Scuola Internazionale Superiore di Studi Avanzati

Ph.D. in Astrophysics and Cosmology

Final Dissertation

The Initial-Final Mass Relation of White Dwarfs: Insights from PARSEC and COLIBRI TP-AGB models

Thesis supervisors

Prof. Alessandro Bressan

Prof. Paola Marigo

Thesis co-supervisor

Dr. Guglielmo Costa

Candidate

Francesco Addari

Academic Year 2023/2024

Abstract

The Initial-Final Mass Relation (IFMR) plays a crucial role in understanding the structure and evolution of stars, by linking the star's initial mass to the mass of its remnant. In this thesis we explore the Initial-Final Mass Relation of White Dwarfs from a theorist perspective, using full PARSEC evolutionary tracks and completing the ejection of the envelope with COLIBRI computations. The journey starts with a detailed review of the PARSEC code, the fundamental equations, and input physics involved in modeling the Thermally-Pulsing Asymptotic Giant Branch phase. With this knowledge at hand, I will present new opacity tables and new numerical methods to accelerate and terminate the AGB evolution. Finally, with all the tools ready, we aim to reproduce the recently observed non-monotonic behavior in the IFMR. The presence of a kink at $M_{\rm ini} \sim 1.65 - 2.10$ M$_\odot$ is interpreted as the interaction between recurrent dredge-up events and strong episodes of mass loss. To model the anticipated IFMR, I investigate the role of the efficiency convective overshooting applied at the border of the convective envelope and pulse-driven convective zone (PDCZ). By comparing our stellar models with observational data, I find that no fixed couple of overshooting parameters can explain the kink. Instead, the results suggest an increasing envelope overshooting as the initial mass of the star increases.

Contents

List of Figures

List of Tables

Introduction

The evolution of stars, from their birth in interstellar clouds to their final states, represents one of the most compelling narratives in astrophysics. Central to their tale is the fate of stars like our Sun, which end their lives as white dwarfs (WD). These remnants, composed primarily of electron-degenerate matter, provide crucial insights into the processes governing stellar structure and evolution, nucleosynthesis, and the evolution of galaxies.

The progenitors of white dwarfs are classified as low- and intermediate-mass stars, which roughly cover the range $0.8 \lesssim M_{\rm ini}/{\rm M}_{\odot} \lesssim 8$. Less massive stars still had not enough time to evolve out of their main sequence phase, while more massive stars die in spectacular supernova explosions leaving behind a neutron star or a black hole. The upper mass range of intermediate-mass stars (referred to as $M_{\rm up}$) is subject to large uncertainties mainly associated to core overshooting and also depends on metallicity. Low- and intermediate-mass stars account for the $\sim 95\%$ of the total number of stars assuming a simple Salpeter initial mass function (Salpeter, 1955), meaning that white dwarfs are the most popular remnant of stellar objects out in the Universe.

Discussion on the existence of a relation between a star's initial mass and final mass arose when it became clear that stars with initial masses well above the Chandrasekhar limit (Chandrasekhar, 1931) can end up as white dwarfs. That evidence was pointed out by (Weidemann, 1977) looking at the white dwarfs in the Hyades cluster, for which they estimated a cluster age of $\sim 5\times10^8$ yr and a turn-off mass 2.1 $M_{\odot}$ but already showed WDs. Therefore, the progenitors of those confirmed white dwarfs had to be more massive than the turn-off mass, which is only possible if those stars lost part of their mass to get below the Chandrasekhar limit. Consequently, from the late '70, there have been many advancements and revisions of the initial-final mass relation (IFMR) (Weidemann & Koester, 1983; Weidemann, 1987, 2000; Ferrario et al., 2005; Kalirai et al., 2008; Cummings et al., 2018, and many others) simultaneously with the improvements on the computing power, stellar evolution codes and new white dwarf data. The IFMR plays a key role in several fields of modern astrophysics, a role that goes well beyond in simply assessing the final mass of low- and intermediate-mass stars. Knowing the mass lost by

those stars allows us to place constraints on the efficiency of stellar winds during the progenitor's previous evolution. The mass ejected and returned to the ISM has been processed by the star via nuclear reactions and mixing events, therefore the IFMR is a critical ingredient in chemical evolution models of stellar populations, and in general in any application regarding the origin and evolution of the interstellar gas or the mass-to-light ratio of those stellar systems. On the high mass end, the IFMR provides an empirical test to the lower limit of the stars ending in supernovae explosions, either core-collapse or electron capture.

A recent revision of the IFMR (Marigo et al., 2020) stands out of the sea of results as they found a kink at initial masses $\sim 1.6 - 2.1$ $M_\odot$, while all the other stellar models produce a monotonically increasing relation. The kink, observed in open clusters close to solar metallicity, is caused by the interplay of surface carbon enhancement and the stellar wind in these carbon stars. This work is focused on investigating this idea with complete stellar evolution models, which are a fundamental part of the IFMR studies. However, arriving at the final mass is not a trivial matter; these stars experience the Thermally-Pulsing Asymptotic Giant Branch phase, for which models are still plagued by uncertainties of both numeric and physics nature (Wood & Faulkner, 1986; Wagenhuber & Weiss, 1994; Weiss & Ferguson, 2009; Addari, 2020, to name a few). The main actors of the TP-AGB phase are convection and the stellar wind, which are deeply connected by recurrent (third) dredge-up episodes, which limit the core mass growth and expose helium-burning processed material on the surface (Herwig, 2005). Consequently, if the Third Dredge-up is efficient enough, an M-type star can become carbon-rich during its evolution, but the prediction for the range of initial masses and their impact on the surrounding interstellar medium are heterogeneous because of the complex physical processes that are difficult to model.

In this Ph.D. thesis, we focus on the TP-AGB modeling with `PARSEC` and `COLIBRI` to assess the role of convection, extra-mixing, and mass loss on the initial-final mass relation, aiming to find the kink at $M_{\rm ini} \sim 1.6 - 2.1$ $M_\odot$. This goal requires a deep understanding of the physical processes and numerical techniques that compose a full stellar evolution code. Therefore, a notable fraction of the time has gone into revision, improvement, and new additions to the `PARSEC` code, which is now capable of modeling the TP-AGB phase with limited user assistance and in a (not so un)-reasonable amount of computing time.

The topics in this thesis are presented as follows:

Chapter 1: The first chapter aims to briefly present the evolution of low- and intermediate-mass stars, with a particular focus on the processes and events that shape the final TP-AGB evolution and the mass of the final remnant.

Chapter 2: The second chapter wants to deeply explore the numerical details of modern stellar evolution codes and describes the critical input physics provided. This gives the reader a solid reference for the next chapter.

Chapter 3: The third chapter offers a complete view of the numerical methods I newly implemented in `PARSEC` specifically for the TP-AGB modeling and its critical features.

Chapter 4: The fourth and final chapter constitutes the main matter of the thesis. I investigate the role of the extra-mixing and mass loss in shaping the initial-final mass relation.

Name	Description	First Appearance	Name	Description	First Appearance
PMS	Pre-Main Sequence	Section 1.1	CNO	Carbon-Nitrogen-Oxygen	Sect 1.1
ZAMS	Zero-Age Main Sequence	Section 1.1	EOS	Equation of State	Section 1.1
MS	Main Sequence	Section 1.1	FDU	First Dredge-Up	Section 1.2
TAMS	Terminal-Age Main Sequence	Section 1.1	HBB	Hot Bottom Burning	Section 1.3
RGB	Red Giant Branch	Section 1.1	HR	Hertzsprung-Russell (diagram)	Section 1.1
ZAHB	Zero-Age Core He-Burning	Section 1.1	IFMR	Initial-Final Mass Relation	Introduction
AGB	Asymptotic Giant Branch	Section 1.1	MLT	Mixing-Length Theory	Section 2.2.3
E-AGB	Early AGB	Section 1.1	PDCZ	Pulse Driven Convective Zone	Section 1.3
TP-AGB	Thermally Pulsing AGB	Section 1.1	SDU	Second Dredge-Up	Section 1.2
WD	White Dwarf	Introduction	TDU	Third Dredge-Up	Section 1.3
CHeB	Core He-burning	Section 1.1	TP	Thermal Pulse	Section 1.3

Tab. 1: List of abbreviations used in the following, also with first appearance in the text.

Name	Description	Value	First Appearance
G	universal gravitational constant	$6.67428 \cdot 10^{-8}$ cm^3 g^{-1} s^{-2}	Section 2.1
$L_\odot$	total luminosity of the Sun	$3.828 \cdot 10^{33}$ erg s^{-1}	Section 1.1
$M_\odot$	mass of the Sun	$1.9892 \cdot 10^{33}$ g	Section 1.1
N_A	Avogadro's number	$6.0221415 \cdot 10^{23}$	Section 2.2.1
a	radiation density constant	$7.56578 \cdot 10^{-15}$ erg cm^{-3} K^{-4}	Section 2.1
c	speed of light	$2.99792458 \cdot 10^{10}$ cm s^{-1}	Section 2.1
m_u	atomic mass unit	$1.66054 \cdot 10^{-24}$ g	Section 2.1
σ	Stefan-Boltzmann constant	$5.6704 \cdot 10^{-5}$ erg cm^{-2} K^4	Section 2.2.1

Tab. 2: List of (astro)physical constants used in the following, also with first appearance in the text.

Tab. 3: List of symbols used in the following, also with first appearance in the text. If not specified, the quantities are meant in CGS units.

Name	Description	First Appearance
A_i	atomic mass of element i	Section 2.1
Δt	timestep between two consecutive models	Section 2.2.1
$\Delta M_{\rm core}$	Core mass growth during interpulse	Section 3.2
$\Delta M_{\rm He}$	H-free core growth during interpulse	Section 1.3
$\Delta M_{\rm H}$	mass of burnt hydrogen during interpulse	Section 3.2
$\Delta M_{\rm dup}$	mass involved in TDU	Section 1.3

Tab. 1: (Continued)

Name	Description	First Appearance
$\Delta M_{\rm sdu}$	mass involved in SDU	Section 1.2
$\Delta M_{\rm pdcz}$	PDCZ maximum extension	Section 1.3
$\Delta M_{\rm overlap}$	overlap between consecutives PDCZ	Section 1.3
D	Total diffusion coefficient	Section 2.2.1
$D_{\rm mlt}$	diffusion coefficient of MLT	Section 2.2.3
H_P	pressure scale height	Section 2.2.3
$\Lambda_{\rm ov}$	overshooting parameter at the bottom of the convective envelope	Section 2.2.3
$L_{\rm surf}$ or L	surface luminosity	Section 1.1
$L_{\rm H}$	luminosity produced by H-burning	Section 1.3
$L_{\rm He}$	luminosity produced by He-burning	Section 1.3
$L_{\rm He}$	gravitational luminosity	Section 3.2
M	star total mass at the specified time	Section 2.1
$M_{\rm ini}$	initial star mass	Introduction
$M_{\rm f}$ or $M_{\rm fin}$	final star mass	Section 3.3.3
$M_{\rm core}$	mass of the core	Section 3.2
$M_{\rm He}$	mass coordinate of the H-free core (X-Y discontinuity)	Section 1.1
$M_{\rm CO}$	mass coordinate of the CO core	Section 1.3
$M_{\rm min}$	minimum mass of the XY discontinuity after pulse	Section 1.3
$M_{\rm env}$	envelope mass	Section 3.3.3
$M_{\rm max}$	maximum mass of the CO core just before TP	Section 1.3
$M_{\rm top}$	top mass of PDCZ at maximum extension	Section 1.3
$M_{\rm bot}$	bottom mass of PDCZ at maximum extension	Section 1.3
$M_{\rm HeF}$	initial mass of the most massive star experiencing He-Flash	Section 1.1
$M_{\rm Ch}$	Chandrasekhar mass	Section 1.1
P	pressure	Section 2.1
R	star radius	Section 2.1
R_2	number ratio between horizontal branch and AGB stars	Section 2.2.3
S	local entropy density	Section 2.1
T	local temperature	Section 2.1
$T_{\rm c}$	central temperature	Section 2.1
$T_{\rm eff}$	effective temperature	Section 1.1
X_i	mass fraction of element i	Section 1.3
X	hydrogen mass fraction	Section 3.1
Y_i	number density of element i	Section 2.2.1
Y	helium mass fraction	Section 3.1
Z	metals mass fraction	Section 2.2.5
α	mixing length parameter	Section 2.2.3
$\eta_{\rm R}$	Reimers wind efficiency	Section 2.2.3
$\eta_{\rm B}$	Blöcker wind efficiency	Section 2.2.3

Tab. 1: (Continued)

Name	Description	First Appearance
ℓ	local luminosity	Section 2.1
$f_{\rm env}$	overshooting parameter at the bottom of the convective envelope	Section 2.2.3
$f_{\rm ov}$	generic overshooting parameter in the exponential prescription	Section 2.2.3
$f_{\rm pdcz}$	overshooting parameter at the borders of PDCZ	Section 2.2.3
j	j-th mesh point of the structure	Section 2.2.1
κ	Rosseland mean opacity	Section 2.1
$\lambda_{\rm ov}$	overshooting parameter at the border of the core	Section 2.2.3
λ	$= \Delta M_{\rm dup}/\Delta M_{\rm He}$ TDU efficiency	Section 1.3
m	mass coordinate of a spherical shell	Section 2.1
μ	mean molecular weight	Section 2.2.3
μ_e	electron mean molecular weight	Section 1.2
∇	temperature gradient	Section 2.1
$\nabla_{\rm ad}$	adiabatic temperature gradient	Section 2.1
$\nabla_{\rm rad}$	radiative temperature gradient	Section 2.1
∇_μ	mean molecular weight gradient	Section 2.2.3
$q_{\rm val}$	effective q-value of hydrogen burning rections	Section 3.2
ρ	density	Section 2.1
$\rho_{\rm c}$	central density	Section 2.1
r	radial coordinate	Section 2.1
$r_{\rm bce}$	radius of the bottom of the convective envelope	Section 2.2.5
t	time or current age	Section 1.1
$t_{\rm TAMS}$	age at TAMS	Section 1.1
$t_{\rm end-He}$	age at the end of CHeB	Section 1.2
$t_{\rm TP1}$	age at the first thermal pulse	Section 1.3
τ	optical depth	Section 2.2
$\tau_{\rm int}$	duration of interpulse period	Section 3.3.3
$\varepsilon_{\rm nuc}$	nuclear power produced per unit mass	Section 2.1
ε_ν	neutrino power per unit mass	Section 2.1
$\varepsilon_{\rm grav}$	gravitational power per unit mass	Section 2.1
$v_{\rm mlt}$	velocity of MLT	Section 2.2.3

List of publications

1. **F. Addari**, P. Marigo, A. Bressan, G. Costa, K. G. Shepherd, G. Volpato (2024), *The Role of the Third Dredge-up and Mass Loss in Shaping the Initial–Final Mass Relation of White Dwarfs*, The Astrophysical Journal, Volume 964, Issue 1, id.51, 13 pp.

2. G. Volpato, P. Marigo, G. Costa, A. Bressan, M. Trabucchi, L. A. Girardi, **F. Addari** (2024), *A Study of Primordial Very Massive Star Evolution. II. Stellar Rotation and Gamma-Ray Burst Progenitors*, The Astrophysical Journal, Volume 961, Issue 1, id.89, 23 pp.

3. A. Bressan, G. Costa, S. Goswami, V. Grisoni, K. G. Shepherd, L. Silva, **F. Addari**, P. Marigo (2023), *Very massive stars chemical enrichment in extremely metal-poor galaxies*, Memorie della Società Astronomica Italiana, Vol. 94, No. 2, 2023, p. 91

4. P. Marigo, D. Bossini, M. Trabucchi, **F. Addari**, L. A. Girardi, J. D. Cummings, G. Pastorelli, P. Dal Tio, G. Costa, A. Bressan (2022), *A Fresh Look at AGB Stars in Galactic Open Clusters with Gaia: Impact on Stellar Models and the Initial-Final Mass Relation*, The Astrophysical Journal Supplement Series, Volume 258, Issue 2, id.43, 37 pp.

5. P. Marigo, **F. Addari**, D. Bossini, A. Bressan, G. Costa, L. A. Girardi, M. Trabucchi, G. Volpato (2024), *ÆSOPUS 2.1: Low-Temperature Opacities Extended to High Pressure*, accepted by ApJ, 10.48550/arXiv.2409.10905

6. C. T. Nguyen, A. Bressan, A. J. Korn, G. Cescutti, G. Costa, **F. Addari**, L. A. Girardi, X. Fu, Y. Chen, P. Marigo (2024), *A combined study of envelope overshooting and thermohaline mixing with PARSEC: Calibration to M4 and NGC 6397*, submitted to A&A.

7. G. Costa, K. G. Shepherd, A. Bressan, **F. Addari**, Y. Chen, X. Fu, L. Girardi, P. Marigo, C. T. Nguyen, G. Volpato, G. Pastorelli, M. Trabucchi (2024), *Evolutionary tracks, ejecta, and ionizing photons from intermediate-mass to very massive stars with PARSEC*, to be submitted.

CHAPTER 1

Evolution of low- and intermediate-mass stars

The mass of a star largely determines its evolution and final fate. This suggests a classification in three categories: low-mass, intermediate-mass, and massive stars. The Ph.D. thesis is focused on the first two classes, accounting for initial masses $0.8 \lesssim M_{\rm ini}/{\rm M}_{\odot} \lesssim 8$, thus this first chapter is dedicated to briefly describing the evolution of such stars from the beginning to the end. All the plots (but two) in this chapter result directly from my PARSEC calculations. Details of the code and input physics are discussed in the next chapters. This chapter contains fairly well-known results of years of stellar structure and evolution research, and we refer mainly to the books by (Kippenhahn, 1990; Hansen, 2004; Maeder, 2009).

1.1 Before the TP-AGB phase

Stars are born in molecular clouds, from the gravitational collapse of part of its material. After a period of accretion, they finally reach the hydrostatic equilibrium, which sets the beginning of the PMS phase. In Figure 1.1 we plot the evolutionary tracks of two prototypes for low- and intermediate-mass stars, respectively for 1 $M_{\odot}$ and 4 $M_{\odot}$. Important evolutionary points are marked by letters, which we extensively use in the following discussion to ease the discussion of the evolution. Both tracks begin at the PMS (point A), where no stable nuclear burning can take place. In this stage, the star has no support against gravitational contraction and is fully convective, therefore it evolves down in luminosity along the Hayashi line. During the transition between point (A) and (B), the contraction can be halted for a few $\sim 10^5$ yr by the deuterium burning. This stage is also important for lithium, as it is quickly destroyed, leaving only traces in the stellar envelope. Deuterium follows a similar fate, as it can interact with hydrogen even down to $T \sim 10^6$ K. While the star contracts, it gets hotter and the opacity decreases, which causes the convective region to be relegated closer to the surface.

At some point, the central temperature reaches $T \sim 10^7$ K and hydrogen can be ignited. How

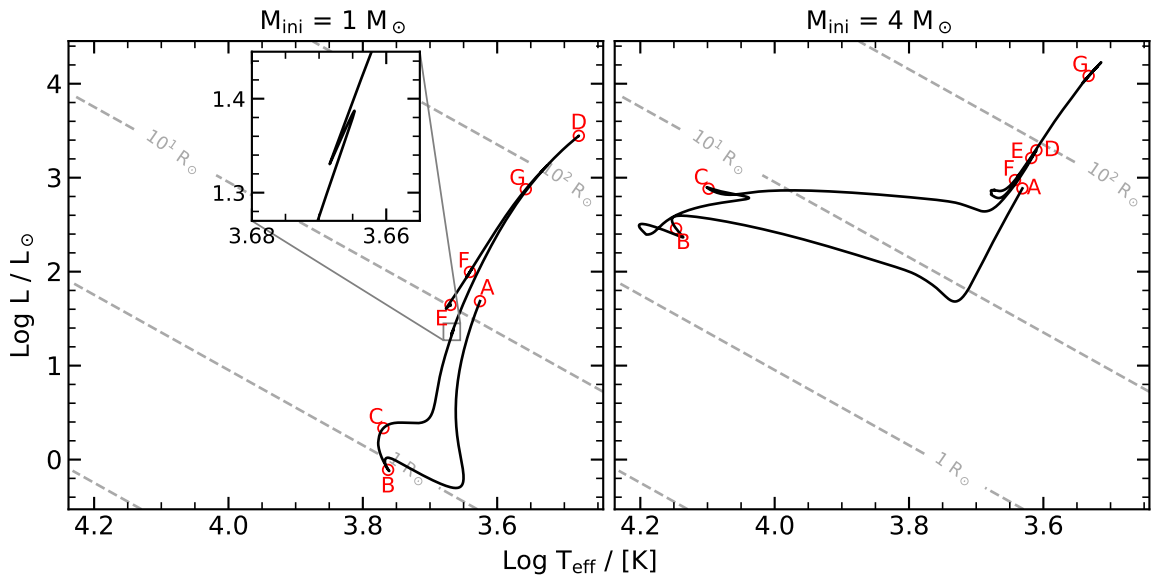

Fig. 1.1: Evolutionary tracks for 1 and 4 $M_\odot$, prototypes of the low- and intermediate-mass classes, respectively. The circles identify, in order: (A) the beginning of PMS; (B) ZAMS; (C) TAMS; (D) Tip of RGB; (E) ZAHB; (F) the beginning of E-AGB; (G) the beginning of TP-AGB. Both tracks end at the first thermal pulse. The zoomed window in the left panel shows the first dredge-up signature.

hydrogen is burnt depends on the mass of the star and metallicity. At about solar metallicity, hydrogen is burnt via pp-chain reactions in a radiative core if $M_{\rm ini} \lesssim 1.2\ M_\odot$. At larger masses, CNO cycles are activated and they generate much more luminosity per unit mass with respect to pp chains, which causes the core to be convective. The difference in radiative and convective hydrogen core burning has critical consequences on the following evolution. Indeed, at the TAMS (point C), a hydrogen-burning shell is naturally formed outside radiative cores because hydrogen is gradually depleted from the center outwards, so the star smoothly approaches the sub-giant branch. Instead, hydrogen burning in a convective core proceeds until the whole region is depleted, which leaves the star without support against the gravitational force. The star has to contract, and the consequent temperature increase ignites the H-burning in a shell around the newly formed helium core. The increase in temperature is visible on the HR of this type of star at the TAMS (i.e. the hook-like shape close to point C in the right panel of Figure 1.1).

In any case, after MS, the star has no nuclear reaction in the helium core and the structure is sustained solely by the hydrogen-burning shell. Its ashes build up the He-core, and in contrast, the envelope expands and cools down, quickly bringing the star towards the Hayashi line at about constant luminosity. Simultaneously, the convective envelope deepens until it covers most of the structure and the star reaches the Hayashi line. This limit cannot be crossed, meaning that stable stars cannot be found at temperatures lower than the Hayashi line, as they would be quickly warmed up by convective energy transport. After reaching the bottom of the RGB, the evolution proceeds up in luminosity. Since the temperature does not change considerably, the star's radius has to increase quickly by a factor $\sim 10 - 100$, as shown by the constant radius contours in Figure 1.1. During the rise along the RGB, the star experiences the first dredge-up,

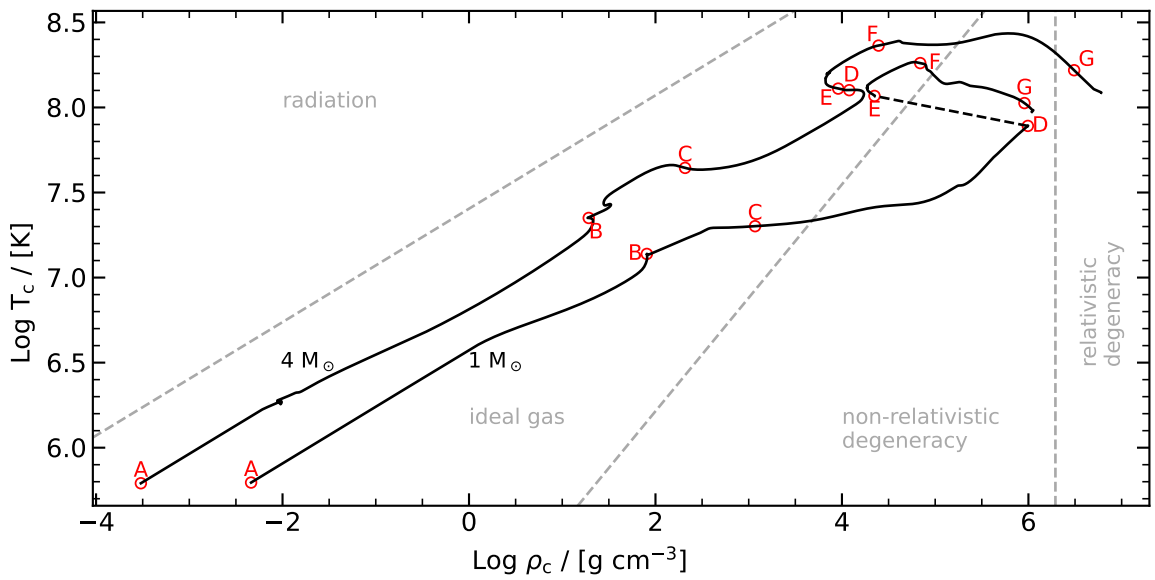

Fig. 1.2: Log ρ_c-Log T_c tracks for 1 and 4 $M_\odot$, prototypes of the low- and intermediate-mass classes, respectively. The circles identify, in order: (A) the beginning of PMS; (B) ZAMS; (C) TAMS; (D) Tip of RGB; (E) ZAHB; (F) the beginning of E-AGB; (G) the beginning of TP-AGB. Both tracks end at the first thermal pulse. The dashed line between D and E points of the 1 $M_\odot$ corresponds to where He-flash takes place and lifts the degeneracy. Areas identified by dashed lines show where a certain type of EOS (roughly) dominates over the others.

which we discuss separately in the following section (Section 1.2). At the tip of RGB (point D) the star can ignite helium, and how it takes place separates the low and intermediate-mass star classes. Low-mass stars $M_{\rm ini} < M_{\rm HeF}$ (~ 2 $M_\odot$) have developed a strongly degenerate core, as shown in the $T_c - \rho_c$ diagram in Figure 1.2 (evolution from C to D). During the RGB the pressure of degenerate electrons sustains the core below the burning H-shell, up to point D, where He is ignited in the core. The ignition takes place off-center and starts a thermal runaway, as the injection of energy causes the temperature to increase without an immediate reaction of the core, in such degenerate conditions. A large amount of energy is generated in a short event called Helium flash, and it (with a series of lower energy flashes) can lift the degeneracy bringing the star to point (E), where it quiescently burns helium in the core. Instead, for $M_{\rm ini} > M_{\rm HeF}$ stars quickly evolve from (D) to (E) avoiding the degeneracy (see the 4 $M_\odot$ track in Figure 1.2). The tip of the RGB can be used as a robust distance indicator (Lee et al., 1993) because the low-mass stars arrive at the flash with basically the same core mass, setting the luminosity at the tip.

Once helium is ignited, the central burning proceeds similarly to the core H-burning, namely the star is relatively stable and this phase is long compared to the other evolutionary phases. Given the MS as the most stable and longest phase, the CHeB phase lasts about one-tenth respect to the central hydrogen burning phase. At the end of CHeB, as before, the star is left with a He shell surrounding a carbon-oxygen core. On top of both we still have a hydrogen shell and an extended convective envelope, up to the surface. The star has entered the AGB phase, divided into the early AGB and the thermally pulsing AGB. The second is described in detail in Section

1.3. In the E-AGB phase, the star is initially supported by two burning shells: the H-shell and the He shell, which ashes add to the CO core, meaning that the He-shell is pushed outwards in mass and becomes thinner. In stars $M_{\rm ini} \lesssim 4$ M$_\odot$ (at solar metallicity) both shells stay active until the TP-AGB phase, which starts when the He shell is so thin that it does not provide a significant amount of energy. In more massive AGB stars, the H-shell temporarily shuts down and the convective envelope can penetrate even below it. This is called second dredge-up, which again brings up hydrogen-burning ashes and, more importantly, limits the growth of the CO core, allowing stars with cores even larger than $M_{\rm ch}$ to end up as white dwarfs.

1.2 The first and second dredge-up

Dredge-ups occur when the convective envelope mixes regions previously processed by nuclear reactions. These events pollute the surface with new material, and the abundance changes might be detected in spectra. There are three types of dredge-up events: the first and the second dredge-up take place before the TP-AGB phase, while the third dredge-up can occur multiple times during this very final phase. In this section, we want to briefly discuss the first two dredge-up events, while an extensive discussion on the third is found in Section 1.3 or Chapter 4.

The FDU occurs during the RGB phase, leaving a visible signature on the HR diagram (see zoomed window in Figure 1.1) of low-mass stars, fading at increasing mass. The temporary stalling of the luminosity increase is caused by the H-shell reaching the discontinuity left by the convective envelope, after the FDU. This feature is significant as it corresponds to the observed crowding of red giant stars in color-magnitude diagrams, commonly called RGB bump. It is sensible to the extra-mixing (usually overshooting) applied at the bottom of the convective envelope, constraining its value and allowing for calibration (Alongi et al., 1991). In Figure 1.3 we show the effect of the FDU on surface abundances. The convective envelope brings up material processed by hydrogen burning, showing the pattern of the dominating nuclear pathway, being pp-chains or CNO-cycles. The low-mass prototype is dominated by the pp-chain reactions, which results in the ^{3}He surface abundance showing the most variation. We can appreciate that the composition of the material changes as the convective envelope reaches deeper layers since CNO-cycle signature elements (^{13}C and ^{14}N) are brought up later than the pp-chain elements, and the core was not convective during central H-burning. On the other hand, the intermediate-mass example shows a large variation of ^{14}N surface abundance, a marker of the CNO cycles. In this case, the composition variation is simultaneous for both nuclear pathways because the star burnt hydrogen in a convective core.

The SDU has a similar effect as the FDU on the surface abundances, meaning that it also uncovers newly H-burning processed material (see Figure 1.4). However, it has a much more dramatic effect on the final fate of intermediate-mass stars. At the end of central He burning, stars are left with a carbon-oxygen core, which is not degenerate for massive stars. They experience all subsequent burning stages (carbon, neon, oxygen, silicon), and they will eventually explode

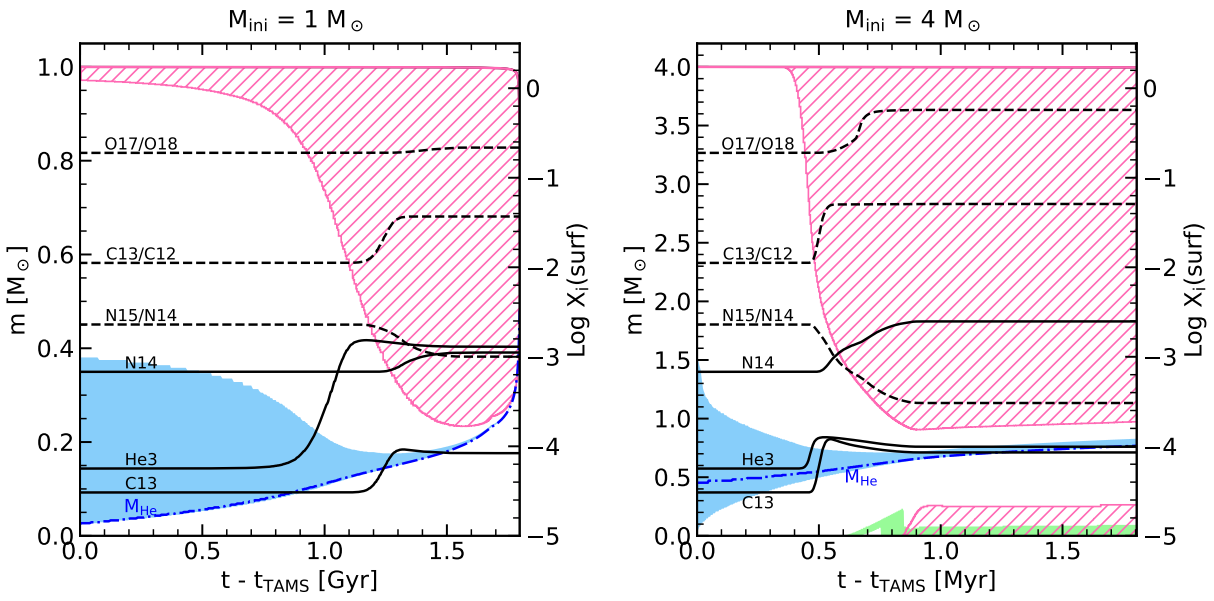

Fig. 1.3: Kippenanhn diagrams (mass coordinate on the left of each plot) for 1 $M_\odot$ and 4 $M_\odot$ tracks during the RGB phase Convective regions are marked by the pink hatching, light blue and light green corresponds, respectively, to hydrogen and helium burning regions. The blue dash-dotted line marks the boundary of the He-core. We superimpose a few surface abundances (solid lines) and isotopic ratios (dashed lines), which refer to the Log X_i(surf) axis on the right of each plot, where i is the annotated element or ratio.

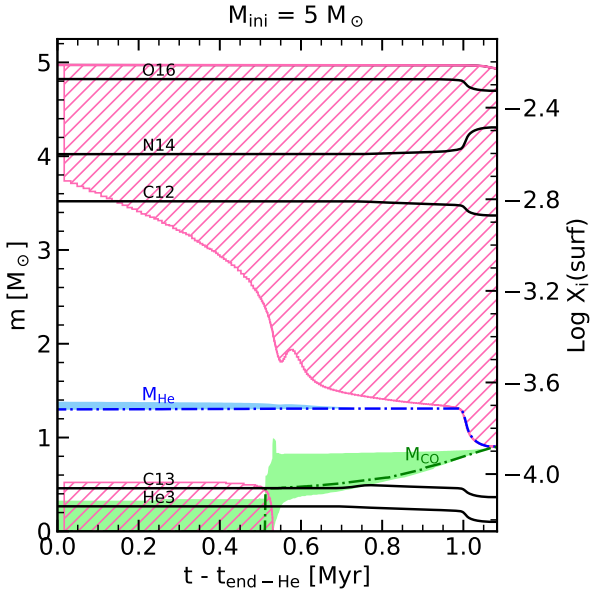

Fig. 1.4: Kippenanhn diagram (mass coordinate on the left) for 5 $M_\odot$ track during the E-AGB phase. The green dash-dotted line marks the boundary CO-core, respectively. See Figure 1.3 for the complete legend.

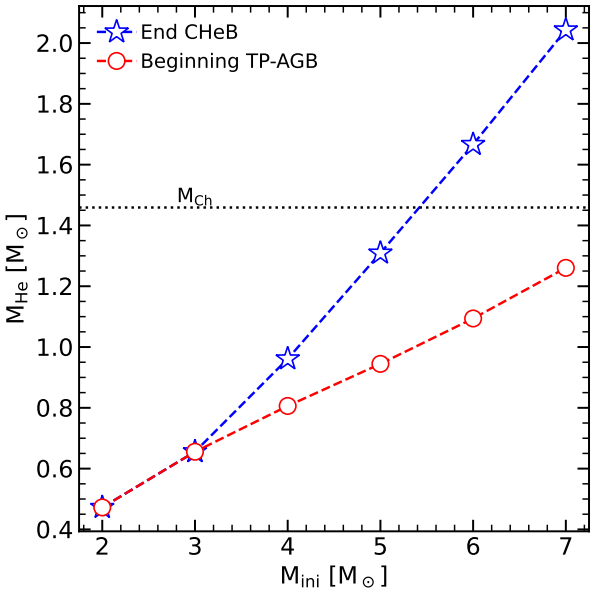

Fig. 1.5: He-core mass at the end of CHeB (blue stars) and beginning of TP-AGB (red circles) for intermediate-mass stars. The dotted black line marks the value of the Chandrasekhar mass for $\mu_e = 2$.

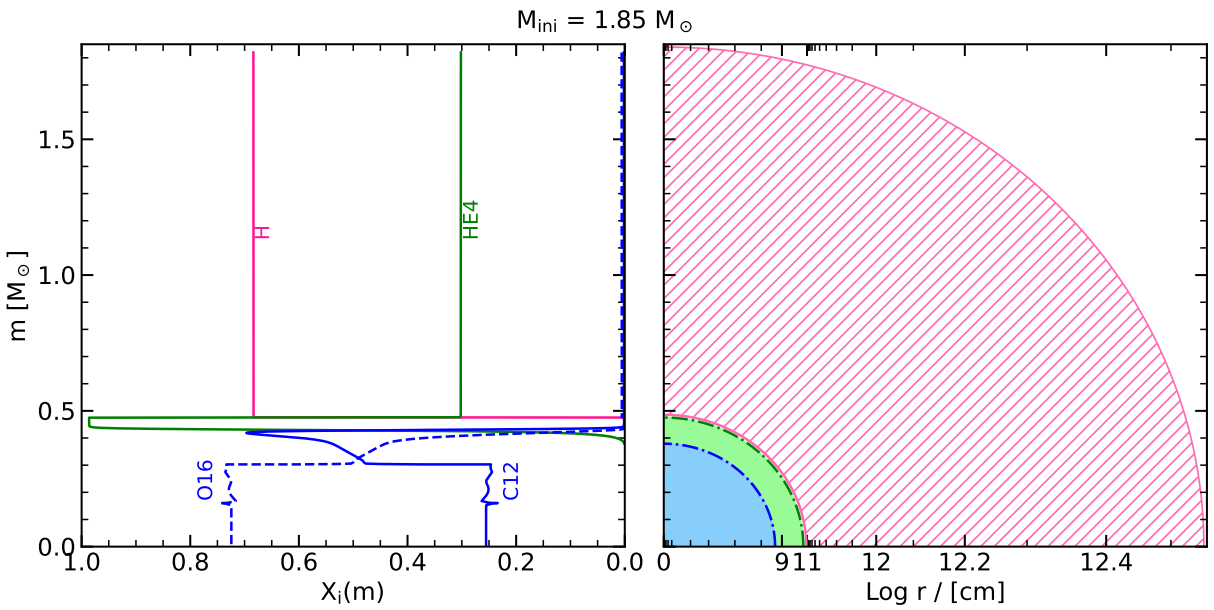

Fig. 1.6: Structure of a TP-AGB star. On the left panel, hydrogen, helium, carbon, and oxygen profiles against the mass coordinate. On the right panel, mass (y-axis, same as left panel) and radial (x-axis) cross-section of the star layers. The pink hatching marks the convective regions, the green where the abundance is dominated by He, and blue where it is dominated by C and O.

as supernovae. Low and intermediate-mass stars are left with a degenerate CO-core, but the picture of the following evolution is still a matter of debate (Doherty et al., 2017; Limongi et al., 2024). The most massive AGB stars can ignite carbon in degenerate conditions (similarly to the He-flash of low-mass stars), which converts ^{12}C into ^{16}O, ^{20}Ne and ^{24}Mg, and after that they go through the TP-AGB phase. If the mass of the newly formed ONeMg-core is less than $M_{\rm Ch}$ (~ 1.44 M$_\odot$ for $\mu_e \simeq 2$) then they will leave an ONeMg WD as a remnant. Otherwise, electron capture can remove the support of the pressure of degenerate electrons, causing the collapse of the core and the development of an ECSN. This sets the boundary between intermediate-mass stars and massive stars, which is highly influenced by the efficiency of the second dredge-up, besides extra mixing in the core and, to a lesser extent, in the envelope. Figure 1.5 shows the effect of SDU on the mass of the hydrogen-depleted core on tracks with $2 \leq M_{\rm ini}/\,{\rm M}_\odot \leq 7$. The dredge-up mass increases considerably with the initial mass, topping at $\Delta M_{\rm sdu} \sim 0.9$ M$_\odot$ for $M_{\rm ini} = 7$ M$_\odot$.

1.3 The TP-AGB phase

The structure of a star at the beginning of the TP-AGB phase is shown in Figure 1.6. The convective envelope extends for most of the radial structure, from $R \sim 10^{11}$ cm to $\sim 5 \times 10^{12}$ cm, while the mass is only $\sim 3/4$ of the total. Therefore, compared to the envelope the core is extremely dense, on top of which the star has a thin He-intershell, the main actor driving the evolution in this phase. The thinness of the He-shell makes it geometrically unstable, meaning

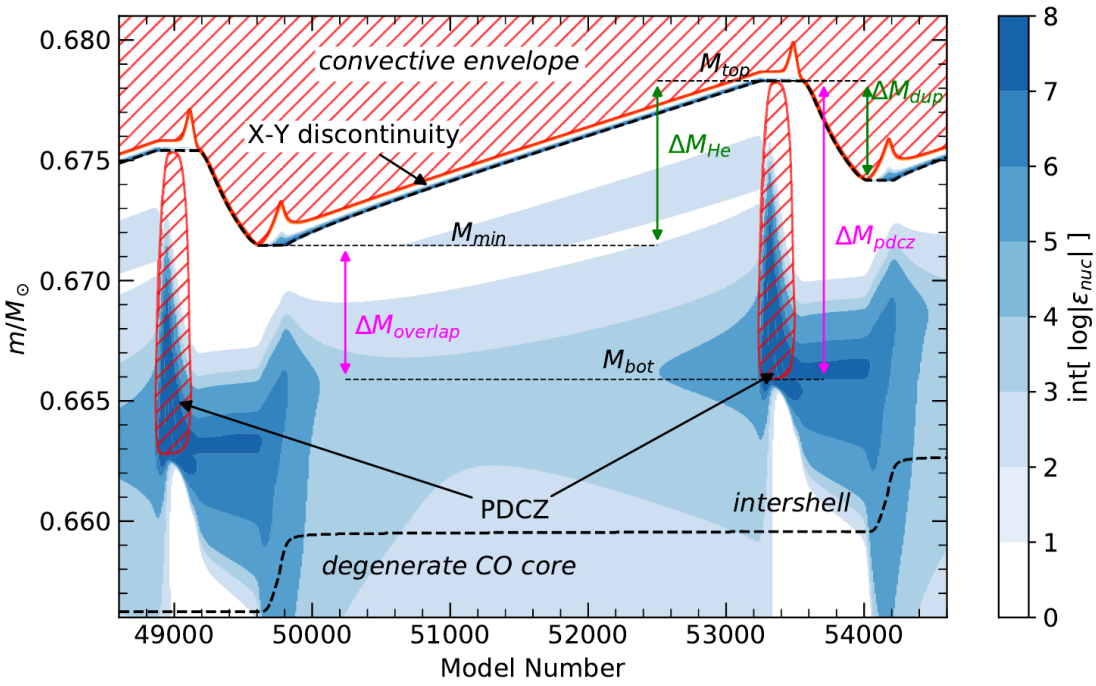

Fig. 1.7: Kippenhahn diagram during a pulse cycle of a 3 $M_\odot$ track, computed with `MESA` (Paxton et al., 2011; Jermyn et al., 2023) by Addari (2020). Red hatching marks the convective layers. The blue colormap quantifies the nuclear energy produced per unit mass and time. The time is represented in the real number of models, as in proper time units the PDCZ would not be easily visible as it is too short-lived.

that if conditions to activate He-burning are met, it is not able to cool down enough to stop a thermonuclear runaway. This event, called *thermal pulse*, occurs repeatedly during the lifetime of a TP-AGB star, and causes a series of critical consequences. We can analyze the pulse cycle starting from the TP, with the aid of Figure 1.7:

1. **TP.** He-burning turns on in the intershell for a short time ($\sim 1-10$ yr) and generates a large luminosity flux. The pulse's energy drives convection in the intershell, forming the PDCZ, but most of it does not escape as surface luminosity (left panel, Figure 1.8). The energy injection makes the envelope expand and cool down, and eventually, the flash is quenched. Different nuclear pathways are activated, aside from the He-burning reactions, depending on the temperature at the bottom of the PDCZ (where most of the energy is generated). In particular, in intermediate-mass stars with $M \gtrsim 4M_\odot$ the ^{22}Ne(^{4}He,n)^{25}Mg reaction is very active at the base of the convective pulse and the released neutrons contribute to the production of (light) s-process elements.

2. **TDU.** The sudden expansion and cooling of the envelope may cause it to penetrate inside the He-shell, mixing He-burning ashes and s-process elements up to the surface for about $\sim$ 100 yr (right panel, Figure 1.8). The intershell material (mainly ^{4}He, ^{12}C and ^{16}O) greatly affects the surface conditions, generally increasing the opacity and favoring the formation of dust. The occurrence or not of the TDU depends on the power of the TP,

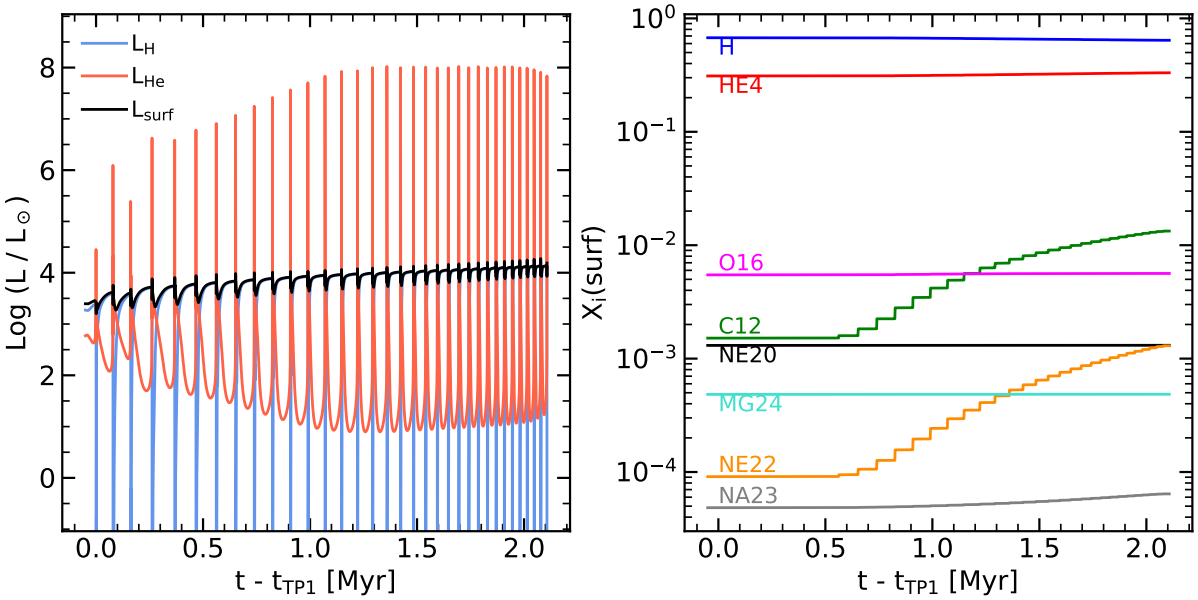

Fig. 1.8: Luminosity (left panel) and surface abundance (right panel) evolution during the TP-AGB phase of a $M_{\rm ini} = 2.5$ M$_\odot$ track. The time axis is offset to the age at the first thermal pulse.

which is correlated with the mass of the core at the ignition of the flash. Its efficiency is highly dependent on the convection physics, other mixing processes, and even numerics of the code itself, but as a rough reference, the core mass has to be at least $M_{\rm He} \gtrsim 0.55$ M$_\odot$ for the occurrence of the TDU. The efficiency is defined as:

$$\lambda = \frac{\Delta M_{\rm dup}}{\Delta M_{\rm He}} \tag{1.1}$$

which is just the fraction of the mass growth "lost" in the envelope penetration. The efficiency λ also depends on the envelope mass, which is steadily decreased by the stellar wind, and when $M_{\rm env} \lesssim 0.5$ M$_\odot$, TDU does not occur anymore.

3. **Interpulse.** After the TP (and eventually the TDU), H-burning turns on again in a thin hydrogen shell in between the envelope and the He-intershell (in Figure 1.6 it is barely visible). The ashes of the H-burning make the core grow steadily, which builds up pressure on the He-intershell until a new He-flash sets in. The interpulse is the longest phase in the cycle, taking $\sim 10^3 - 10^5$ yr depending on the core mass. Therefore, most of the time the star is sustained by the H-shell and stays relatively quiescent, as shown by the surface luminosity evolution in Figure 1.8. In the most massive AGBs ($M_{\rm ini} \gtrsim 5$ M$_\odot$, at solar metallicity) the temperature at the bottom of the convective envelope exceeds $\sim$ 40MK, igniting hydrogen burning. This is called Hot Bottom Burning, which modifies the core evolution and the surface abundances. Since part of the H-shell is inside the convective envelope, the ashes are mixed within it and do not contribute to the growth of the He-core.

The general picture of the pulse cycle is fundamental in understanding the interplay of the various physics phenomena at play in this stage. On top of the TP and TDU events, TP-AGB stars experience strong winds, dust formation, and radial pulsations. These are all linked

together, as the mass loss is thought to be driven by radiative pressure on dust assisted by pulsations. While the star evolves towards its maximum extension, during a pulsation (not a thermal pulse!) period, it pushes atmospheric material outwards, which is compressed and cools down. This is the ideal setting for dust formation, which then can be pushed out by the radiation emitted at the photosphere, also dragging the gas surrounding the grain. This mechanism is synchronized with the pulsations, causing strong episodes of mass loss during the evolution. The magnitude of the wind also depends on the surface composition of the star, and in particular on the carbon-to-oxygen number ratio C/O. Given that the most bonded molecule is carbon monoxide, oxygen or carbon available to form dust comes from the atoms not locked in the CO molecule. Oxygen-rich (M-type stars, $C/O < 1$) mixtures form silicate dust grains, such as olivine and pyroxene. A carbon-rich (C-type stars, $C/O > 1$) composition instead forms carbon dust grains, e.g. amorphous carbon, and silicon carbide. The surface composition is not fixed if TDU events occur, therefore a single TP-AGB star can have multiple wind-driving dust molecules, which will result in different mass loss rates. At the beginning of the AGB stars are richer in oxygen than carbon, but with the TDU the C/O may be increased over unity. The increase of the carbon excess in the surface is counteracted by the HBB, which quickly converts ^{12}C brought up from the intershell to ^{14}N. C-type stars (the endpoint of some TP-AGB stars) are expected to experience a stronger mass loss than M-type stars, being cooler and more opaque, even reaching $10^{-5} - 10^{-4}$ $M_{\odot}yr^{-1}$. Dust formation and condensation (and the interaction with the TPs) is a complicated matter that is out of the scope of this work, but a general picture is needed to understand the choices of the input physics of our models. In general, the mass loss rate sets the lifetime of the TP-AGB phase, the number of TP cycles, and ultimately the final mass of the resulting white dwarf. That is, when the envelope is thin enough ($10^{-2} - 10^{-3}$ $M_{\odot}$) the star heats up and leaves the AGB phase and enters the post-AGB phase.

1.4 Road to the white dwarf stage

In the post-AGB phase, the star's radius decreases while its temperature increases, maintaining nearly constant luminosity, which is still powered by the residual hydrogen-burning shell. The star reaches very high effective temperatures ($\mathrm{Log}\, T_{\mathrm{eff}} \gtrsim 4.5$), radiating in the UV band and ionizing the surrounding circumstellar envelope (which consists of the previously ejected mass), thus appearing as a planetary nebula. Eventually, hydrogen burning ceases, and the star gradually cools into a white dwarf, dimming over time. Interestingly, during the post-AGB phase or even in the early stages of white dwarf cooling, the star may undergo a final thermal pulse, temporarily reverting to the AGB region of the Hertzsprung-Russell diagram. Those are called, respectively, late and very late thermal pulses. Figure 1.9 shows the evolution from the early AGB phase to the white dwarf stage, ending at $\log L/L_{\odot} = -2$. A (very) late thermal pulse does not affect the location of the white dwarf cooling track, which is both a pro and a con. It is a convenient feature because we can fit WD models and get the cooling age without worrying about previous late TP events, but this also means that we cannot guess whether or not a late TP occurred

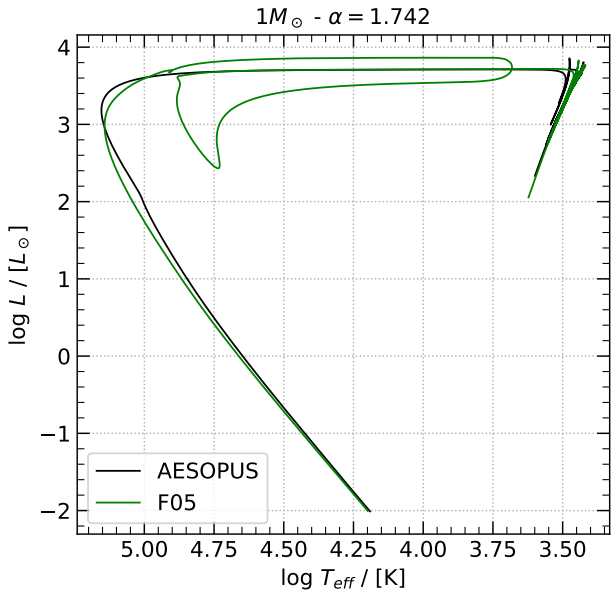

Fig. 1.9: Two evolutionary tracks fo $M_{\rm ini}$ = 1 $M_\odot$ from AGB to WD phase, with different opacity. Both are computed with the `MESA` code (Paxton et al., 2011; Jermyn et al., 2023), taken from (Addari, 2020). The opacity tables `F05` are taken from Ferguson et al. (2005), and the track computed with them experiences a very late thermal pulse.

by observing the remnants. Finally, it is not yet clear what are the conditions to trigger a late thermal pulse, our example showed that just a change in the opacity tables can produce very different outcomes, while the previous evolution remains fairly similar.

CHAPTER 2

Stellar structure and evolution equations

What do you do, you deprive yourself?

An extremely contagious catchphrase,
with a deep lifestyle meaning.

In the previous Chapter, we set the stage by briefly describing the evolution of low- and intermediate-mass stars from a qualitative point of view. Chapter 2 aims to provide the technical details on the equations governing the star's structure and evolution. In this work, I focus on how PARSEC (Bressan et al., 2012) faces the problem. However, deriving each equation from scratch is not the scope of this thesis, even though much can be learned with pen-and-paper calculations. Nevertheless, I carefully review the most important features needed to discuss the following Chapters, also giving credit to the time I spent studying, polishing, and improving parts of the PARSEC code throughout the project. For the following, more theoretical, sections we mainly refer to any classical academic stellar structure and evolution book (Kippenhahn, 1990; Weiss et al., 2004) and to Kippenhahn et al. (1967).

2.1 Brief overview on the general equations

As usual in the physics realm, we have to make assumptions to simplify the system and be able to write down a system of equations. The first one is spherical symmetry, which allows us to write every equation with a single spatial coordinate. The intuitive choice would be the radius r, from the center $r = 0$ to the surface at $r = R$. However, it is often more convenient to work in a Lagrangian coordinate system, dividing the star into mass shells identified by the mass enclosed by the shell itself:

$$m = \int_0^r \mathrm{d}r' 4\pi r'^2 \rho(r') \tag{2.1}$$

where m ranges from 0 at the center to M at the surface. Eq. 2.1 already contains our second assumption: we impose that the mass is conserved in every mass shell. This does not mean mass cannot flow throughout the structure, but we say that the net flow is zero. Differentiating Eq. 2.1 gives us the first equation of stellar structure:

$$\boxed{\frac{\partial r}{\partial m} = \frac{1}{4\pi r^2 \rho}} \tag{2.2}$$

where the partial derivative is needed because every quantity also depends on time t. Once we choose the independent coordinate, the next step is to analyze the forces acting on a mass element. In this regard, we assume there is no net force on the element, namely we say the star is in hydrostatic equilibrium. This is suggested empirically since the vast majority of stars show no change over human lifetimes, implying their evolution occurs on much longer timescales. Nowadays, we know that stars experience stable oscillation over much shorter periods. Nevertheless, we can still safely say that these oscillations average out over typical stellar timescales, which are the focus of this work. To study oscillations the acceleration cannot be neglected, and other types of codes are needed. Finally, hydrostatic equilibrium leads us to the second stellar structure equation:

$$\boxed{\frac{\partial P}{\partial m} = -\frac{Gm}{4\pi r^4}} \tag{2.3}$$

Being m and r strictly positive, Eq. 2.3 immediately implies the pressure must increase inwards in the star's structure, eventually suggesting to use P as depth coordinate. Eqs. 2.2 and 2.3 set the dynamics of the stellar structure. We now turn on the thermodynamics part of the system of equations. Directly from the first law of thermodynamics, applied locally, follows the third equation:

$$\boxed{\frac{\partial \ell}{\partial m} = \varepsilon_{\rm nuc} - \varepsilon_\nu + \varepsilon_{\rm grav}} = \varepsilon_{\rm nuc} - \varepsilon_\nu - T\frac{\partial S}{\partial t} \tag{2.4}$$

This equation ensures that energy is locally conserved by accounting for every possible energy source or sink. $\varepsilon_{\rm nuc}$ quantifies the energy produced by nuclear reactions, already considering neutrino losses; ε_ν accounts for all neutrino losses that do not come from nuclear reactions, which are important in the latest phases of massive stars or strongly degenerate conditions; $\varepsilon_{\rm grav}$ determines the energy released or absorbed by a contraction or an expansion of the structure. Finally, we need to describe how this energy is transported throughout the structure with the fourth and last equation, which reads:

$$\boxed{\frac{\partial T}{\partial m} = -\frac{GmT}{4\pi r^4}\nabla} \tag{2.5}$$

The transport mechanism sets the expression for the temperature gradient ∇. There are three ways for the energy to flow inside the structure: radiative, conductive, and convective. The first two acts similarly, thus we generally refer to those regions in which these mechanisms are active

as radiative. Here the temperature gradient is:

$$\nabla = \nabla_{\rm rad} = \frac{3}{16\pi acG}\frac{\kappa \ell P}{mT^4} \tag{2.6}$$

Instead, in convective regions, the energy is transported with macroscopic movements of the stellar matter. The temperature gradient here must be determined by a theory of convection, and for now we just define it as $\nabla_{\rm ad}$. We defer this discussion to Section 2.2, where we describe how PARSEC deals with convective mixing. Solving the system composed by Eqs. 2.2, 2.3, 2.4 and 2.5 means finding the functions $P(m,t)$, $T(m,t)$, $r(m,t)$ and $\ell(m,t)$. However, the system of equations is not closed yet. The quantities ρ, $\varepsilon_{\rm nuc}$, ε_ν, S, κ and $\nabla_{\rm ad}$ are all functions of temperature, pressure, and chemical composition; they have to be provided to close the system. These functions are part of the input physics of the stellar evolution code, which is discussed in the PARSEC framework in Section 2.2. However, once every auxiliary function is set, the system can be solved numerically and the solution at time t is called *stellar model*. The evolution of the star is then given by a sequence of stellar models, in which structure and chemical composition change with time.

During the star's evolution, chemical composition profiles may be modified by a variety of processes. Inside stars, elements are being processed and transformed into new species by nuclear reactions. At the same time (and eventually in the same mass shells) elements can be mixed throughout the structure. Elements are moved mainly by convective motions, but rotation, microscopic diffusion, thermohaline mixing, and gravitational settling may have a role in modifying the chemical profile of the star. For the rest of the manuscript, we focus only on convection as for this work we did not include any other type of mixing. We can generally write the rate of change for the mass fraction of the i-th element as follows:

$$\frac{\partial X_i}{\partial t} = \frac{A_i m_u}{\rho}\left(\sum_{kl} r_{kl,i} - \sum_j (1+\delta_{ij}) r_{ij}\right) + \text{mixing terms} \tag{2.7}$$

In Eq. 2.7 $r_{kl,i}$ is the rate at which the element i is created by the reaction between species k and l. r_{ij} is the rate at which i is destroyed, and the Kronecker delta accounts for those reactions that destroy two particles of the same element i. The last term generally accounts for every mixing that we listed above. Its explicit form depends on the theory considered to model any particular process, which is part of the discussion specifically dedicated to PARSEC (Section 2.2).

The equations presented in this section are in common to all evolution codes, but there are three main ways in which they can be solved. These approaches may be defined as non-simultaneous, partially simultaneous, and fully simultaneous (Stancliffe, 2006). The non-simultaneous approach converges to a solution of the structure equations only, which is then used to calculate the mixing and the nuclear burning and the new chemical profile is needed to find the structure of the next stellar model. Therefore, we say that the iterations needed for converging to a solution are made separately for structure and chemistry. PARSEC uses the non-simultaneous approach, which has particular relevance for Chapter 3. The partially simultaneous approach solves the structure for one iteration and then performs an iteration of

the chemistry. Such an alternating approach continues until the solver reaches convergence to a solution. Finally, the fully simultaneous method solves the structure and chemistry equations altogether. `MESA` (Paxton et al., 2011; Jermyn et al., 2023) and `FRANEC` (Chieffi et al., 1998) are examples of such code. For the non-simultaneous approach, besides `PARSEC`, the reader can check out `STAREVOL` (Siess et al., 2000; Siess, 2006) and `GENEC` (Eggenberger et al., 2008).

Regardless of the approach to solve the system of equations, determining its solution numerically is equivalent to a root-finding problem. Furthermore, the solution must be continuous until and at the boundaries: the star's center ($m = 0$) and surface ($m = M$). The central boundary is usually easier to deal with, and it is carried out by expanding in power series the solution of the system. This defines another set of equations that are matched with the original system. Setting the surface conditions is often trickier: the star is surrounded by a medium with non-zero density and temperature, despite being small and with negligible mass compared to the star's total mass. A convenient way is to identify the surface with the photosphere, namely the visible surface of the star. The system of equations can be adapted again to satisfy the photospheric assumptions and its solution is matched with the interior solution. In practice that is more than enough to fix the outer boundary, but one has to remember that in the atmosphere, the radiative diffusion approximation does not hold anymore. The best solution is to match a detailed stellar atmosphere model, which is however another different problem per se and it would need a separate program to be carried out.

2.2 The PAdova and tRieste Stellar Evolution Code

In this section, I revisit the general discussion of the equations in the `PARSEC` framework. I also include all the input physics in common with every model I calculated or mentioned in this thesis. For the rest of the manuscript, I use the term "structure" as the solution of the four structure equations (Eq.s 2.2, 2.3, 2.4 and 2.5), without including abundance profiles.

2.2.1 Method of solution

In `PARSEC` we divide the structure into three regions as in Figure 2.1: internal structure, envelope (or outer layers), and atmosphere. The central boundary is included in the internal structure as it is only one mesh point, but it still needs a separate set of equations.

For what concerns the internal structure, it obeys the four structure equations I presented in the previous section. However, we transform the variables into a more suitable set of coordinates (and the equations are rewritten accordingly). Our independent variable, equivalent to the mass coordinate m, reads:

$$q(m) = \ln\left(1 - \frac{m}{M}\right) \tag{2.8}$$

The unknown variables are transformed as follows:

$$\tilde{P} = \ln P \qquad \tilde{T} = \ln T \qquad \tilde{R} = \ln r \qquad \tilde{L} = \ln\left(1 + \frac{\ell}{L'}\right) \tag{2.9}$$

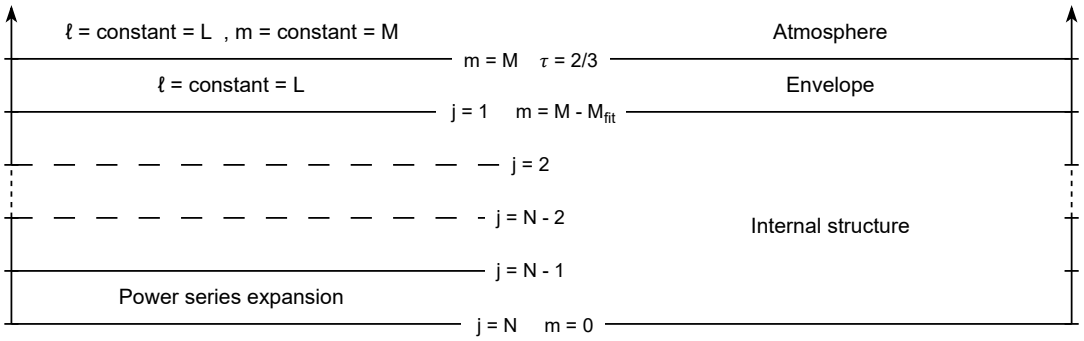

Fig. 2.1: Schematic grid implemented in PARSEC. The internal structure is divided into N meshpoints. The name of the corresponding region is on the right side of the diagram. On the left side, we report the approximation applied to the original set of structure equations in the corresponding boundary.

where L' is a positive constant that allows negative values of the luminosity ℓ granting that $|\ell| < L'$. These transformations are needed as the more intuitive ones span several orders of magnitude throughout the internal structure, which otherwise might be a source of numerical instabilities. However, it is convenient to keep referring to the physical quantities unless explicitly noted. To solve the star's structure in PARSEC, we adopt the Henyey method, which is an adaptation of the Newton-Raphson method usually employed in root-finding problems. Details can be found in the works by Henyey et al. (1959, 1964); Kippenhahn et al. (1967). The internal structure is divided into N mesh points, going from $j = 1$ at the outer boundary to $j = N$ at the center, while the envelope and atmosphere integration is carried out separately (see Section 2.2.2).

The variation of abundances, due to mixing or nuclear reactions, is carried out by the chemical routine. We adopt an implicit diffusive scheme, in which the rate of change of the i element reads (Sackmann et al., 1974):

$$\frac{\partial Y_i}{\partial t} = \frac{1}{\rho r^2}\frac{\partial}{\partial r}\left(r^2 \rho D \frac{\partial Y_i}{\partial r}\right) \pm \sum_j Y_j \lambda_k \pm \sum_{j \geq k} \frac{d_i}{1+\delta_{kl}} \rho N_A Y_j Y_k \langle \sigma v \rangle_{jk} \tag{2.10}$$

The first term collects every mixing process described by a diffusion coefficient. That may include convection, overshooting, rotation, and thermohaline mixing. The second term describes single particle decays from species j to k with rate λ_k, taking the positive sign if $i \neq j$ and $k = i$ and the negative if $i = j$. Finally, the third term corresponds to 2-body interactions between jk with the velocity-averaged cross section $\langle \sigma v \rangle_{jk}$. d_i is the number of i particles involved in the reaction, and the Kronecher delta δ_{kj} takes care of the double counting in the summation for $j = k$. Again, the positive and negative sign is associated with reactions that respectively produce or destroy the i element (i.e. $i \neq j, k$ and $i = j$ or k). Microscopic diffusion is treated separately with the method described by Thoul et al. (1994).

The outline of the program is presented in Figure 2.2. Starting from initial conditions or the previous model, the chemical routine solves Eq. 2.10 with timestep Δt for the model at time t. The structure of the model at age $t - \Delta t$ is modified by removing the top layers with a mass-loss

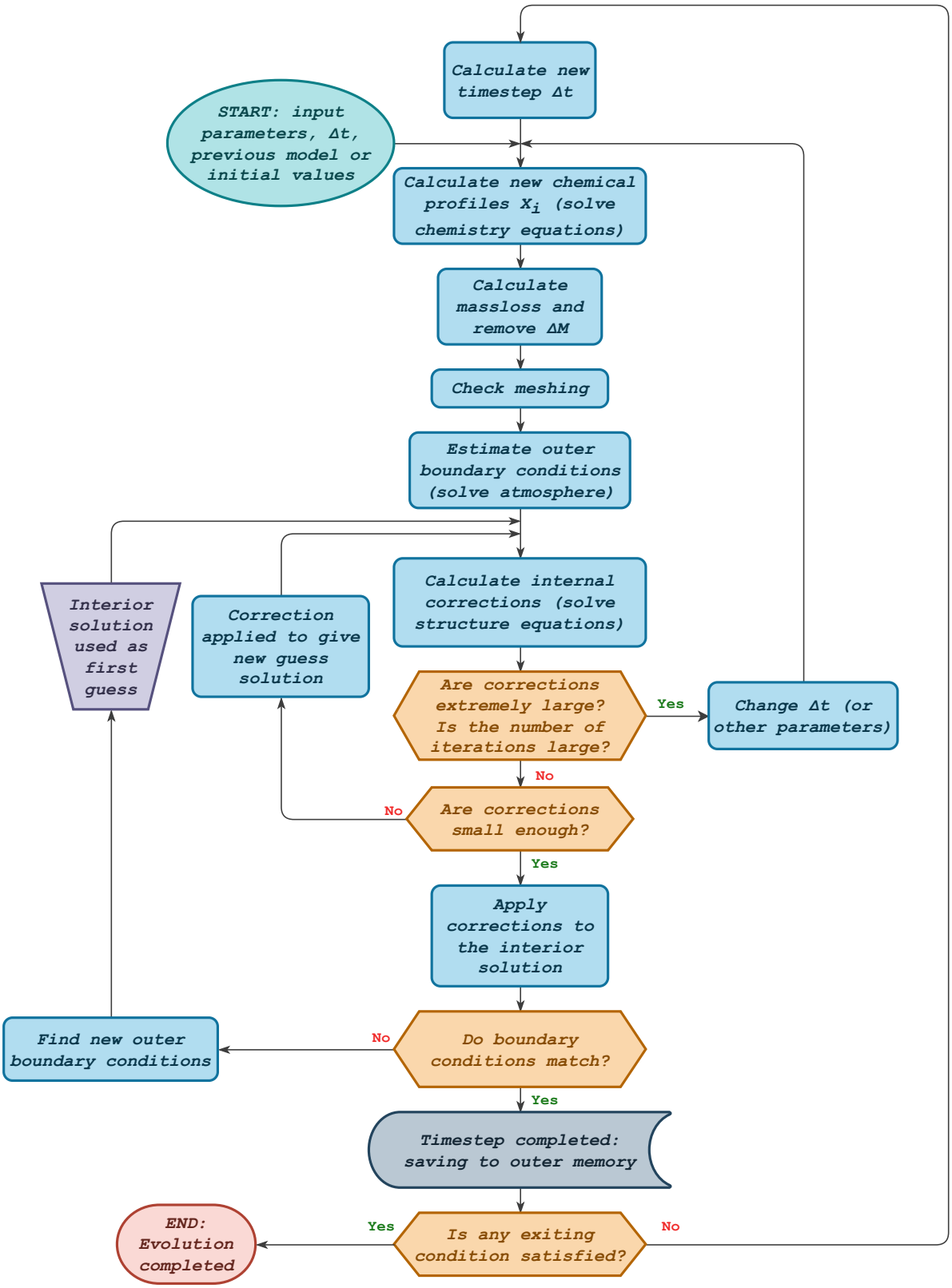

Fig. 2.2: Schematic flowchart of PARSEC. Revisited from the flowchart presented by Kippenhahn et al. (1967).

recipe and it is re-meshed if needed. Then PARSEC gives the outer boundary conditions for the structure at age t by using the previous structure as a first guess. It solves the interior structure, which is temporarily saved if it meets the desired accuracy. If the outer boundary conditions match the interior structure, the model is complete and the evolution proceeds by calculating a new timestep. Otherwise, the structure is used to calculate again the outer boundary and as a first guess for another whole iteration of the interior solution solver. The evolution finally stops if any exiting conditions are met or if the code cannot find a solution in case of too large corrections or divergence.

PARSEC uses a series of expressions to determine the timestep, which may vary depending on the evolutionary phase of the star, which are evaluated before entering the chemical evolution routine. These include for example, calculations of the characteristic timescales for hydrogen and helium burning in both core and shell phases, a series of tests to ensure that all variations are within acceptable limits, and estimates of a timestep that keeps these variations under control. Ultimately, PARSEC selects the smallest timestep from among all the proposed values and then blends it with the timestep from the previous model to smooth out any sudden variations. Each of these timestep expressions includes a multiplying constant that can be adjusted externally as an input parameter. This allows users to modify the relative weight of the various expressions to better suit different evolutionary scenarios, for instance when calculating low and intermediate-mass stars with respect to massive star tracks. For Section 3.2, it is important to mention the constant that multiplies the timestep associated with the hydrogen-burning shell, as this is typically the dominant factor (i.e., it yields the smallest timestep). I denote this constant as f_{T}.

2.2.2 Boundary conditions

The boundaries of the internal structure have to be treated separately. Although they have to satisfy the same equations, they must be adapted and, somehow, the user has to make choices that make the problem numerically solvable.

Central boundary. The center is defined as $m = 0$ and here the radius and luminosity must vanish, $r(0) = 0$ and $\ell(0) = 0$. The radial variable may seem ill-defined, but the central value of the radius never enters the equations needed to match the center to the internal structure. In the center proximity, we can expand the solution in power series and exploit the structure equation to substitute derivatives. This leads to the following equations, valid in the neighborhood of the center:

$$\tilde{r} = \ln\left(\frac{3m}{4\pi\rho_N}\right) \tag{2.11}$$

$$P = P_N - \frac{G}{2}\left(\frac{4\pi}{3}\right)^{1/3} \rho_N^{4/3} m^{2/3} \tag{2.12}$$

$$\tilde{L} = \ln\left(1 + \frac{m\left(\varepsilon_{\mathrm{nuc}} - \varepsilon_\nu + \varepsilon_{\mathrm{grav}}\right)_{j=N}}{L'}\right) \tag{2.13}$$

$$\tilde{T}_N - \tilde{T} = \nabla_N\left(\tilde{P}_N - \tilde{P}\right) \tag{2.14}$$

Quantities with subscript N are calculated at the center. In PARSEC, the only exception to the standard procedure of expanding in series is the Eq. 2.14, which instead comes from the definition of the temperature gradient. The four equations for the central boundary are solved and matched with the interior solution at $j = N - 1$.

Outer boundary. The star is surrounded by an atmosphere, which gives us the outer boundary condition. The atmosphere has negligible mass with respect to the total mass of the star and there are no nuclear reactions ($\ell = L$ = constant). In this regime, we can rewrite the hydrostatic equilibrium equation (Eq. 2.3), which reads:

$$\frac{\mathrm{d}\tau}{\mathrm{d}P} = \frac{\kappa r^2}{GM} \tag{2.15}$$

For the temperature stratification, we can consider a plane-parallel grey atmosphere. Respectively, it implies that the material properties depend only on the height in the atmosphere and the opacity does not depend on the frequency of the radiation. The latter is also called Rosseland approximation, which naturally leads to the use of the Rosseland mean opacity. These assumptions lead to the solution (Weiss et al., 2004):

$$T^4 = \frac{3}{4} T_{\mathrm{eff}}^4 \left[\tau + q(\tau)\right] \tag{2.16}$$

where $q(\tau)$ is the Hopf function (Hopf, 1934). In the famous Eddington approximation, $q(\tau) = 2/3$ from which we recover the usual definition of the photosphere as the layer at which $\tau = 2/3$ and $T = T_{\mathrm{eff}}$. However, in this more general case, the photosphere is identified by satisfying the definition of effective temperature:

$$T_{\mathrm{eff}}^4 = \frac{L}{4\pi\sigma R^2} \tag{2.17}$$

In the atmosphere $\ell = L$ and R are constant parameters, therefore equating Eq. 2.16 and Eq. 2.17 gives the limit on the optical depth $\tilde{\tau}$ that identifies the photosphere. Below the photosphere ($\tau > \tilde{\tau}$) we have an envelope region, which extends down to the fitting point $m = M_{\mathrm{fit}}$. The value of M_{fit} is set to prevent any nuclear burnings, so that, as in the atmosphere, $\ell = L$ = constant. Therefore, we can integrate all the structure equations but Eq. 2.4 starting from the conditions given by the atmosphere integration at the photosphere, and then they are matched with the interior solution. More details on the integration and matching of the outer layers with the interior solution are given by Kippenhahn et al. (1967).

2.2.3 Input physics

In this work, I call "input physics" every aspect that has to be provided by the user to PARSEC. Some of these inputs are needed to close out the system of equations (e.g. EOS, opacity), others instead refer to processes that are not directly included in the basic formulas (e.g. overshooting prescriptions and parameters, initial rotation rate). It is important to have a clear idea of the input physics included in a stellar evolution code, as it hides a lot of parameters whose value is not known a priori, and they must be calibrated. In this section, I describe how such processes

are implemented and which parameters they add to the picture. The values of the parameters presented here are valid for any track shown in this work if not explicitly specified.

Convective mixing. When radiation is not sufficient to transport all the energy from the interiors to the surface of the star, then (usually) convection sets in. Convection also implies mixing of the material, thus it affects both the structure and chemical equations directly. It is, naturally, a turbulent 3D phenomenon; to include it in a 1D code one has to resort to parametrizations, which may as well simplify the description of the process itself. First, we have to determine which layers of the star are convective. A simple consideration based on the buoyancy of hot bubbles in colder surroundings leads to the Schwarzschild criterion, stating that a medium is stable against convection if:

$$\nabla_{\rm rad} < \nabla_{\rm ad} \tag{2.18}$$

The latter is valid in a chemically homogeneous region. If this assumption is lifted, we get the Ledoux criterion instead:

$$\nabla_{\rm rad} < \nabla_{\rm ad} - \frac{\chi_\mu}{\chi_T}\nabla_\mu \tag{2.19}$$

where we used the definitions:

$$\chi_\mu = \left(\frac{\partial \log P}{\partial \log \mu}\right)_{\rho,T} \quad \chi_T = \left(\frac{\partial \log P}{\partial \log T}\right)_{\rho,\mu} \quad \nabla_\mu = \frac{{\rm d}\log P}{{\rm d}\log \mu} \tag{2.20}$$

Should one use the Schwarzschild or Ledoux criterion? The question naturally arises and the choice is not arbitrary a priori. Convection is efficient in mixing so that unstable regions are indeed homogeneous. Therefore, if we approach the border from inside the convective zone, the result should be the same. However, they often result in slightly different outcomes, and the use of one or the other may impact the code stability too. A detailed discussion is given by Gabriel et al. (2014), and the effects on the TP-AGB phase are briefly investigated by Addari (2020) suggesting worse convergence rates and damping TDU efficiency. `PARSEC` tests the stability of the layers with the Schwarzschild criterion for the whole star's evolution, which I kept considering the focus on the TP-AGB evolution. Now we want to answer the problem of how the bubbles behave and transport energy throughout the structure. Reducing a 3D phenomenon to 1D is not an easy task, and there are not many prescriptions available in the literature. The choice falls (almost inevitably) on the Mixing-Length Theory (Böhm-Vitense, 1958), which is based on the concept of the average length traveled by the convective bubbles from formation to dissipation:

$$l_{\rm mlt} = \alpha H_P \tag{2.21}$$

The actual formulas implemented in `PARSEC` can be found in Chapter 14 of Weiss et al. (2004), we just recall how to calculate the diffusion coefficient in the MLT framework, which contributes to Eq. 2.10:

$$D_{\rm mlt} = \frac{1}{3} v_{\rm mlt} l_{\rm mlt} \tag{2.22}$$

The MLT adds the parameter α, which is calibrated on the sun. The solar calibration (Bressan et al., 2012) results in $\alpha = 1.74$.

Overshooting. The convective neutrality given by the Schwarzchild (or Ledoux) criterion corresponds to the point at which the acceleration of the eddies vanishes. They may be able to overcome the boundary by inertia, polluting a radiative region. This process is called overshooting, which may take place at every convective boundary. It is common to include it at the core and envelope boundaries, while it is argued if it is effective at the PDCZ boundaries (Lattanzio et al., 2017). In this case, there is no strictly preferred prescription, as calibrations are not able to say which formula is best. Depending on the prescription adopted, the added free parameters can be calibrated, and the value is set on observed features. The core overshooting is treated as a ballistic process (Bressan et al., 1981), which I briefly recall here: the convective border corresponds to the radius at which the convective bubbles have zero net acceleration, and this model wants to determine the true convective border where the velocity of the bubbles is vanishing, assuming an adiabatic temperature gradient in the overshooting region. The ballistic velocity profile of the convective bubbles is found by numerically solving the following equation (Eq. 6 by Bressan et al. (1981)) in a region across the border of the convective core:

$$\frac{1}{3}\frac{\partial v_r^3}{\partial r} = \frac{1}{k}\frac{g}{T}\frac{\chi_T}{\chi_\rho}\frac{F_c}{c_P\rho} - \frac{g}{\mu}\frac{\chi_\mu}{\chi_\rho}\Delta\mu \cdot v_r \tag{2.23}$$

where k is a constant (assumed 2 to account for the contribution of both rising and descending convective elements), g is the local gravity acceleration, F_c is the convective energy flux, c_P is the heat capacity at constant pressure and $\Delta\mu$ is the difference of the mean molecular weight from the convective border. Solving Eq. 2.23 from below (where bubbles are accelerated) to above the border of the convective core (where they are slowed down) determines the real extension of the convective region in consideration.

In the envelope and at both borders of the PDCZ[1], I use an exponentially decaying diffusion coefficient, as suggested by hydrodynamical simulations of stellar envelopes (Freytag et al., 1996; Herwig, 2000):

$$D(r) = D_0 \exp\left(-2\frac{|r - r_0|}{f_{ov}H_p}\right) \qquad r_0 = r_{cnv} \pm f_{0,ov}H_p \tag{2.24}$$

which adds two free parameters (f_{ov} and $f_{0,ov}$) for every border (placed at radius r_{cnv} from the center). r_0 sets the radius at which the prescription sets in, and a minus or negative sign is taken accordingly to set r_0 in the interior of the corresponding convective region. The minimum value for the diffusion coefficient is set to $D_{min} = 10^3$ cm^2 s^{-1}, and no diffusion is considered if $D(r) < D_{min}$. To reduce the number of free parameters, I set $f_{ov} = 2f_{0,ov}$ (Choi et al., 2016). Concerning the value used for the various overshooting parameters, the calibration of f_{env} and f_{pdcz} in the TP-AGB phase is the main point of the recently published paper (Addari et al., 2024), thus we defer the discussion to Chapter 4. Instead, the efficiency of core and envelope overshooting prior to the TP-AGB phase is completely set on what has

[1] Lattanzio et al. (2017) suggests that the extent of the overshooting region in the PDCZ is minimal or negligible. While this may not be the most precise description, it offers a convenient and straightforward way to include extra mixing, provided the free parameters are calibrated to reproduce observable features.

been done in previous works (Bressan et al., 2012; Nguyen et al., 2022, and references therein). First, we identified that the minimum mass for having a convective core during the main sequence (without any core overshooting) is $M_{O1} = 1.22\ M_\odot$, therefore the other limiting mass is $M_{O2} = M_{O1} + 0.3\ M_\odot = 1.52\ M_\odot$. Details on the value of M_{O2} can be found in Bressan et al. (2012), and is determined by reproducing features in the color-magnitude diagram of M67 and NGC 419. These two limits allow us to define three overshooting regimes:

$$c_{ov} = \begin{cases} c_{ov,min} & \text{for} \quad M_{ini} \leq M_{O1} \\ c_{ov,min} + \dfrac{M_{ini} - M_{O1}}{M_{O2} - M_{O1}} \left(c_{ov,max} - c_{ov,min}\right) & \text{for} \quad M_{O1} < M_{ini} \leq M_{O2} \\ c_{ov,max} & \text{for} \quad M_{ini} > M_{O2} \end{cases} \tag{2.25}$$

where the parameter c_{ov} generally refers to the core or envelope overshooting efficiencies, always prior to the TP-AGB phase. For the core, the corresponding overshooting parameter λ_{ov} ranges from $\lambda_{min} = 0$ to $\lambda_{max} = 0.5$, but during the central He-burning stage we always set $\lambda_{ov} = \lambda_{max}$ to give consistent horizontal branch and AGB lifetimes with the R_2 ratio observed in globular clusters (Bressan et al., 1986; Constantino et al., 2016). Finally, for the envelope $f_{env,min} = 0.033$ and $f_{env,max} = 0.047$, which are the equivalent values of $\Lambda_{ov,min} = 0.5$ and $\Lambda_{ov,max} = 0.7$ in those PARSEC works where a penetrative undershooting prescription was used also for the envelope. The envelope overshooting has been calibrated in various works (Alongi et al., 1991; Christensen-Dalsgaard et al., 2011; Bressan et al., 2015; Fu et al., 2018) by observing the RGB bump luminosity and effective temperature width of blue loops. We will generally refer to the envelope overshooting efficiency calculated as in Eq. 2.25 as $f_{env} = 0.047^\star$ or "fiducial" value. A more detailed discussion on the penetrative undershooting and exponential overshooting schemes is presented in Section 2.2.5.

Chemistry. In PARSEC it is possible to provide any initial chemical composition, given that EOS, opacity, and nuclear reactions are consistent. For all tracks in this work, we refer to solar-scaled partitions (Caffau et al., 2011). We track 33 species: neutrons, ^{1}H, D, ^{3}He, ^{4}He, ^{7}Li, ^{7}Be, ^{12}C, ^{13}C, ^{14}N, ^{15}N, ^{16}O, ^{17}O, ^{18}O, ^{19}F, ^{20}Ne, ^{21}Ne, ^{22}Ne, ^{23}Na, ^{24}Mg, ^{25}Mg, ^{26}Mg, ^{27}Al, ^{28}Al, ^{29}Si, ^{30}S, ^{31}Ar, ^{40}Ca, ^{44}Ti, ^{48}Cr, ^{52}Fe, ^{56}Ni, ^{60}Zn. The choice is driven by the computational cost of a bigger network, as the listed elements are the main actors in the reactions that produce almost all the energy needed to sustain the star. Other isotopes may be involved only in nucleosynthesis, for which dedicated studies are needed and a full network or a post-processing scheme has to be provided. For the very same reason, we include 72 reactions in our nuclear network, listed in Table 2.1 with their respective references. The JINA REACLIB database (Cyburt et al., 2010) provides the reaction rate for all the reactions listed in Table 2.1 and their Q-value (eventually accounting for neutrinos), that are used to compute the energy generated by every interaction.

EOS and opacity. The equation of state and opacity functions are needed to close out the system of structure equations. In PARSEC we use EOS tables pre-computed with the freely available software FREEEOS (Irwin, 2012). It is also possible to use the same software on-the-fly, although increasing the computational time. Bressan et al. (2012) showed that the tables

Reaction	Reference	Reaction	Reference
$p(p,e^+\nu)d$	Cyburt et al. (2010)	$^{21}Ne(p,\gamma)^{22}Na$	Iliadis et al. (2010)
$p(d,\gamma)^3He$	Descouvemont et al. (2004)	$^{22}Ne(p,\gamma)^{23}Na$	Iliadis et al. (2010)
$^3He(^3He,2p)^4He$	Angulo et al. (1999)	$^{23}Na(p,^4He)^{20}Ne$	Iliadis et al. (2010)
$^4He(^3He,\gamma)^7Be$	Cyburt & Davids (2008)	$^{23}Na(p,\gamma)^{24}Mg$	Iliadis et al. (2010)
$^7Be(e^-,\gamma)^7Li$	Cyburt et al. (2010)	$^{24}Mg(p,\gamma)^{25}Al$	Iliadis et al. (2010)
$^7Li(p,^4He)^4He$	Descouvemont et al. (2004)	$^{25}Mg(p,\gamma)^{26}Al^g$	Iliadis et al. (2010)
$^7Be(p,\gamma)^8B$	Angulo et al. (1999)	$^{25}Mg(p,\gamma)^{26}Al^m$	Iliadis et al. (2010)
$^{12}C(p,\gamma)^{13}N$	Li et al. (2010)	$^{26}Mg(p,\gamma)^{27}Al$	Iliadis et al. (2010)
$^{13}N(\beta^+,e^+\nu)^{13}C$	Li et al. (2010)	$^{27}Al(p,^4He)^{24}Mg$	Iliadis et al. (2010)
$^{13}C(p,\gamma)^{14}N$	Angulo et al. (1999)	$^{27}Al(p,\gamma)^{28}Si$	Iliadis et al. (2010)
$^{14}N(p,\gamma)^{15}O$	Imbriani et al. (2005)	$^{26}Al^g(p,\gamma)^{27}Si$	Iliadis et al. (2010)
$^{15}N(p,^4He)^{12}C$	Angulo et al. (1999)	$^{26}Al^g(\beta^+,e^+\nu)^{26}Mg$	Tuli (2012)
$^{15}N(p,\gamma)^{16}O$	Leblanc et al. (2010)	$^{12}C(^{12}C,n)^{23}Mg$	Caughlan & Fowler (1988)
$^{16}O(p,\gamma)^{17}F$	Iliadis et al. (2008)	$^{12}C(^{12}C,p)^{23}Na$	Caughlan & Fowler (1988)
$^{17}O(p,^4He)^{14}N$	Iliadis et al. (2010)	$^{12}C(^{12}C,^4He)^{20}Ne$	Caughlan & Fowler (1988)
$^{17}O(p,\gamma)^{18}F$	Iliadis et al. (2010)	$^{20}Ne(\gamma,^4He)^{16}O$	Costantini et al. (2010)
$^{18}O(p,^4He)^{15}N$	Iliadis et al. (2010)	$^{16}O(^{16}O,^4He)^{28}Si$	Caughlan & Fowler (1988)
$^{18}O(p,\gamma)^{19}F$	Iliadis et al. (2010)	$^{28}Si(^4He,\gamma)^{32}S$	Cyburt et al. (2010)
$^{19}F(p,^4He)^{16}O$	Angulo et al. (1999)	$^{32}S(^4He,\gamma)^{36}Ar$	Cyburt et al. (2010)
$^{19}F(p,\gamma)^{20}Ne$	Angulo et al. (1999)	$^{36}Ar(^4He,\gamma)^{40}Ca$	Cyburt et al. (2010)
$^4He(2^4He,\gamma)^{12}C$	Fynbo et al. (2005)	$^{40}Ca(^4He,\gamma)^{44}Ti$	Cyburt et al. (2012)
$^{12}C(^4He,\gamma)^{16}O$	Cyburt et al. (2012)	$^{44}Ti(^4He,\gamma)^{48}Cr$	Cyburt et al. (2010)
$^{14}N(^4He,\gamma)^{18}F$	Iliadis et al. (2010)	$^{48}Cr(^4He,\gamma)^{52}Fe$	Cyburt et al. (2010)
$^{15}F(^4He,\gamma)^{19}F$	Iliadis et al. (2010)	$^{52}Fe(^4He,\gamma)^{56}Ni$	Cyburt et al. (2010)
$^{16}O(^4He,\gamma)^{20}Ne$	Costantini et al. (2010)	$^{56}Ni(^4He,\gamma)^{60}Zn$	Cyburt et al. (2010)
$^{18}O(^4He,\gamma)^{22}Ne$	Iliadis et al. (2010)	$^{16}O(\gamma,^4He)^{12}C$	Costantini et al. (2010)
$^{20}Ne(^4He,\gamma)^{24}Mg$	Iliadis et al. (2010)	$^{24}Mg(\gamma,^4He)^{20}Ne$	Iliadis et al. (2010)
$^{22}Ne(^4He,\gamma)^{26}Mg$	Iliadis et al. (2010)	$^{28}Si(\gamma,^4He)^{24}Mg$	Strandberg et al. (2008)
$^{24}Mg(^4He,\gamma)^{28}Si$	Strandberg et al. (2008)	$^{32}S(\gamma,^4He)^{28}Si$	Cyburt et al. (2010)
$^{13}C(^4He,n)^{16}O$	Heil et al. (2008)	$^{36}Ar(\gamma,^4He)^{32}S$	Cyburt et al. (2010)
$^{17}O(^4He,n)^{20}Ne$	Angulo et al. (1999)	$^{40}Ca(\gamma,^4He)^{36}Ar$	Cyburt et al. (2010)
$^{18}O(^4He,n)^{21}Ne$	Angulo et al. (1999)	$^{44}Ti(\gamma,^4He)^{40}Ca$	Costantini et al. (2010)
$^{21}Ne(^4He,n)^{24}Mg$	Angulo et al. (1999)	$^{48}Cr(\gamma,^4He)^{44}Ti$	Cyburt et al. (2010)
$^{22}Ne(^4He,n)^{25}Mg$	Iliadis et al. (2010)	$^{52}Fe(\gamma,^4He)^{44}Ti$	Cyburt et al. (2010)
$^{25}Mg(^4He,n)^{28}Si$	Angulo et al. (1999)	$^{56}Ni(\gamma,^4He)^{52}Fe$	Cyburt et al. (2010)
$^{20}Ne(p,\gamma)^{21}Na$	Iliadis et al. (2010)	$^{60}Zn(\gamma,^4He)^{56}Ni$	Cyburt et al. (2010)

Tab. 2.1: List of nuclear reactions included in PARSEC. We reported the specific reference for each reaction, but we follow the recommended rates from the JINA REACLIB database (Cyburt et al., 2010).

are accurate enough to avoid directly calling FREEEOS during the evolution. There are two types of EOS tables corresponding to hydrogen-rich and hydrogen-depleted mixtures, which are interpolated to get all thermodynamic quantities for each P and T at any meshpoint. The opacity κ is a fundamental quantity that describes how matter interact with radiation, and it works similarly to the EOS. We provide PARSEC with pre-computed tables, again for hydrogen-rich and hydrogen-depleted mixtures. Details on what hydrogen-rich and hydrogen-depleted mixture really mean for EOS and opacity are given later in Section 3.1. Opacity tables in the low temperature regime ($\mathrm{Log}\,(T/\mathrm{K}) < 4.2$) are calculated with ÆSOPUS (Marigo & Aringer, 2009; Marigo et al., 2022a). For this project, I updated them to track the variation of carbon, nitrogen, and oxygen abundances due to consecutive dredge-up events and hot-bottom burning (Section 3.1). In the high-temperature regime, $4.2 \leq \mathrm{Log}(T/\mathrm{K}) \leq 8.7$, we use the opacity tables

provided by the Opacity Project At Livermore (OPAL; Iglesias & Rogers, 1996). Conductive opacities are incorporated following Itoh et al. (2008). More details on the opacity tables are given in Section 3.1. The EOS and opacity module are called for every meshpoint at every iteration of the structure-solving routine.

Mass loss. In PARSEC any stellar wind prescription can be easily implemented in the mass-loss module[2], which is called right before solving the structure equations with the new chemical profiles (see flowchart in Figure 2.2). The mass loss is a critical aspect that greatly affects the lifetime of the star. Every track in this work (unless specified) follows the recipe introduced by (Marigo et al., 2020). No stellar wind is considered up to the end of the MS, from there to the end of core He burning we use a Reimers' formula with efficiency $\eta_R = 0.2$ (Reimers, 1975). After central He burning is completed and as long as the luminosity is below the tip of the RGB ($\mathrm{Log}(L/\mathrm{L}_\odot) \sim 3.5$) we use the wind by Cranmer & Saar (2011) who assumes an Alfvén wave-driven mechanism. Above this threshold, if the star's surface is oxygen-rich (C/O < 1) we use the Blöcker's formula (Bloecker, 1995) with $\eta_B = 0.01$, which applies for Mira-like stars where mass-loss is thought to be driven by radiation pressure on oxygen dust. Conversely, when the star becomes a carbon star, we also calculate the carbon excess:

$$\mathrm{C} - \mathrm{O} = \log\left(\frac{Y_\mathrm{C} - Y_\mathrm{O}}{Y_\mathrm{H}}\right) + 12 \tag{2.26}$$

If the carbon excess is small, the star cannot form carbon dust and the wind is only sustained by pulsations (Winters et al., 2000). In this case, we use the recipe proposed by Bedijn (1988):

$$\dot{M} = \exp\left(a M^b R^c\right) \tag{2.27}$$

where the total mass M and the radius R are in solar units and the parameters $a = -789$, $b = 0.558$ and $c = -0.676$ are found by fitting the dust-free pulsating atmosphere models by Bowen (1988). Finally, if the carbon excess is large enough we use state-of-the-art dynamical atmosphere models by Mattsson et al. (2010); Eriksson et al. (2014); Bladh et al. (2019). The minimum value of C − O to trigger the carbon-dust driven wind depends on current mass, luminosity, and effective temperature, but it places somewhere in the range $\sim 8.2 - 9.2$.

2.2.4 Other possibilities

In this section, I want to briefly list and comment on other possibilities that are implemented in PARSEC, which are not used in this project. With version V2.0 (Costa et al., 2019; Costa, 2019; Nguyen et al., 2022) there have been many additions and improvements, the main one might be the addition of stellar rotation. Under the proper assumptions and approximation, a 3D phenomenon as rotation can be implemented in a 1D code. The scheme included in PARSEC V2.0 follows the description by Meynet & Maeder (1997); Maeder (2009) and it is fully developed in our framework in the thesis by Costa (2019). Rotation introduces a series of critical effects on the stars, as the transport of angular momentum, changes the effective gravity

[2] I recently rewrote the module to allow much more flexibility in adding new recipes.

felt by the structure (e.g. enhancing the mass loss) and contributes to the mixing of elements. All my models are calculated with a zero rate of angular rotation throughout the whole evolution. Still, we somehow account for the net effect of rotation on the core mass at the beginning of the AGB phase with our core overshooting prescription, as discussed by Costa et al. (2019). This choice simplifies the picture and reduces the degeneration in the TP-AGB calibration, besides lowering the computational time.

Even without convective mixing and rotation, elements can diffuse out of the surface by mainly three processes: microscopic diffusion, where the elements would naturally distribute to homogenize the concentration; gravitational settling, which is just a buoyancy effect, namely heavier elements tend to sink in the structure; radiative levitation, where the radiation pressure might lift some species to the surface. All these processes are not separated and they interact with each other, but they are very slow compared to convection. For this reason, they are not important when the star has extended convective regions (usually the envelope) or when the lifetimes is short (e.g. massive stars). In PARSEC diffusion is implemented by following the scheme presented by Thoul et al. (1994), which includes microscopic diffusion with gravitational settling. However, I do not include the effect of microscopic diffusion, as the abundance changes are limited and the deep convective envelope would anyway erase them after the main sequence.

Finally, there is the possibility of including the effects of thermohaline mixing. Generally, in a star, the mean molecular weight gradient is positive (i.e. μ increases inward), which means that the particles are, on average, heavier the deeper you go inside the structure. However, the reaction ^{3}He(^{3}He,2p)^{4}He converts two particles into three. This effectively means that the (approximately) same weight is distributed in a larger number of particles, which lowers the mean molecular weight and in that region ∇_μ becomes negative. This causes the region to be unstable and the thermohaline mixing acts against this gradient inversion. The effect is relevant especially at the bottom boundary of hydrogen-burning shells, as in the interior or in burning cores the two protons produced by the reaction are quickly reprocessed. Then, it might affect red giant stars both on the RGB and on the AGB. In the first case, studies have already hinted towards a visible effect of thermohaline mixing (Charbonnel & Zahn, 2007; Charbonnel et al., 2020), although the free parameter is not well constrained as its value ranges from order unity to 1000. On the AGB there is not much information available, but models suggest that the evolution timescale is too short for thermohaline mixing to have a sensible effect compared to the third dredge-up (Cantiello & Langer, 2010; Addari, 2020). For this reason, I choose not to include the effects of thermohaline mixing.

2.2.5 Details on the envelope overshooting

This final section wants to dive deeper into the overshooting prescriptions mentioned earlier for the bottom of the convective envelope. On one side, we have the usual PARSEC prescription described in various works (Alongi et al., 1991; Bressan et al., 2012; Tang et al., 2014; Costa et al., 2019), which I called here penetrative undershooting. The only free parameter is the extent of the overshooting region, or in other words, the mean free path that the convective bubbles can

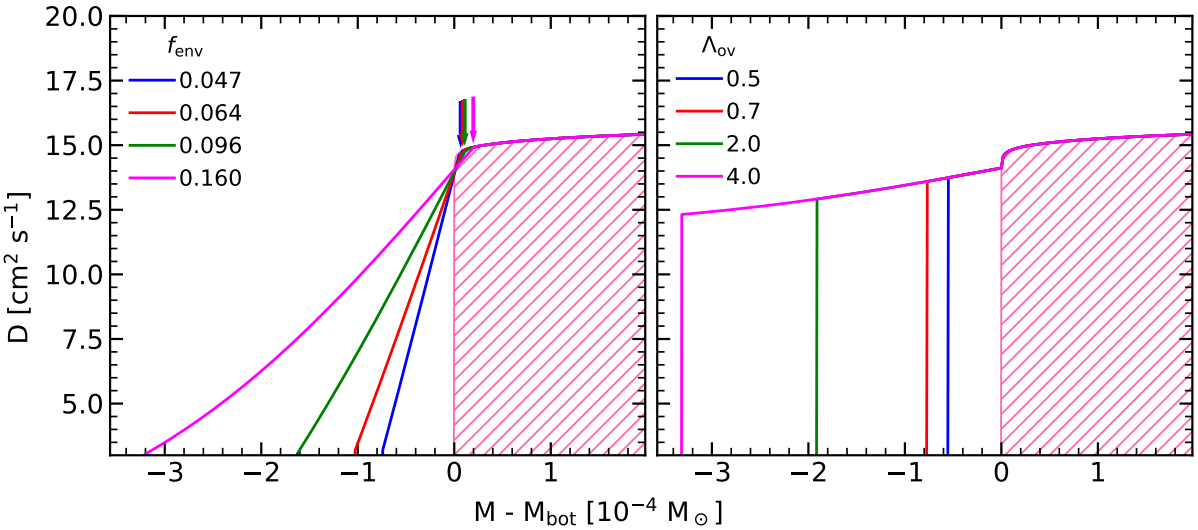

Fig. 2.3: Base-10 logarithm of the diffusion coefficient for exponential overshooting (left panel) and penetrative undershooting (right panel) for a model during the interpulse phase. The arrows mark the beginning of the overshooting region in the exponential case, namely r_0 with corresponding colors. The hatched pink region shows the convectively unstable region according to the Schwartzchild criterion. The x-axis is the mass coordinate with an offset equal to the mass of the bottom of the convective envelope $M_{\rm bot}$, in 10^{-4} $M_\odot$ units.

travel in the radiative region to produce sensible mixing. In particular, the diffusion coefficient is calculated as:

$$D(r) = D_0 \exp\left(-2\frac{r_{\rm bce} - r}{H_{\rm p}}\right) \qquad r_{\rm bce} - \Lambda_{\rm ov} H_{\rm p} \leq r \leq r_{\rm bce} \tag{2.28}$$

The formula is the same as for exponential overshooting Eq. 2.24 but I want to stress a few important caveats. First, the radius at which the prescription is applied is equal to the bottom of the convective envelope $r_0 = r_{\rm bce}$, meaning that it does not begin inside the convective envelope as in Eq. 2.24.; second, the decaying slope is always equal to $f_{\rm ov} = 1$ which makes the shape of the diffusion coefficient almost flat and still quite large all down to the maximum extension of $\Lambda_{\rm ov} H_{\rm p}$. We could say that this prescription is a special case of exponential overshooting, but the chosen parameters make it behave sensibly different compared to the literature's most common values for $f_{\rm ov}$. The penetrative undershooting prescription focus is the extension of the overshooting region, while the exponential overshooting focuses more on the slope of the diffusion coefficient.

The differences are shown in Figure 2.3, where the left panel also highlights no sensible effects on r_0 with different $f_{\rm env}$ for the exponential overshooting prescription. The initial point from which I apply Eq. 2.24 does not move far from the border of the convective envelope, meaning that $f_{\rm env}$ only sets the slope of the diffusion coefficient profile for the values I investigated. On the other hand, the flatness of the penetrative undershooting is part of the reason why I have chosen exponential overshooting: I noted that in the most massive AGBs ($M_{\rm ini} \gtrsim 3$ $M_\odot$) increasing the value of $\Lambda_{\rm ov}$ caused the H-shell to be completely eaten out and

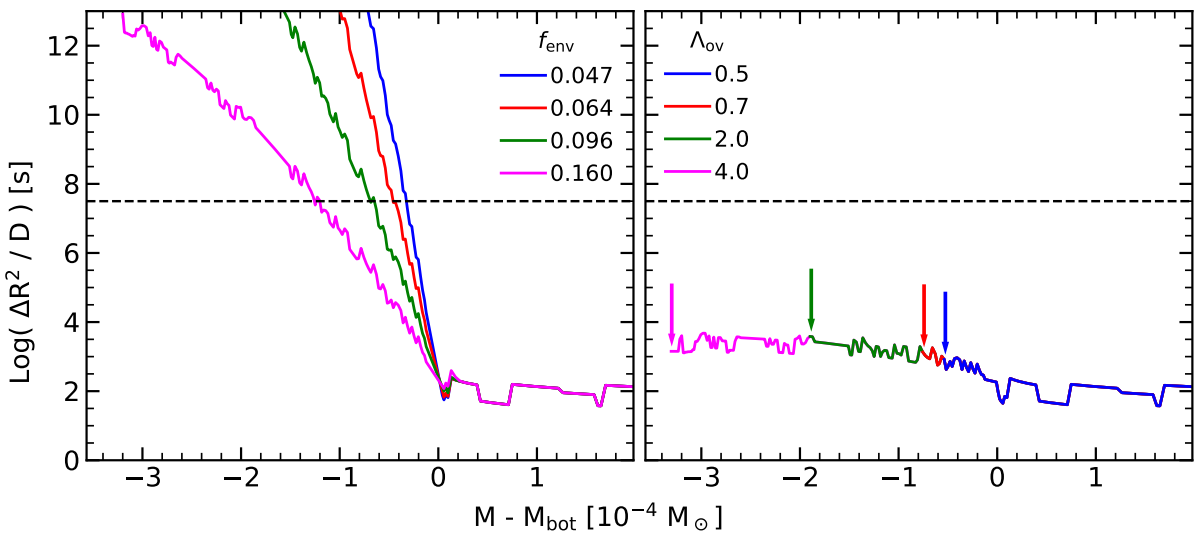

Fig. 2.4: Mixing timescale for exponential overshooting (left panel) and penetrative undershooting (right panel) for a model during the interpulse phase. The arrows mark the extent of the penetrative undershooting region, with corresponding colors. The horizontal dashed line is drawn at 1 yr. The x-axis is the mass coordinate with an offset equal to the mass of the bottom of the convective envelope, in 10^{-4} $M_\odot$ units.

preventing the core mass to grow at all during interpulses, which also effectively blocked the occurrence of thermal pulses.

Only the diffusion coefficient cannot tell the extent of the region effectively mixed in a single timestep, because it depends on its width (in time). That is more effectively shown in Figure 2.4, where I calculated the mixing timescale. From a purely dimensional analysis, we can define it as:

$$\Delta t_{\rm mix} \sim \frac{\Delta R^2}{D} \tag{2.29}$$

where ΔR is the radial distance between two mesh points and D is the average diffusion coefficient in between them. $\Delta t_{\rm mix}$ gives a rough estimate of the time needed to mix material between adjacent grid cells during a timestep. Taking the 1-year line as a reference timestep during third dredge-up episodes, we can see that for penetrative undershooting the mixing timescale is very small, therefore the material gets mixed quickly in the whole overshooting region. On the other hand, in the exponential overshooting $\Delta t_{\rm mix}$ quickly increases over the dashed line, therefore depending on the Δt of the model, the material may not be mixed completely down to the maximum extension of the overshooting region, corresponding to the limit of $D = 10^3$ cm^2 s^{-1}.

How can we compare the extension of the overshooting zone for these two prescriptions? In literature there are indications for a conversion factor between $f_{\rm env}$ and $\Lambda_{\rm ov}$ is $\sim 10 - 15$ (Claret & Torres, 2017, Section 5.1, and references therein). We can get inspiration on the way the envelope overshooting is usually calibrated (Bressan et al., 2012; Tang et al., 2014): in low-mass stars, the RGB bump luminosity is strongly dependent on the extent of the overshooting region. Similarly, for stars somewhat close to the boundary of intermediate-mass and massive

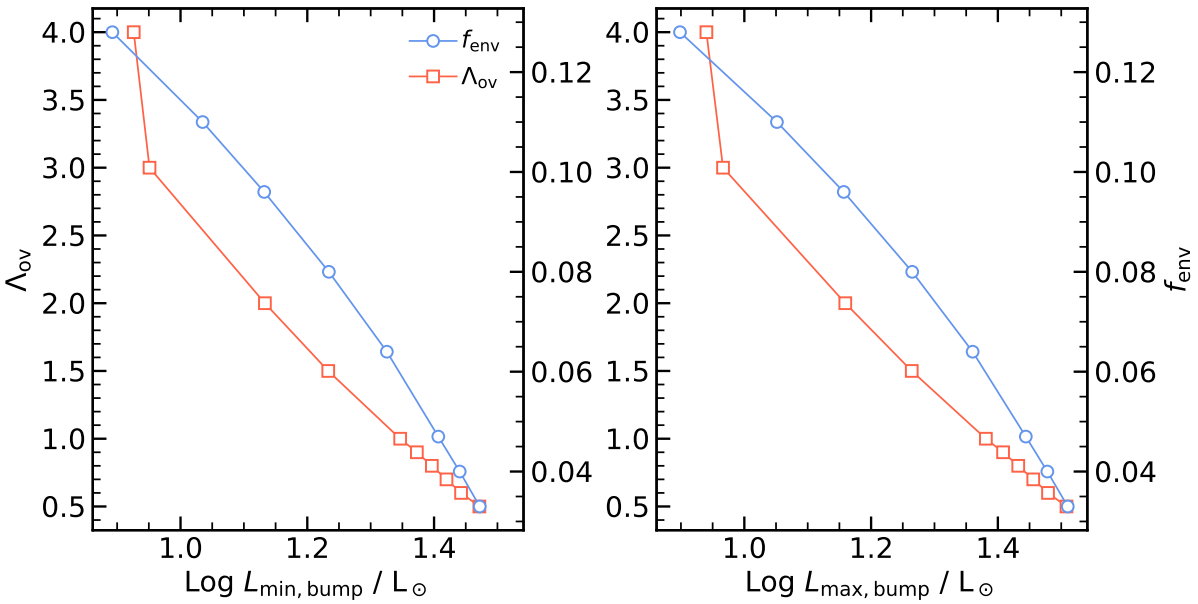

Fig. 2.5: Minimum (left panel) and maximum (right panel) bump luminosity for a 0.9 $M_\odot$ and $Z = 0.006$. The blue line with circles refers to the tracks with exponential overshooting (right y-axis) and the red line with boxes to the penetrative undershooting (left y-axis).

classes, the overshooting affects the width of blue loops. Therefore, I calculated models with both prescriptions and compared them to get the same RGB bump luminosity and temperature width of blue loop. My prototype models in this case are at $Z = 0.006$ (to enhance the effects of the RGB bump) absolute metallicity and have no mass loss, and respectively I evolve a 0.9 $M_\odot$ and 10 $M_\odot$ stars. For the low-mass prototype, we can easily identify the maximum and minimum luminosity in the bump (see the small window in Figure 1.1) and compare the values for the two prescriptions in Figure 2.5. As the extent of the overshooting region increases (for any prescription), the luminosity of the bump decreases because the first dredge-up occurs earlier. The plots in Figure 2.5 give a visual way to convert from one prescription to the other: the intersection between the two curves (f_{env} and Λ_{ov}) and any vertical line will identify the values for the overshooting parameters that give the same bump luminosity. We can follow this procedure and plot the result for any given luminosity, with a linear interpolation for the values of the parameters that have not been explored with a track. This is shown in Figure 2.6: the two curves, corresponding to the minimum and maximum luminosity give the same result, which is a good sanity check. I verified that a parabolic fit is a good representation for the curves for $f_{env} \lesssim 0.12$ and $\Lambda_{ov} \lesssim 3$, while a simple linear fit is not enough to give an accurate conversion. The curve becomes steeper for bigger f_{env} and Λ_{ov} because the star becomes effectively fully convective, as the overshooting region eats the newly developed helium core. Finally, from Figure 2.6 we can also see that, as mentioned above in Section 2.2.3, $f_{env} = 0.033$ corresponds to $\Lambda_{ov} = 0.5$, and $f_{env} = 0.047$ to $\Lambda_{ov} = 0.7$.

I now want to discuss the same conversion formula retrieved comparing the width of blue loops. In the stellar evolution brief introduction, I discussed only the low- and intermediate-mass

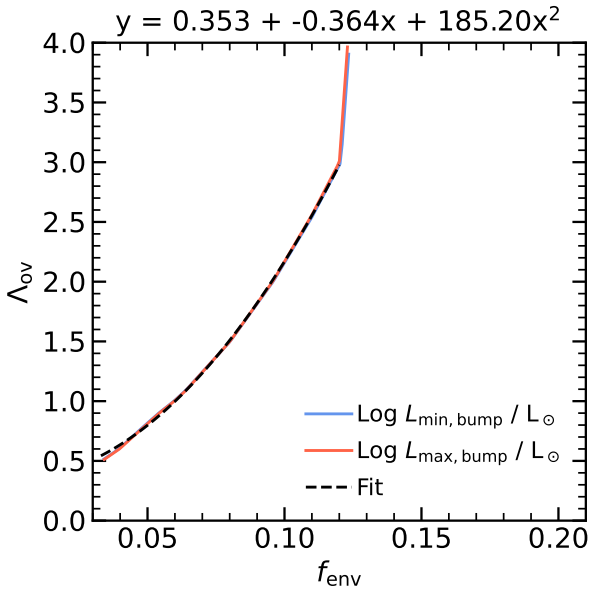

Fig. 2.6: Conversion between f_{env} and Λ_{ov} based on the RGB bump luminosity. Blue and red lines refer to the minimum and maximum luminosity, respectively. The dashed black line shows a fit with a parabola, given in the title.

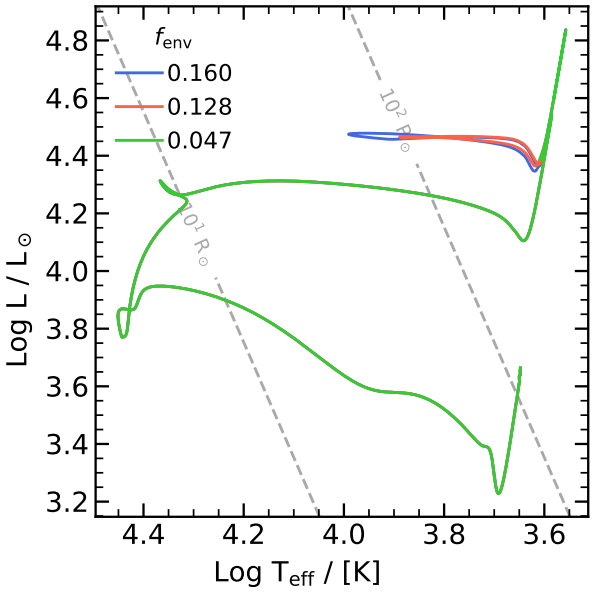

Fig. 2.7: H-R diagram for a 10 $M_\odot$ track and $Z = 0.006$, with different parameters for exponential overshooting. The width of the loop for the track with $f_{env} = 0.047$ is so small that is not visible in the figure.

stars, thus Figure 2.7 shows a prototype massive star of 10 $M_\odot$ in the H-R diagram, for three values of f_{env}. Blue loops occur during the central He-burning phase of intermediate-mass and massive stars (a detailed discussion is given by Tang et al. (2014)) and happen to cross the instability strip, explaining the pulsating behavior of Cepheids. Details on the process driving the loops and the parameters that affect them are out of the scope of this work, for now, I will focus on the extent of envelope overshooting. As Λ_{ov} (or f_{env}) increases, the effective temperature width of the blue loop considerably increases, as shown in the left panel of Fig 2.8. At $\Lambda_{ov} = 1.0$ and $f_{env} = 0.125$ there is a sudden increase from widths of less than 100 K (basically no loop) to more than 3000 K, which quickly saturates close to 10000 K. The idea is the same as before: with the intersection of the two curves with vertical lines we can visually identify the correspondence between the two overshooting prescriptions. Again, I can use linear interpolation to fill the values not explored with full tracks, and plot the conversion curve in the right panel Figure 2.8. Compared with the conversion curve done with the RGB bump, we can see how the curve is now shallower, meaning that for the same f_{env} the corresponding Λ_{ov} is smaller. Physically, this means that the region effectively mixed with the exponential overshooting scheme is smaller in the case of a massive star during the blue loop than the low-mass case in the RGB bump. In this second case, the conversion factor (roughly the slope of the linear fit) is closer to what is currently present in literature (Claret & Torres, 2017). Again, at some point the blue loop saturates and all the models give roughly the same width for any parameter.

Finally, this discussion on the overshooting prescription does not want to assess the best

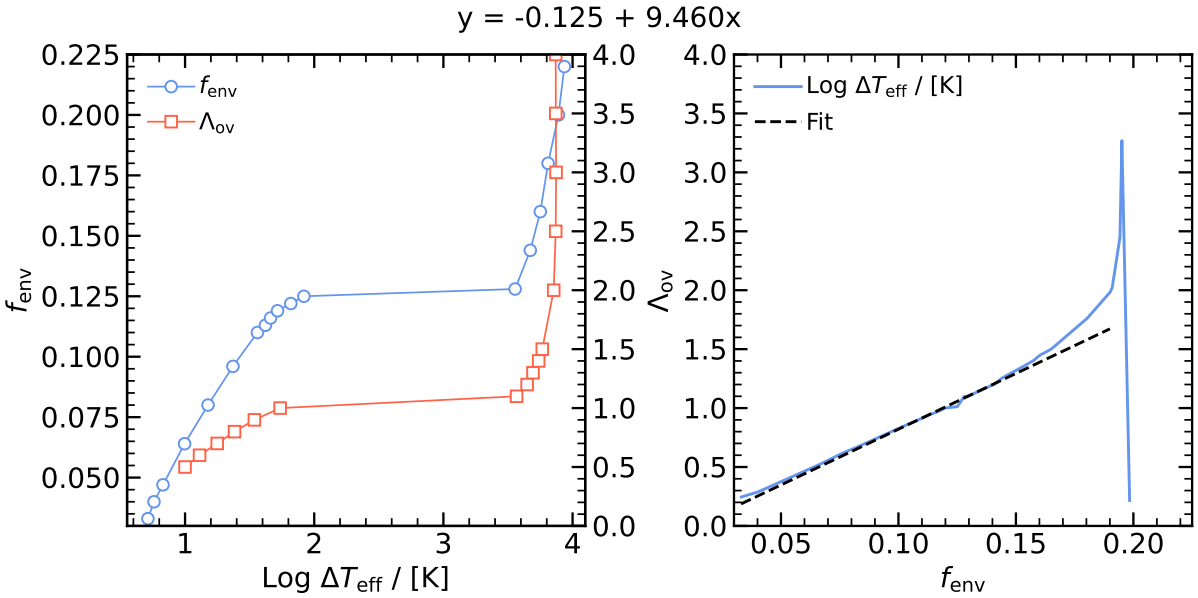

Fig. 2.8: Conversion between f_{env} and Λ_{ov} based on the effective temperature width of blue loop of a 10 $M_\odot$ and $Z = 0.006$ track. Left panel: f_{env} (blue circles) and Λ_{ov} (red squares) against the width of the blue loop. Right panel: conversion curve between the two overshooting parameters. The black dashed line is a linear fit that approximates the interpolation.

(or the correct!) prescription to use in stellar evolution codes. Instead, I wanted to show that after choosing any one of them, careful calibration has to be carried out with observed features, and then a comparison can be carried out to understand better the characteristics of any specific recipe.

CHAPTER 3

Numerical Methods for AGB evolution

In this Ph.D. project, I focused much of the effort in preparing and improving PARSEC to handle TP-AGB evolution, which is notoriously computationally intensive. In this Chapter, I describe the updates and numerical methods I implemented specifically for this stage of evolution and that have been employed in the computation of most of the tracks of the published work Addari et al. (2024) discussed in Chapter 4.

3.1 Updates on opacity tables

In this section, I want to discuss the inclusion of new opacity tables for computing the AGB evolution. I have already briefly discussed how opacity tables are used by PARSEC in Section 2.2.3, and I start by providing more detailed information on the standard set of tables.

Regardless of the source (e.g. low-temperature or high-temperature opacities), opacity tables are of two types: hydrogen-rich and hydrogen-depleted. The first type (Type I) gathers all those tables with fixed metallicity and hydrogen abundance nodes $X_{\rm H} \geq 0$ where the remaining abundance is all attributed to helium. For instance, if $Z = 0.01$ and the hydrogen nodes are $X = \{0, 0.3, 0.6, 0.9\}$, for those four opacity tables we will have $Y = \{0.99, 0.69, 0.39, 0.09\}$. Type I tables are used in those layers where hydrogen is present, as the main effect on opacity is due to variation of hydrogen and helium, and the effect of other metals is taken into account by interpolating in metallicity as a whole. To account for the proper contribution of other elements to the opacity in hydrogen-depleted layers, we use Type II tables which have nodes in metal enrichment dZ. For instance, if the reference $Z = 0.01$ and the nodes in metal enrichment are $\mathrm{d}Z = \{0, 0.3, 0.6, 0.9\}$, the corresponding helium values are $Y = \{0.99, 0.69, 0.39, 0.09\}$ and $X = 0$ always but we also have to assess the composition of the metal-enriched contribution. Ideally, we want to track the change of every element, as any one of them contributes differently to the opacity, but this would need a tool that computes the opacity (and the EOS too) on the fly

with any given chemical composition. That is theoretically possible already with AESOPUS, but currently, no high-T opacity group freely provides a similar tool, and in any case, that would be extremely time-consuming. Therefore, even though different variations are indeed happening inside the enriched part, we realize that due to the standard sequence of the main burning stages, the metal enrichment is mostly due to carbon and oxygen. To limit the number of tables to compute, we include three tables for each value of the metal enrichment: the first attributes all the contribution to an oxygen enrichment $\mathrm{d}Z = \mathrm{d}X_\mathrm{O}$, the second is the analog for carbon $\mathrm{d}Z = \mathrm{d}X_\mathrm{C}$ and the third one is where the enrichment is split in half between the two $\mathrm{d}Z/2 = \mathrm{d}X_\mathrm{O}$ and $\mathrm{d}Z/2 = \mathrm{d}X_\mathrm{C}$. Therefore, with the example nodes for the Type II tables, we get 10 tables, because for $\mathrm{d}Z = 0$ there is only one table. In most cases, this approach is accurate enough to estimate the opacity in the stellar matter, as the surface composition does not sensibly change (for low and intermediate-mass before the TP-AGB) or the surface is so hot that electron scattering and conduction are the main sources of opacity in the whole structure (for evolved massive stars that lost their hydrogen envelope).

However, regarding TP-AGB stars, TDU can considerably enrich the surface in C, O (ash of the helium burning), and N (from hydrogen burning). Still, hydrogen is one of the main elements in the surface chemical composition, so we would keep using the Type I tables even though the CNO element abundance is sensibly changed. To account for this effect, we calculated new low-temperature opacity tables (Type I) with ÆSOPUS (Marigo & Aringer, 2009; Marigo et al., 2022a) with nodes tracking the abundance variation of carbon, oxygen, and nitrogen. The variables we use to track those elements are:

$$f_\mathrm{CO} = \mathrm{Log}\left(\frac{Y_\mathrm{C}}{Y_\mathrm{O}}\right) - \mathrm{Log}\left(\frac{Y_\mathrm{C}}{Y_\mathrm{O}}\right)_\odot \tag{3.1}$$

$$f_\mathrm{C} = \mathrm{Log}\left(\frac{Y_\mathrm{C}}{Y_{\mathrm{C},\odot}}\right) \tag{3.2}$$

$$f_\mathrm{N} = \mathrm{Log}\left(\frac{Y_\mathrm{N}}{Y_{\mathrm{N},\odot}}\right) \tag{3.3}$$

where Y_C, Y_O, and Y_N are the number abundances accounting for the main isotopes of each element. These new tables aim to estimate the opacity close to the surface, at temperatures $\mathrm{Log}(T/\mathrm{K}) < 4.2$, therefore the chosen nodes are:

$$\begin{aligned}
X &= \{0.5, 0.6, 0.7, 0.8\} \quad (4 \text{ values}) \\
f_\mathrm{CO} &= \{-1, -0.5, 0, 0.2, 0.232, 0.251, 0.260, 0.273, 0.374, 0.561, 0.959\} \quad (11 \text{ values}) \\
f_\mathrm{C} &= \{-1, -0.5, 0, 0.2, 0.232, 0.251, 0.260, 0.273, 0.374, 0.561, 0.959\} \quad (11 \text{ values}) \\
f_\mathrm{N} &= \{0, 0.42, 0.85, 1.27, 1.7\} \quad (5 \text{ values})
\end{aligned}$$

The combination is optimized for tracking accurately the shift from oxygen- to carbon-rich composition, which is the critical period where the TP-AGB star move rapidly to cooler temperatures,

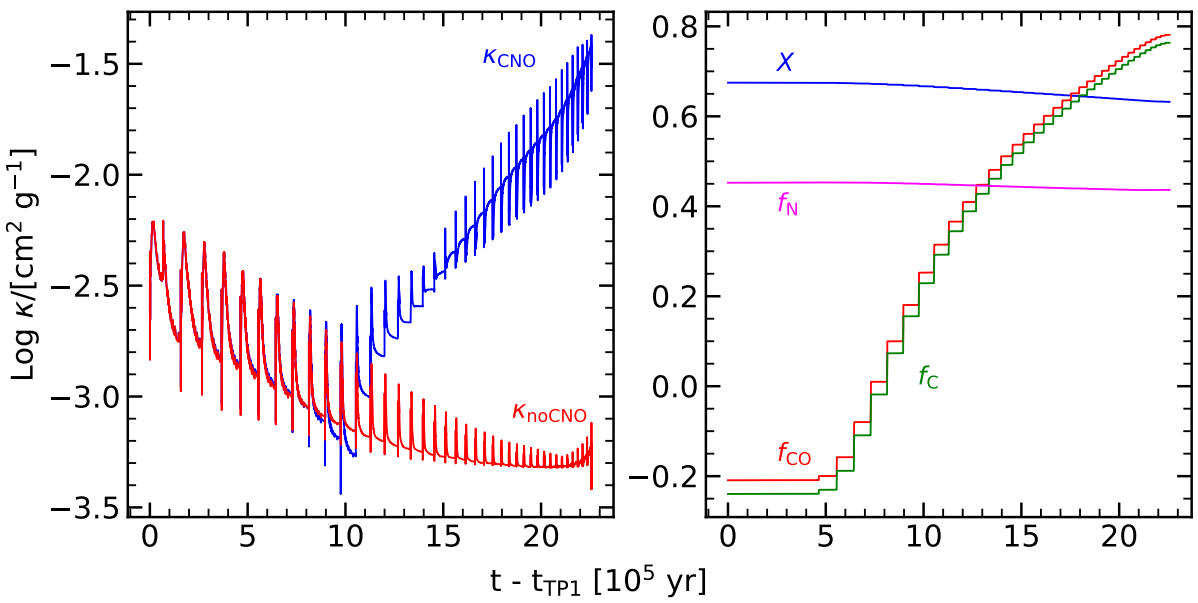

Fig. 3.1: Evolution of the two types of opacity tables (left panel) and the four abundance variables (right panel) for a TP-AGB track with $M_{\rm ini} = 2.5$ M$_\odot$ and solar metallicity $Z = 0.014$, specifically on the surface. The x-axis is the age from the first thermal pulse, in units of 10^5 yr.

and this results in $4 \times 11 \times 11 \times 5 = 2420$ tables per value of metallicity. Each opacity table, regardless of the type, runs over two variables, temperature T and R (not to be confused with the total radius, only here), defined as:

$$R = \frac{\rho}{(T/10^6\ \mathrm{K})} \tag{3.4}$$

The tables are read at the beginning of the code and stored for the whole evolution, so that there is little time spent in reading the tables, but the interpolation technique inside the opacity module has to be optimized not to increase considerably the computational time. Being the nodes sufficiently fine, I chose to interpolate linearly over each of the six variables at play (R, T, X, $f_{\rm CO}$, $f_{\rm C}$, $f_{\rm N}$), and the approach is simple enough to incorporate over a single[1] line of code that avoids excessive use of cycles to estimate the opacity. Once the routine has been updated to track and interpolate over all the new nodes, we can quantify the difference in using the classical opacity tables ($\kappa_{\rm noCNO}$) and the new ones ($\kappa_{\rm CNO}$). To do so, I calculated a TP-AGB evolution for a $M_{\rm ini} = 2.5$ M$_\odot$ and solar metallicity $Z = 0.014$ that considerably increases the C/O over unity with the classical opacity tables, without the additional nodes. Then, we can take the evolution of the six variables (R, T, X, $f_{\rm CO}$, $f_{\rm C}$, $f_{\rm N}$) on the surface and calculate the surface opacity that would result by using the new tables. I plot the result in Figure 3.1. The comparison between the two opacity tables clearly shows that as long as the composition stays oxygen-rich there is almost no difference. However, when $f_{\rm CO} \gtrsim 0.2$ (C/O = 1 corresponds to $f_{\rm CO} \simeq 0.26$) the two tables begin to return different results, and the discrepancy increases up to three orders of magnitude as the carbon abundance increases. This test was done on the same

[1] Extremely long.

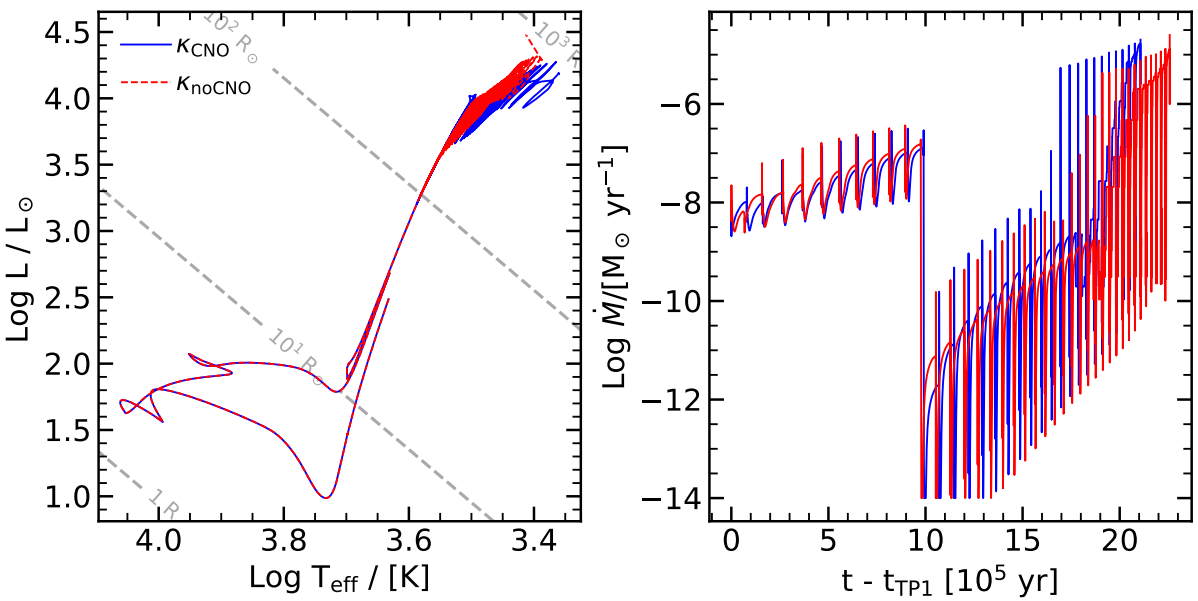

Fig. 3.2: H-R diagram (left panel) and mass-loss evolution (right panel) of a 2.5 $M_\odot$ track from PMS to the TP-AGB with classic (blue line) and new opacity tables (red line). In the left panel, the age is shown from the first thermal pulse of each track.

track and the κ_{CNO} was calculated a posteriori, but if the track is calculated with the proper opacity tables the discrepancy will directly affect the evolution. This is what has been done in Figure 3.2 and Figure 3.3. From the H-R diagram we can see that the evolution is exactly the same up to the TP-AGB, even though abundances are already modified by the FDU. However, the variation induced by FDU is not sufficient to produce a sensible effect on the opacity. TDU

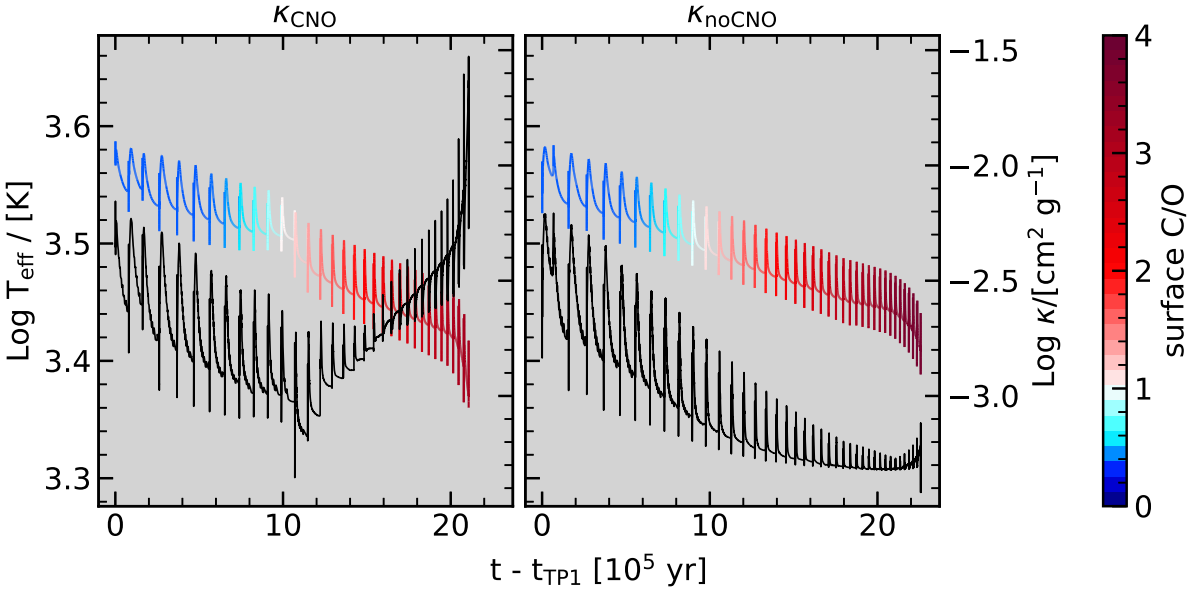

Fig. 3.3: Effective temperature evolution (color-coded with the surface C/O, left axis) and surface opacity (black line, right axis) from the first thermal pulse of a 2.5 $M_\odot$ track for new (left panel) and classic (right panel) opacity tables.

is much more impactful in this sense, as the (mainly) carbon enrichment and the consequence opacity effect drives the evolution towards cooler temperatures, affecting the dust production and the magnitude of the mass loss, which is generally larger. That allows the track to reach the carbon-dust-driven regime earlier than using classical opacity tables, which ultimately affects the lifetime (and the final core mass) of the star. A more detailed look on the effective temperature is given in Figure 3.3. As anticipated, the turning point is where C/O $\simeq$ 1, and after that the track with $\kappa_{\rm CNO}$ cools down sensibly faster than the classical one due to the sudden increase in opacity.

3.2 Revisiting the shell-shifting

3.2.1 Back to the drawing board: energy conservation in TP-AGB

A TP-AGB star is powered, for most of the time, by the hydrogen shell underneath the convective envelope, if HBB is not present. For the sake of simplicity, I focus on those stars without HBB, but I will discuss this particular scenario later in this section. The hydrogen-burning shell is thin, as shown in Figure 1.6 and Figure 1.7, and the ashes are deposited on top of the He-core, making it grow and moving the burning front outwards. The H-shell also moves outwards because part of the energy produced by the reactions warms up the layers surrounding the shell, triggering hydrogen burning where it is not depleted and pushing the border of the convective envelope outwards. The H-shell evolution during an interpulse is shown in Figure 3.4, together with temperature and density profiles. Energy conservation between age t_1 and t_2 reads:

$$E_1 = \int_{t_1}^{t_2} \mathrm{d}t L_{\rm H} = \int_0^M \mathrm{d}m \left(X_{\rm H}(m, t_1) - X_{\rm H}(m, t_2)\right) q_{\rm val} = E_2 \tag{3.5}$$

In the full regime of the interpulse phase, there is little to no variation of the luminosity and it comes almost entirely from the hydrogen burning, therefore we can simplify the equation to:

$$L\Delta t \simeq q_{\rm val}\Delta M_{\rm H} \tag{3.6}$$

This form of energy conservation shows very clearly that, during the interpulse, the timescale is given by the movement of the hydrogen-burning shell. Furthermore, we can use it to check if the code conserves the energy model after model because Eq. 2.4 only ensures that it is locally conserved inside the structure at a fixed time. In Figure 3.5 we compare three TP-AGB tracks with different time constant $f_{\rm T}$, which simply allows for bigger timesteps at increasing values. As explained in Section 2.2.3, PARSEC has multiple time constants that can be set, and I selected the dominant one in the interpulse phase for the discussion. We can see that the two expressions for computing the energy generated by the hydrogen shell do not agree, they differ up to 50% when using the largest $f_{\rm T}$. For $f_{\rm T} = 0.1$ the difference is limited to a threshold under which we cannot disentangle physical inconsistencies or numerical artifacts. However, the $\Delta E/E$ value offers a much deeper interpretation. If it is positive and much larger than zero, it means that the hydrogen shell has not moved outwards by the correct amount in mass coordinate to explain

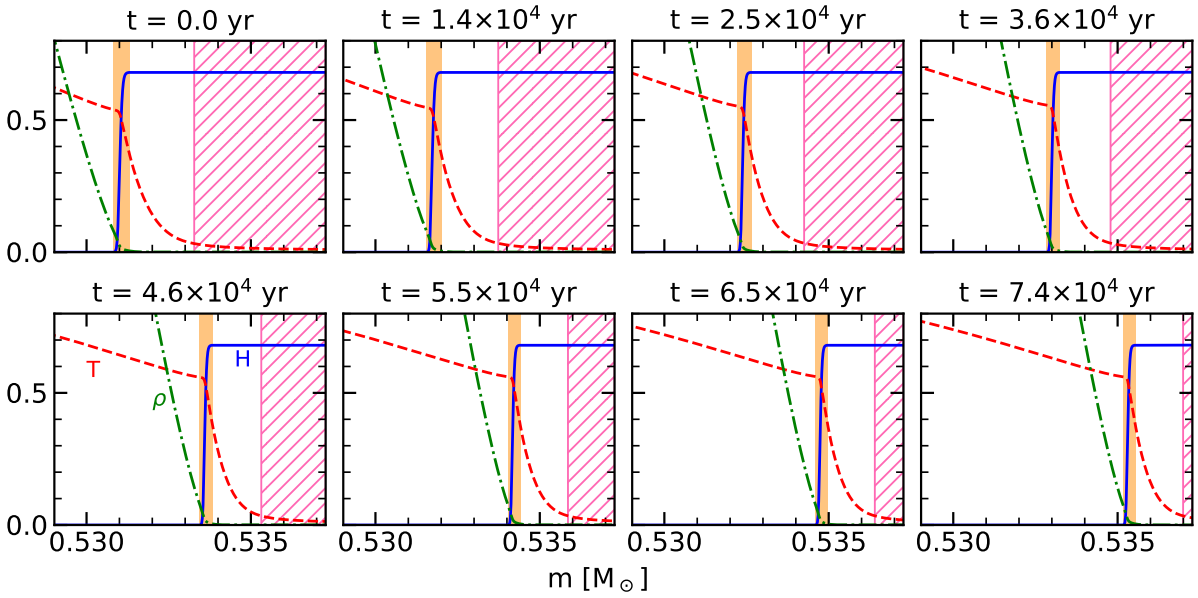

Fig. 3.4: Hydrogen shell evolution inside the structure of a $2M_{\odot}$ track during the interpulse, after the 10th thermal pulse. The orange-shaded area marks the region where hydrogen is burnt. The pink hatch marks the convective envelope. The blue solid line shows the hydrogen mass fraction, the dotted red line represents the temperature profile in units of 10^8 K, and the green dotted line is the density in units of 10^3 g cm^{-3}. The windows show the structure of the track every 500 models, we report the time after the first one.

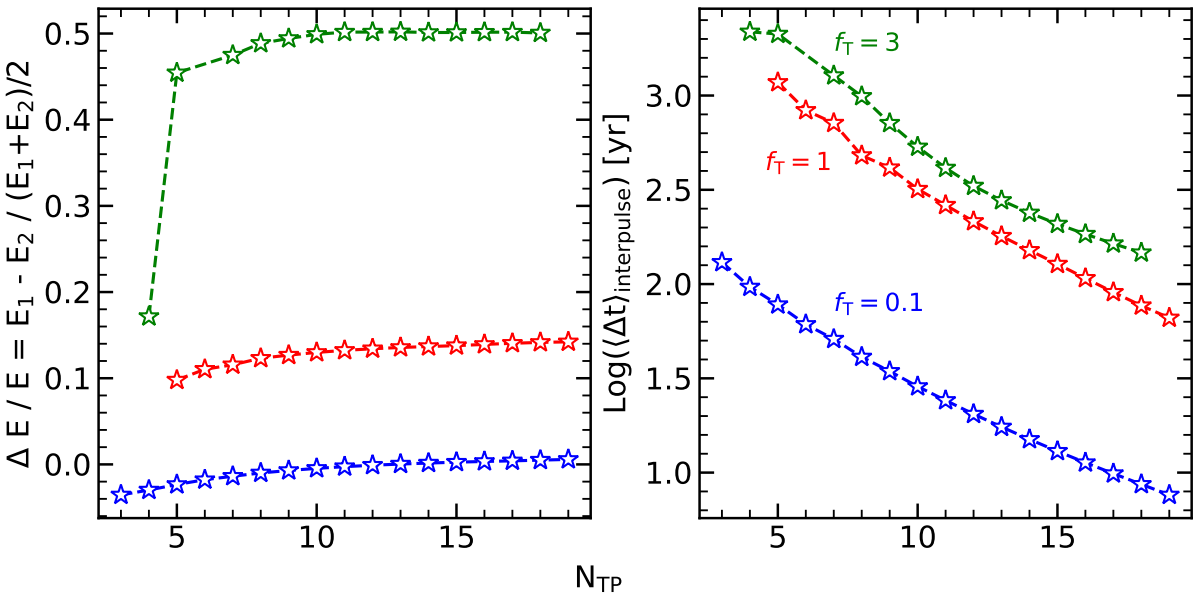

Fig. 3.5: Energy conservation checks for three TP-AGB tracks with $M_{\rm ini} = 2M_{\odot}$ and different values for the dominant time constant. Each symbol refers to the whole interpulse between pulses $N_{\rm TP}$ and $N_{\rm TP}+1$. The left panel shows the fractional difference of the energy generated by hydrogen burning computed as in Eq. 3.5. The right panel shows the average timestep in the interpulse corresponding to the different time constant $f_{\rm T}$.

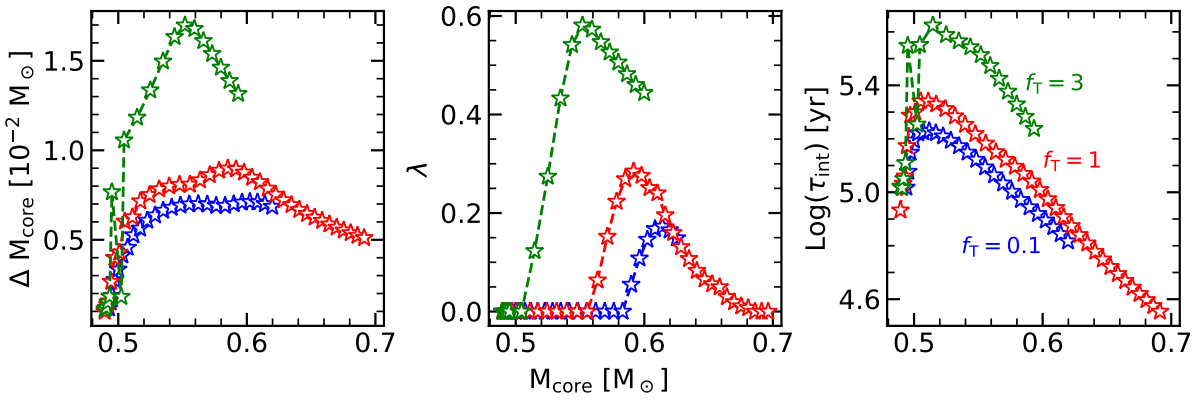

Fig. 3.6: Core growth (left panel), TDU efficiency (central panel) and interpulse duration $\tau_{\rm int}$ (left panel) for three TP-AGB tracks with $M_{\rm ini} = 2{\rm M}_{\odot}$, with the same time constants as in Figure 3.5. The core mass is taken at the maximum of the quiescent luminosity, before the thermal pulse.

the hydrogen luminosity of the model. In other words, the time that has really passed between the two models should be smaller than what has been assigned, which is equivalent to say that the hydrogen shell is the real clock of the star during the interpulse. The time mismatch has severe implications both on the structure and chemical evolution, some of which are shown in Figure 3.6. Even though the three tracks have all the same parameters but $f_{\rm T}$, they act like three different tracks. The core mass, which is the main parameter of the TP-AGB evolution, evolves completely differently in the three timestep cases. During each interpulse, the core grows more at increasing $f_{\rm T}$, for which models suggest more powerful thermal pulses (Marigo et al., 2013) and therefore more efficient TDUs. Furthermore, not following the real clock of the star gives different timescales for the interpulse period, increasing when the timestep is larger. At this point, I investigate whether these discrepancies have only a numerical nature or if I can extract useful information even from the tracks that do not conserve energy (in time!).

To answer this question, I restarted the evolution of the 2 $M_{\odot}$ track with $f_{\rm T} = 3$ after the 10th thermal pulse, changing the value of $f_{\rm T}$ to 0.1 and 1, and I compared the evolution only in the following interpulse period, stopping when the 11th thermal pulse is triggered. In Figure 3.7, I show the maximum temperature $T_{\rm max}$ in the intershell and the gravitational luminosity $L_{\rm grav}$, which has been calculated by integrating $\varepsilon_{\rm grav}$ only in the intershell. The gravitational energy rate $\varepsilon_{\rm grav}$ is crucial because it is the only place, in the structure equations, where the timestep appears directly (Eq. 2.4). Without that term, the structure equations would sense the time flowing only through the chemical profile changes. Figure 3.7 clearly demonstrates that the intershell is hotter at decreasing $f_{\rm T}$, which is caused by a higher degree of contraction, as shown by the larger (and positive) gravitational luminosity. Being hotter, the intershell has to accumulate less material from the hydrogen shell to trigger a thermal pulse again, which explains the trends in the leftmost panel of Figure 3.6, and ultimately the whole picture. Ideally, we would like $\varepsilon_{\rm grav} = {\rm d}S/{\rm d}t$ to be independent of the time constant, and therefore to the choice of the timestep, but the code does not find an entropy variation that scales as the dt. To summarize the whole discussion, at decreasing $f_{\rm T}$ the intershell contracts more and stays hotter (larger $L_{\rm grav}$),

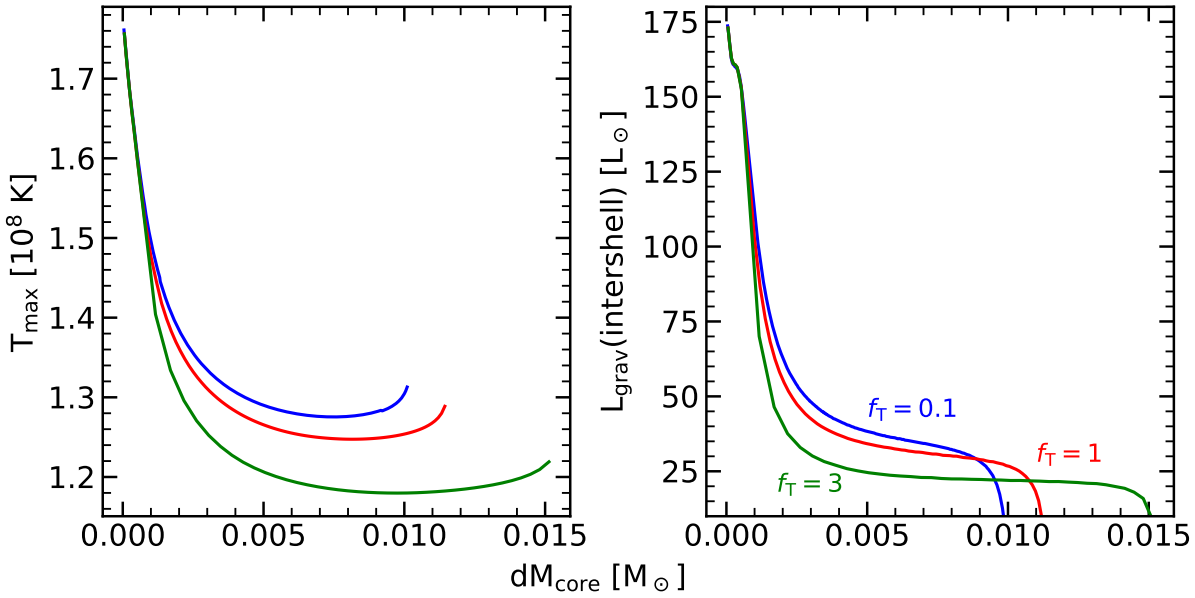

Fig. 3.7: Maximum temperature in the intershell (left panel) and gravitational luminosity evolution (right panel) during the 10th interpulse of a 2 $M_\odot$ track. During the interpulse, the time passed can be tracked by the relative growth of the core, dM_{core}. The track has evolved to the starting point with $f_T = 3$, which then has been changed after the 10th thermal pulse (when PDCZ has vanished). The evolution is stopped when the 11th thermal pulse is triggered.

which limits the core growth during the intershell (and its duration), prompting less powerful thermal pulses and, ultimately, less effective dredge-ups. These discrepancies accumulate every pulse cycle, causing the track to follow different evolutionary paths (and reach different final outcomes) depending only on the value f_T.

I interpreted the outcome of the tracks on the physical ground, but now we have to answer why, from the numerical point of view, the code is not able to keep up dS consistent with the choice of f_T. Actually, this has been already hinted at the beginning of this long (and deep) analysis and it is related with the non-simultaneous nature of `PARSEC`. I recall that (see flowchart in Figure 2.2) non-simultaneous stellar evolutionary codes solve the structure and chemical equations separately. Therefore, when the chemical routine is called the structure is kept constant, which is equivalent to say that in the given timestep Δt the structure does not evolve significantly. When a thin burning shell is present (hydrogen shell in our case), this assumption easily breaks down because of the strong dependence of the nuclear reaction rates on temperature, which varies rapidly with the mass coordinate (Figure 3.4). If the timestep given to the chemical solver is too large the thin shell gradually reaches layers where the temperature is not high enough to burn the particular material at the same rate, or even burn at all, stopping the growth of the underlying core. This is exactly what I observed in the right panel of Figure 3.5, where the energy computed with the luminosity integral does not match the same energy calculated with the progression of the hydrogen profile.

3.2.2 A newer shell-shifting method

In the previous section, I deeply investigated the status of energy conservation (in time) in TP-AGB models and the sources of inconsistencies and time mismatches. We are now left with only two options: the first one is to set a small $f_{\rm T}$, increasing the already high computational cost of such tracks; the second is to develop a method to use larger timesteps still conserving the energy model after model. The said method could simply be changing completely how PARSEC solves the equations, from a non-simultaneous to a simultaneous approach. Stancliffe (2006) already studied the differences in the two methods in the TP-AGB phase, finding that to find equivalent results the timestep has to be considerably smaller for the non-simultaneous case. However, this would mean a complete re-writing of the code and consequently testing and calibrating again everything. Instead, literature already provides part of the solution. Weigert (1966) (or better[2] Kippenhahn et al. (1967)) already approached the problem of thin burning shells to reduce the computational cost, and at that time the choice was forced because computers were extremely slow, compared to what we have today. However, sometimes (almost always) it is very instructive to look back and re-interpret what has already been done. Weigert (1966) overcame the problem of using small timesteps by rigidly shifting the shell to enforce energy conservation, by letting the code approach the hydrogen profile found by differentiating Eq. 3.5.

In PARSEC, I implemented a shell shift-like routine to be used only during interpulses of the TP-AGB phase that is called inside the chemical solver. I recall that (Figure 2.2) the chemistry solver is called right after the calculation of the timestep for the next model and its goal is to find the next solution for the abundance profiles, for which it needs temperature, density, radius, diffusion coefficient, and reaction rate profiles. At the beginning of the chemistry solver, the timestep Δt is split into N equal sub-steps. At each sub-step, the solver is called and finds the solution for the abundance profile, which is used in the next sub-step while still keeping all the structure profiles constant. The idea is to shift outwards all the profiles used in the chemistry by a mass $\Delta M = \Delta M_{\rm H}$ equal to the mass of burn hydrogen at the end of each sub-step. The shifted structure represents an approximation of the real structure if we looped over the whole flow of the code with a timestep $\Delta t' = \Delta t / N$ equal to the duration of the sub-step. The implementation and workflow of the new module are shown visually in Figure 3.8, but we now explain the steps in detail.

First, I need a practical and reliable way to determine if the track is in the interpulse phase, where the star is fully sustained by the hydrogen shell. Therefore, I define the star to be in the interpulse if the ratio:

$$\frac{L_{\rm H}}{L_{\rm H} + L_{\rm He}} \geq \text{threshold} \tag{3.7}$$

The threshold can be arbitrarily varied, but I found that it should be at least 0.9, meaning that at least 90% of the luminosity produced by nuclear reactions is generated by hydrogen burning. When the criterion is not satisfied, the track goes under the normal workflow of the code, using very restrictive time constants, to ensure that energy is conserved and avoiding the problem I

[2] Only because I was not brave enough to learn German.

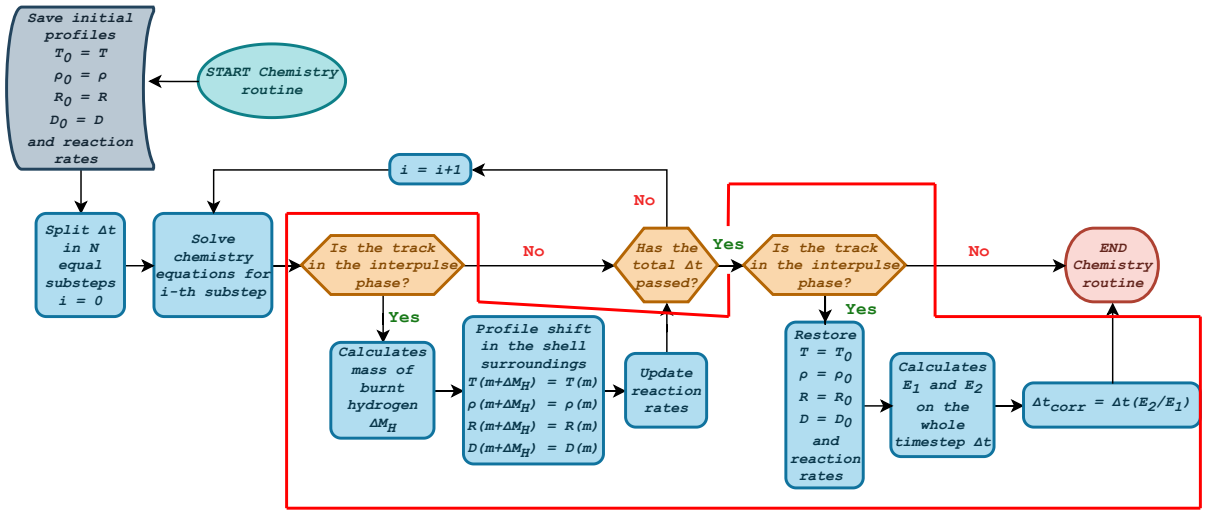

Fig. 3.8: Flowchart of the shell shifting routine implemented in PARSEC. The red closed area groups the steps activated only for the shell shifting. Details are discussed in the text.

discussed in the previous section. Otherwise, the track can safely proceed through the shell-shifting routine, and the limits on the timestep are gradually relaxed. Once the timestep Δt is chosen, the code calls the chemistry routine and saves the initial stage, before preparing to loop through the sub-steps of width $\Delta t/N$. At any given sub-step, the code first solves the chemistry equations (Eqs. 2.10) and checks again if it can use the shell shift. If the check is positive, it brackets the burning region only considering the radiative layers. The radiative condition is critical because convective motions can quickly mix the ashes, which cannot accumulate behind the burning front, effectively pushing it outwards. Now, the routine can calculate the mass of burnt hydrogen by integrating the difference between the old and new hydrogen mass fraction in mass:

$$\Delta M_{\rm H} = \int_{m_{\rm b1}}^{m_{\rm b2}} {\rm d}m \, (X_{\rm H}(m, t_{\rm i-1}) - X_{\rm H}(m, t_{\rm i})) \tag{3.8}$$

where i indicates the i-th sub-step, and $m_{\rm b1}$ and $m_{\rm b2}$ are the borders of the radiative burning region. In practice $m_{\rm b1}$ is the border of the hydrogen-depleted core, and $m_{\rm b2}$ is the bottom of the convective envelope. In other words, I established how much the hydrogen profile has shifted outwards, leaving a mass $\Delta M_{\rm H}$ of ashes. Therefore, I predict the structure for the next sub-step to be:

$$T^{i+1}(m + \Delta M_{\rm H}) = T^{i}(m) \tag{3.9}$$

and similarly for density, radius, and diffusion coefficient. The shift is done only for $m \geq m_{b1}$, which may leave a gap if the $\Delta M_{\rm H}$ is bigger than the distance between two adjacent meshpoints. The routine fills the gap with linear interpolation, which avoids abrupt changes in the structure profiles and does not increase the temperature significantly in the underlying He-core, with the risk of an early occurrence of the thermal pulse. I remark again that these shifted profiles must be interpreted as approximations of the solution the structure solver module would give if used with the same timestep $\Delta t/N$. In Figure 3.9 I show the discrepancy caused by using no shell-shifting module with a (too long) timestep, during a single sub-step of the chemistry routine. If no shift

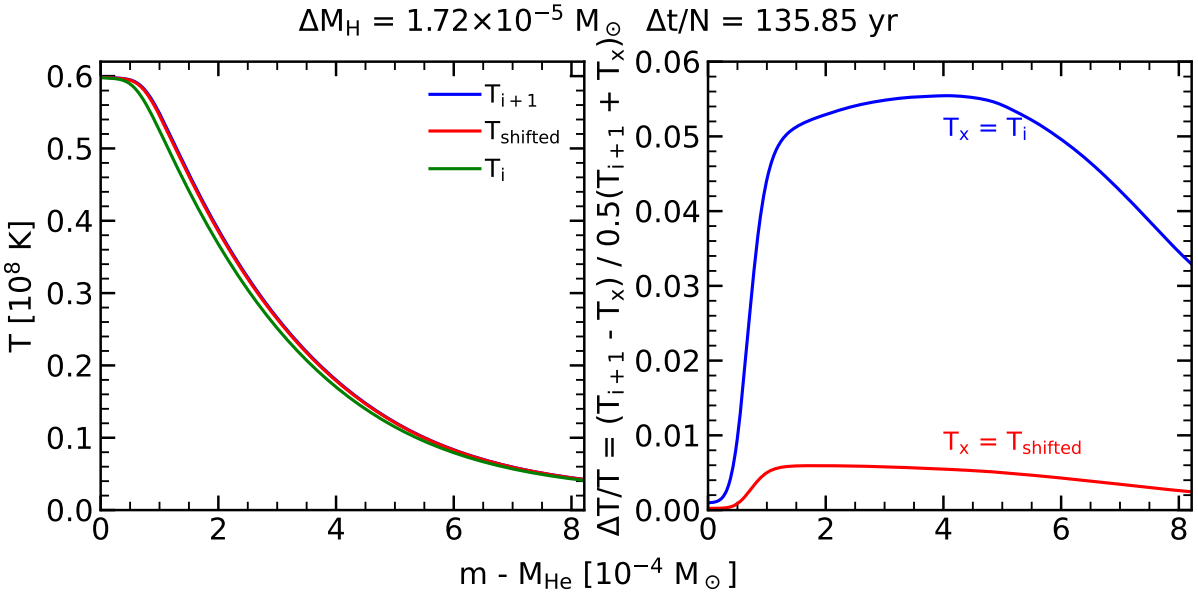

Fig. 3.9: Temperature profile shift during one chemistry sub-step, with a (sub)timestep $\Delta t/N \simeq 135$ yr. The timestep length has been chosen to allow visual comparison between the curves. The left panel shows the temperature profiles, where $T_{\rm i}$ (green line) is the profile at the beginning of the sub-step and it stays constant for all the sub-steps (from $i = 0$ to $i = N - 1$) if no shift is applied. $T_{\rm i+1}$ (blue line, below the red line) is the profile obtained using the whole PARSEC workflow with a (full) timestep of $\simeq 135$ yr. $T_{\rm shifted}$ (red line) is the profile obtained by shifting $T_{\rm i}$ by the mass of burnt hydrogen in the i-th sub-step. In the right panel, we plot the fractional difference between $T_{\rm i+1}$ and the other two profiles. The x-axis shows the range for the shell-shifting procedure, going from the hydrogen-depleted core's border to the convective envelope's bottom.

is applied, the error made by maintaining a constant temperature profile on the single sub-step seems limited to less than 6%. However, this accumulates over every iteration of the chemistry solver, producing, in the end, the differences in the left panel of Figure 3.5. Moreover, Figure 3.9 also demonstrates the power of the shell-shifting module, which can reduce the discrepancy to less than 1% on a relatively long duration sub-step, and similar results are obtained for all the profiles used by the abundance equations. Once the profiles have been shifted, the reaction rates are updated and the code proceeds to the next sub-step. At the end of the chemistry iterations, the module checks again for interpulse, and it restores the real initial structure profiles that are used as initial guesses for the next model structure (Figure 2.2). If the shell-shifting routine has been used, it checks the mass variation of the hydrogen shell over the whole timestep, and it (usually) still finds residual differences between E_1 and E_2 (Eq. 3.5). Therefore, I use the physical intuition I discussed before (e.g. the hydrogen shell sets the timescale in this phase), and I correct the timestep for the needed factor to synchronize the structure and chemical changes, which closes out the full chemical routine with the shell-shifting module. The correction factor is defined as follows:

$$\Delta t_{\rm corr} = \Delta t \frac{E_2}{E_1} \tag{3.10}$$

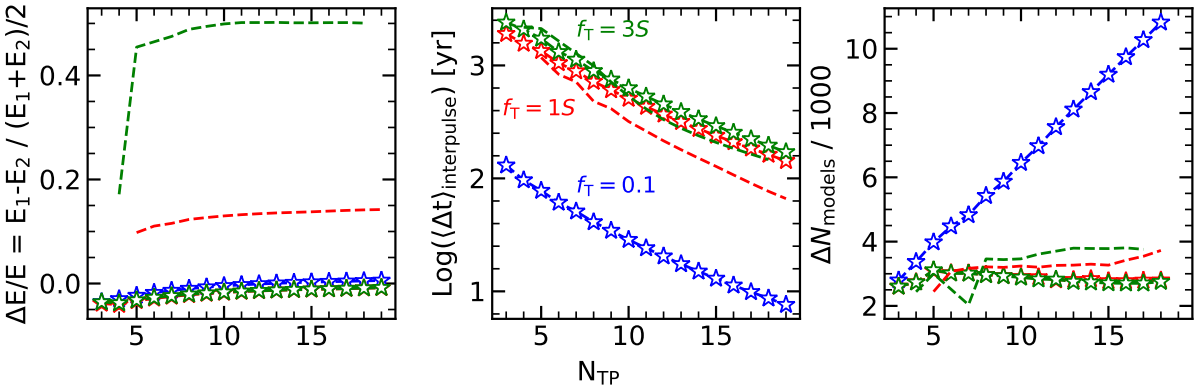

Fig. 3.10: Energy conservation checks for three TP-AGB tracks with $M_{\rm ini}$ = 2M$_\odot$ and different values for the dominant time constant, activating the shell shifting module. Each symbol refers to the whole interpulse between pulses $N_{\rm TP}$ and $N_{\rm TP}$ + 1. The left panel shows the fractional difference of the energy generated by hydrogen burning computed as in Eq. 3.5. The central panel shows the average timestep in the interpulse corresponding to the different time constant $f_{\rm T}$. The right panel shows the number of models between two consecutive thermal pulses in units of thousands. The dashed lines with no symbols are the $f_{\rm T}$ = 1 and 3 curves with no shell shifting, the same as Figure 3.5.

I can compare the before and after the shell-shifting module intervention, again checking the fractional energy difference over the interpulses phases in Figure 3.10. Using the shell-shifting method I can reach a comparable accuracy as setting $f_{\rm T}$ = 0.1, which would require an increasing number of models per pulse cycle. We see that the shell-shifting tracks can keep down the number of models per pulse cycle at about $\sim$ 3000, which however are now mostly distributed outside the interpulse phase where the shell-shifting routine is not called. The computational cost is significantly reduced by a factor of $\sim 3-4$ allowing the exploration of much larger grids of parameters. The actual CPU time depends on the specific machine and the number of jobs present at the execution, but our tests on a single core of the Intel Xeon Gold 6238R CPU @ 2.20GHz take about $\sim$ 400 hours for a 2 M$_\odot$ track without shell-shifting, reduced to about $\sim 70-80$ hours if the shifting is used. Finally, I can compare the whole evolution of the tracks with shell-shifting with our prototype $f_{\rm T}$ = 0.1 track. Figure 3.11 shows that the critical physical quantities for the evolution are in good agreement, even the TDU efficiency, which is notoriously sensible on the numerical treatments, is superimposed with the prototype at $f_{\rm T}$ = 0.1.

I (intentionally) left out the discussion of HBB. It is now time to address the elephant in the room, is the shell-shifting valid even when most of the burning occurs inside the convective envelope? My assumption on the Eq. 3.8 was to consider only radiative layers because burning in convective conditions does not produce a shift in mass of the abundance and structure profiles. Therefore, the picture is more complicated when the H-shell partially or completely overlaps with the convective envelope. When a strong HBB is present, the core mass is practically set at the beginning of the TP-AGB, because either the TDU efficiency is $\simeq$ 1 and nullifies the core growth during the interpulse or because there is little to no core growth at all and the TDU is not present anymore. However, the timestep has to be limited to accurately model the complicated

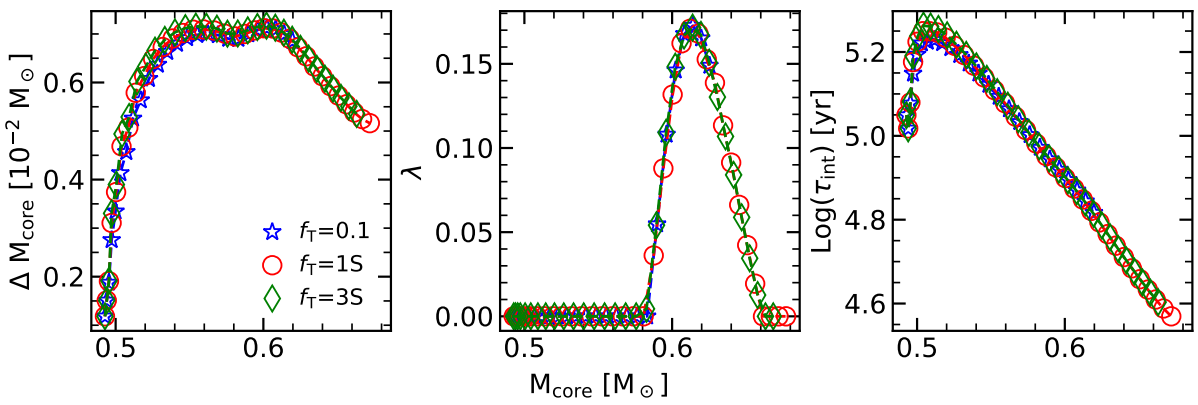

Fig. 3.11: Core growth (left panel), TDU efficiency (central panel) and interpulse time (right panel) for three TP-AGB tracks with $M_{\rm ini} = 2M_{\odot}$ and shell-shifting. The core mass is taken at the maximum of the quiescent luminosity, before the thermal pulse.

nucleosynthesis occurring inside the convective envelope, which continuously affects the surface abundances instead of affecting it in episodes as the TDU does. Up to now, I tried a few solutions to accelerate the evolution even in HBB cases but with little success. Therefore, for the current PARSEC version, I shut off the shell-shifting module if a strong HBB is detected.

3.3 Ending TP-AGB tracks

3.3.1 Overview on the problem

As stars approach the end of the TP-AGB phase, they are characterized by high luminosity ($\mathrm{Log}\, L/L_{\odot} \gtrsim 4.2 - 4.4$, depending on the initial mass) and low effective temperature ($\mathrm{Log}\, T_{\rm eff} \lesssim 3.40$). In these advanced phases, issues in finding model convergence arise and it becomes difficult to follow the evolution with PARSEC. This region of the HR diagram is notorious for numerical difficulties (Wood & Faulkner, 1986; Wagenhuber & Weiss, 1994; Herwig, 1999; Karakas, 2003; Miller Bertolami & Althaus, 2006; Karakas & Lattanzio, 2007; Weiss & Ferguson, 2009; Lau et al., 2012; Miller Bertolami, 2016). These numerical difficulties appear to be independent of the specific stellar evolution code, computational grid, and time step employed (see also discussion by Addari 2020). I tried to determine with our present tracks whether this challenge stems from purely numerical complications or originates from a more physically motivated ground; I have not found conclusive information yet, but literature and our tests suggest that the track can reach the end of the TP-AGB if they avoid the region of the H-R diagram mentioned above. For instance, I calculated a few stellar tracks with a very high mass-loss, which have a relatively short TP-AGB phase, and these examples reached the post-AGB without user assistance. Furthermore, Lau et al. (2012, and references therein) found out that increasing the mixing length parameter, when restarting a track that failed to converge, can delay or avoid the instability. Increasing α causes a significant increase in effective temperature, again pointing towards identifying such region as the source of the problem.

Even though a good meshing scheme might delay the divergence, there is no reliable method to end TP-AGB tracks if they become too cool and luminous. Wagenhuber & Weiss (1994) and Miller Bertolami (2016) discussed the possibility of the connection with a real physical phenomenon, hydrogen recombination. After a thermal pulse, the envelope suffers a significant expansion, quickly cooling down and preparing suitable conditions for rapid recombination of hydrogen (and secondarily, helium He^+). If the recombination takes place where the code solves the full set of equations, it may quickly develop a dynamical instability. Wagenhuber & Weiss (1994) tried to implement the acceleration term to the momentum equation (Eq. 2.3) but with no success in overcoming the instability. It is possible to deal with this instability by including the hydrogen recombination layers in the outer integration, where the luminosity is assumed constant and no energy source or sink is described. While this clearly eliminates the sudden energy injection by the recombination, it is still debated if this is physical and leads to episodes of strong mass loss or even the ejection of the envelope.

3.3.2 Synthetic AGB evolution and the COLIBRI code

At this point, I have made it very clear that full evolutionary calculations of the TP-AGB phase come at a high computational cost, and ejecting the envelope with proper wind recipes brings the track in regions of the H-R diagram where full codes either need a lot of user assistance or fail to converge at all. For these two reasons, synthetic AGB models were widely popular in the literature (Groenewegen & de Jong, 1993; Wagenhuber & Groenewegen, 1998; Izzard et al., 2004). These models start from the first thermal pulse of full evolutionary calculation, and they replace the complicated physics processes with analytical expressions. Clearly, these analytical approximations need to be carefully calibrated on the available full evolutionary calculations but, once this is done, they allow to explore the large parameter space of TP-AGB models with little computational cost. This agility, however, is paid with the loss of accuracy compared with full tracks and the risk of extrapolations outside the intended range of validity of such methods. Their range of validity is usually quite narrow and in any case limited to oxygen-rich stars, therefore still far from the cool temperature typical of carbon stars.

A more intriguing possibility is given by the class of *hybrid models* or, more appropriately, *envelope-based models*, where a mix of full evolution and synthetic techniques are used. The COLIBRI code (Marigo et al., 2013) may fall in this category, however, it leaves out much of the analytic formalism in favor of a detailed physics of a complete envelope model, for which a more fitting name would be *almost-full* TP-AGB model. Despite still requiring full models as a reference for accuracy and some fitting relations (for instance, the evolution of the intershell composition during the thermal pulses), COLIBRI integrates the four stellar structure equations from the atmosphere to the bottom of the convective envelope, and it shares several modules and routines with PARSEC, e.g. convection, atmosphere, opacities, nuclear reactions, mass loss and the diffusive scheme of convection in the envelope. Furthermore, it uses the ÆSOUPUS code on the fly for opacities and equation of state, without resorting to the interpolation pre-computed tables, and it naturally accounts for HBB nucleosynthesis. The TDU efficiency is parameterized, but

Marigo (2022) recently introduced a more physically sound description where it is determined by the core and envelope mass. More details on the interaction between PARSEC and COLIBRI are given in Section 4.4.

3.3.3 A brand new extrapolation scheme

In this section, I present a solution for completing TP-AGB tracks in a self-consistent way, meaning that we use all the information currently available for each single track computed with PARSEC, and extrapolate it to the end of the TP-AGB phase. That is meant to apply if the main goal is to predict the final mass of the white dwarf left as a remnant[3]. If so, it is possible to extrapolate and get a first-order approximation for $M_{\rm f}$. I worked out a solution that resembles closely the workflow of the COLIBRI code (Marigo et al., 2013), even though it gives up much of its complexity to get a simple, yet effective, estimate of the final mass. I will call it from now on as *extrapolation scheme*[4], and I explain how it works in the following. Let me start by showing its flowchart, since by now we got used to them, in Figure 3.12. The extrapolation scheme is applied to a given TP-AGB track that was not able to reach the end, which is assumed when:

$$M_{\rm env} < 0.01 {\rm M}_{\odot} \tag{3.11}$$

If this is the case, the extrapolation begins, aiming to peel down the envelope to reach the condition above. The main idea is to exploit the hard dependence upon the core mass $M_{\rm core}$ during the interpulses of the remaining pulse cycles. Therefore the first step is to find fitting functions for quantities needed to calculate the stellar wind (luminosity and effective temperature) and the interpulse phase variable, defined as:

$$\varphi = \frac{t - t_0}{\tau_{\rm int}\left(M_{\rm core}\right)} \tag{3.12}$$

where t_0 is the age at the beginning of the interpulse phase, meaning that $\varphi = 0$ when the interpulse starts and $\varphi = 1$ when it ends. After the first few thermal pulses, the interpulse lifetime obeys a tight power law relation, which is easily found by fitting the previous PARSEC TP-AGB track (e.g. leftmost panel in Figure 3.11). To extrapolate the luminosity and effective temperature, I split the problem into two parts, which I call *fitting functions* and *shaping functions*.

The fitting functions are those defining the limits of variation of $T_{\rm eff}$ and Log L inside each interpulse against the core mass at the quiescent maximum luminosity (the maximum core mass reached). Therefore, there is a data point for each interpulse. The limits are defined by two values: the minimum $T_{\rm eff}$ (or Log L) and the range over which it distributes in each interpulse $\Delta T_{\rm eff}$ (or Log L). Another choice would be the minimum and maximum of the said quantities, but I found that taking the minimum and the Δ was more stable when trying to find a linear fit. In Figure 3.13 I show the resulting fitting functions for a case with $M_{\rm ini} = 2M_{\odot}$. Since the

[3] Conveniently that was the objective of the paper, see Chapter 4.

[4] Waiting for a fitting acronym to be remembered by future generations.

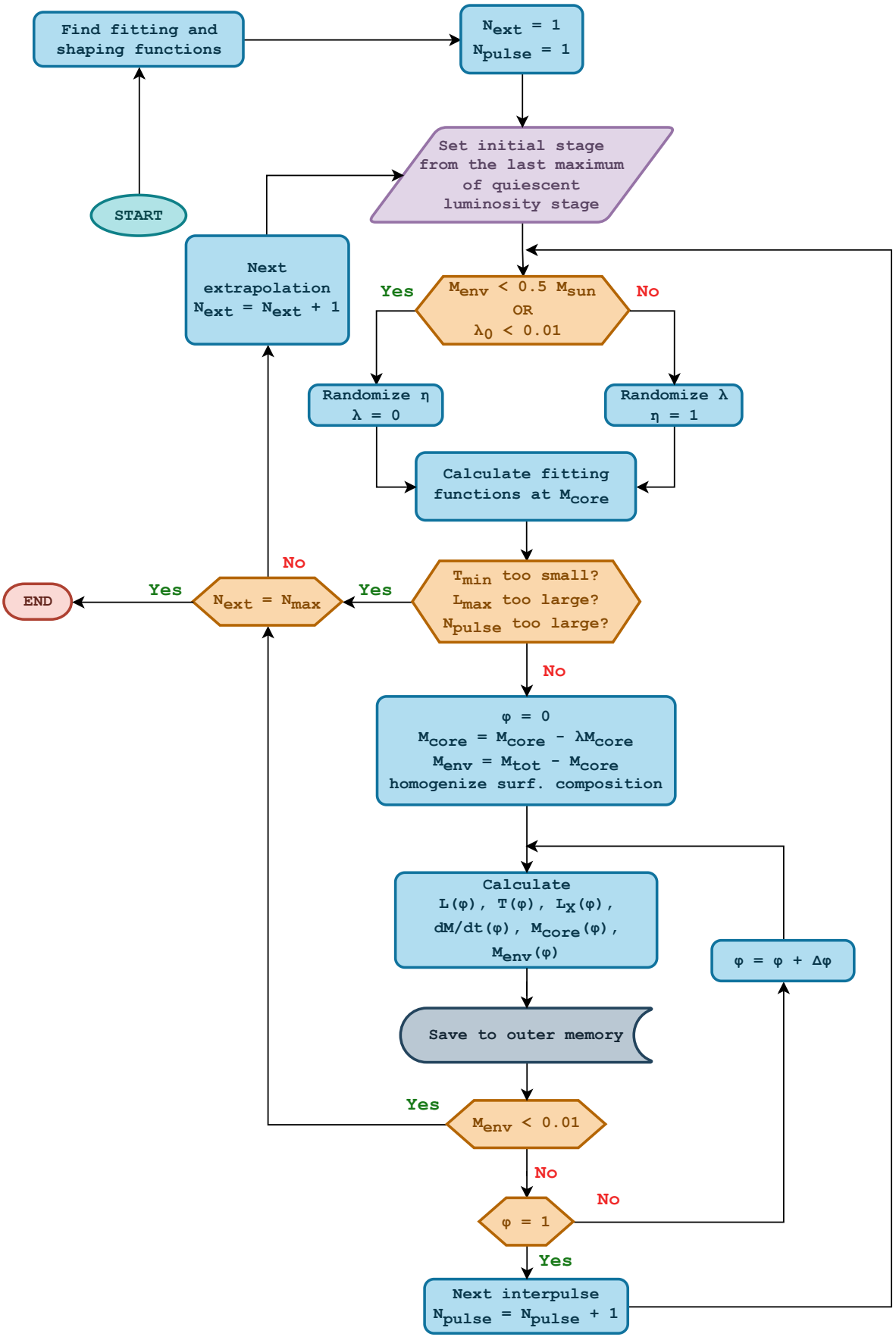

Fig. 3.12: Flowchart of the extrapolation scheme.

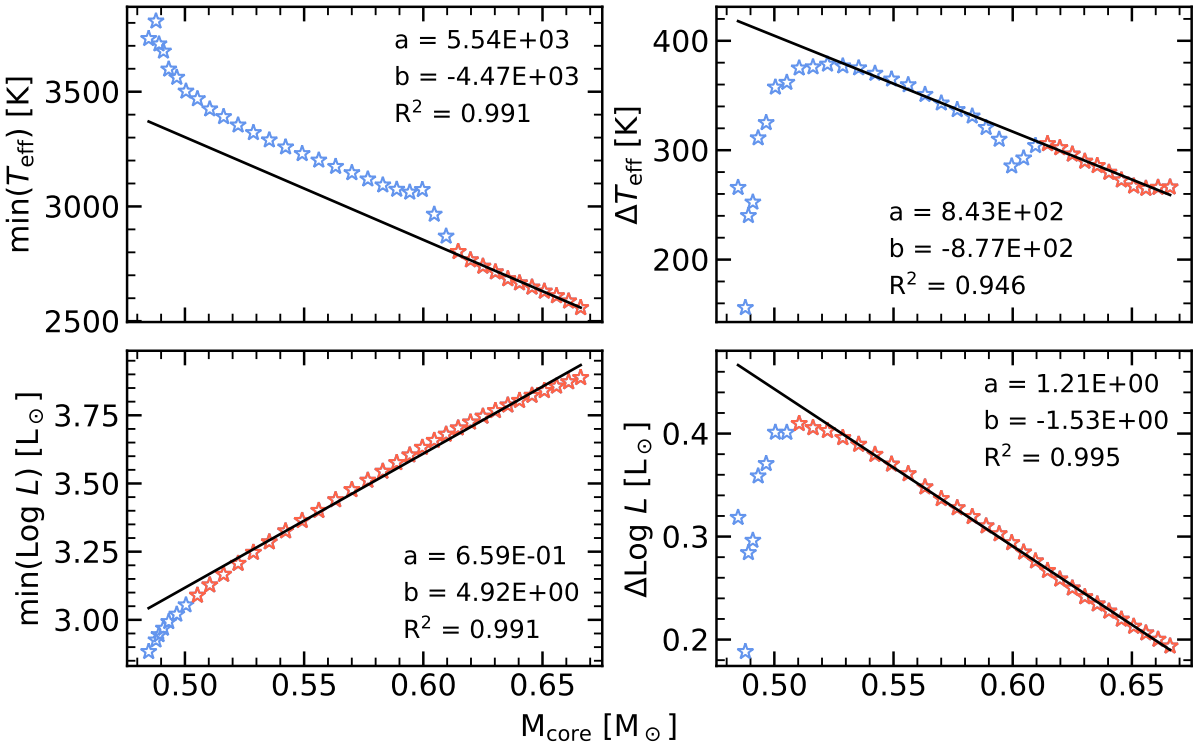

Fig. 3.13: Fitting functions for a $M_{\rm ini} = 2M_{\odot}$. It shows a data point (blue stars) for each interpulse calculated by PARSEC. The red stars highlight the points effectively used in the linear fit, represented by the black line. The linear fit is of the type $y = bx + a$, whose values are displayed in each panel along with the respective correlation factor (or coefficient of determination), defined as $R^2 = 1 - \sum_i (y_{{\rm data},i} - y_i)/\sum_i (y_{{\rm data},i} - \langle y_{\rm data}\rangle)$, where y_i is the value calculated with the linear fit, $y_{{\rm data},i}$ is the real value for the same abscissa and finally $\langle y_{\rm data}\rangle$ is the arithmetic mean among all entries.

goal is to extrapolate beyond the final core mass reached by PARSEC, the fitting technique starts from the last three thermal pulse cycles and tries to extend the linear fit range as long as the correlation factor R^2 does not drop below a given threshold. This ensures that the last thermal pulses are weighted considerably more than the earlier pulses.

The shaping functions instead aim at defining the overall shape of luminosity and effective temperature inside the interpulse itself, namely how $T_{\rm eff}$ and $\log L$ vary with φ. The shape is found by normalizing the curves $T_{\rm eff}(\varphi)$ and $\log L(\varphi)$ as following:

$$\mathrm{Norm}(f) = \frac{f - \min(f)}{\Delta f} \tag{3.13}$$

where f represents the given quantity to normalize. The shaping functions are saved from the last calculated interpulse, and we also include the fraction of hydrogen luminosity, which we saw before (Section 3.2) directly converts in the core growth. In Figure 3.14 I show an example of shaping for the same $M_{\rm ini} = 2M_{\odot}$ track. The temperature shaping function is usually noisy, but the extrapolation scheme is overall stable regardless. The fitting and shaping functions collect and summarize all the information needed for the extrapolation from the PARSEC calculated pulse cycles and they are set for each iteration of the extrapolation scheme.

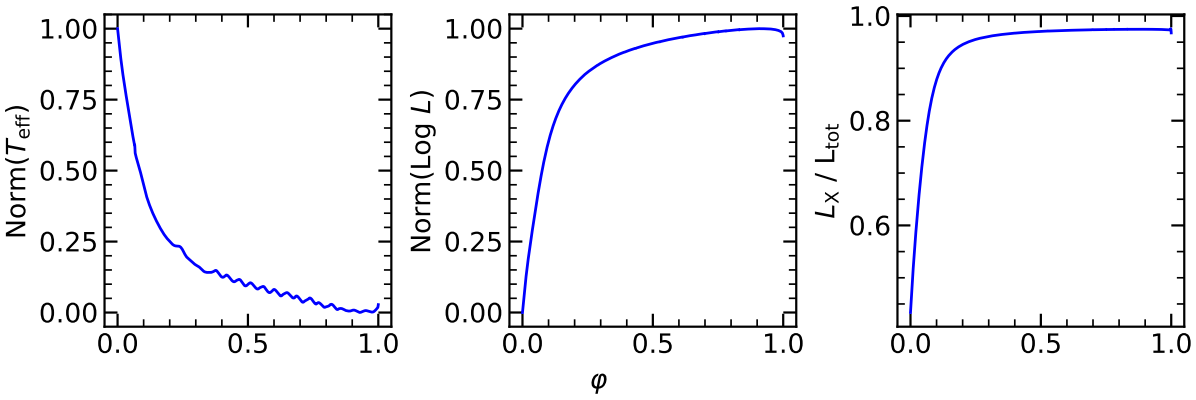

Fig. 3.14: Shaping functions for a $M_{\rm ini} = 2M_{\odot}$. Effective temperature and luminosity are normalized according to Eq. 3.13.

After this (important) preliminary step, the code can properly start the extrapolation from the last calculated interpulse. The first critical point, for the behavior of the full routine, is to choose whether a dredge-up takes place and its efficiency. In literature (Straniero et al., 2003; Izzard et al., 2004), there are recipes that can be used and depend upon the core mass, the envelope mass and metallicity. However, these are still based on complete models for calibration, which would introduce an unwanted mixing between different stellar evolutionary codes. To solve that, I decided to employ a shooting-like method: I define λ_0 as the TDU efficiency in the previous interpulse, $\lambda_{\rm max}$ as its maximum value during PARSEC evolution and $\delta\lambda$ as the maximum variation of the efficiency between two consecutive TDU events. These parameters are used to define a Gaussian distribution centered around λ_0 and with $\sigma = \delta\lambda$. If the probability of finding a $\lambda < 0.01$ is larger than 50% or $\lambda_0 = 0$ or even the remaining envelope mass $M_{\rm env} < 0.5$ M$_{\odot}$, then we set $\lambda = 0$. Otherwise, λ is randomly chosen according to the Gaussian distribution with the above parameters, but with an upper limit at $\lambda_{\rm max}$. The latter constraint comes from the idea of the extrapolation scheme, which is meant to be used to complete TP-AGB tracks that have already approached the end. Therefore, those tracks already overcome the maximum TDU efficiency and I want to limit the range of values that it can explore. This degree of randomness is coupled with the number of iterations of the full extrapolation scheme, which is usually set as $N_{\rm max} = 100 - 1000$. This means that we will have $N_{\rm max}$ estimates of the final core mass, which had explored different paths for the (remaining) λ evolution. When λ becomes zero (because PARSEC already reached that stage or due to the conditions above) I still want to keep some degree of randomization, that is to account for all the approximations somewhat introduced in the whole technique and give an error bar to our estimate. Therefore, when no TDU is present, I extract the wind efficiency parameter out of a log-uniform distribution $0.1 \leq \eta \leq 10$ (namely I draw values from a uniform distribution between -1 and 1), that multiplies the wind formula, which is the same PARSEC recipe.

Once λ (or η) has been extracted, the fitting functions are calculated at $M_{\rm core}$ and a series of checks that prevent the extrapolation going in unphysical regimes or for too many pulse cycles, therefore deciding if the new interpulse can start or not. If the extrapolation can proceed, then

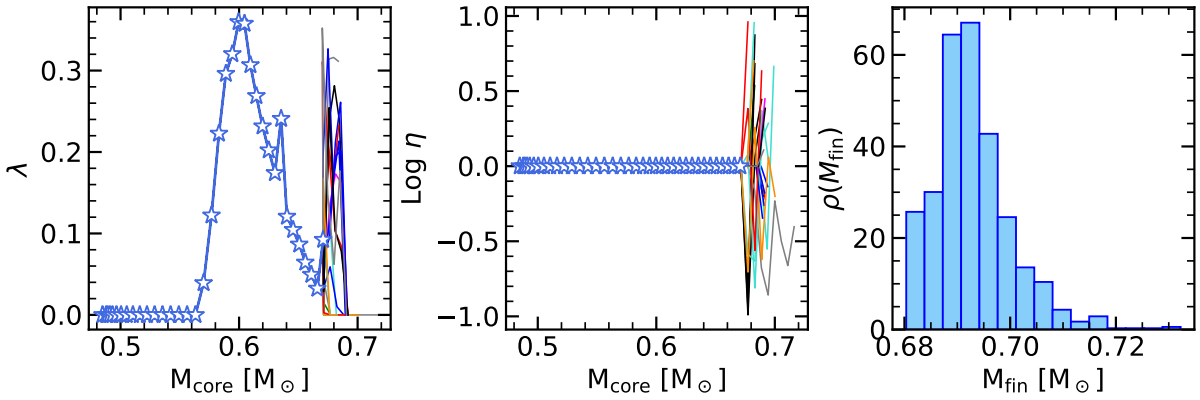

Fig. 3.15: Iterations of the extrapolation scheme applied to a $M_{\rm ini} = 2M_\odot$ track. The left and central panels show the value of λ and η respectively, where the star blue symbol with solid line marks the PARSEC part of the evolution. Afterward, it is followed by 25 examples (out of the total 1000) of the extrapolation part. The right panel shows the probability density of the resulting $M_{\rm fin}$ obtained by the extrapolation scheme with $N_{\rm max} = 1000$. The distribution average and standard deviation are $M_{\rm fin} = 0.692 \pm 0.007$.

the new starting point for the interpulse is set, that is $M_{\rm core}$ is reduced by $\Delta M_{\rm dup} = \lambda \Delta M_{\rm core}$ and the material with the intershell composition (left fixed from the last PARSEC thermal pulse) is homogenized into the envelope. The time variable φ now starts from 0 and goes to 1 in a user-defined number of equally spaced steps, usually 100. In every timestep luminosity and effective temperature are calculated by inverting Eq. 3.13, which are then used to calculate the mass loss, and the core mass is increased by an amount given by the energy conservation Eq. 3.6 considering only the hydrogen luminosity. Every time-step is saved to outer memory and printed into a text file (which can get pretty large if the number of simulations is large) and the code checks if the end of TP-AGB is reached within the interpulse, and if not proceeds to the next timestep until completing the whole interpulse at $\varphi = 1$. If the envelope is not completely removed after that, the code starts another interpulse stage.

Finally, the extrapolation scheme ends when a number $N_{\rm max}$ simulations equal is reached. The final estimate of the $M_{\rm fin}$ is the average of the obtained distribution, to which I assign the standard deviation as error on the estimate. An example of the distribution of $M_{\rm fin}$ with $N_{\rm max} = 1000$ is shown in Figure 3.15. The distribution is presented as probability density, found just by dividing the number of $M_{\rm core}$ obtained in each bin by $N_{\rm max}$ and the bin size. To obtain this result, the code run for about 40 seconds on a single core of the same Intel Xeon Gold 6238R CPU @ 2.20GHz cited before, and its workflow can be easily parallelized as each iteration is independent from the others, once the fitting and shaping functions are defined. In this particular case, the track was close to the end of the TP-AGB, it was missing ~ 4 thermal pulses and the carbon dust driven mass loss (Mattsson et al., 2010; Eriksson et al., 2014; Bladh et al., 2019) was already activated, granting $\dot{M} > 5 \times 10^{-6}$ M$_\odot$ yr^{-1}. Therefore, the code completed all the iterations without going outside the safe regime where extrapolation can be carried out. However, it may happen that the extrapolation scheme cannot peel the envelope if the PARSEC track stops too early. In these few cases, it provides a simple lower and upper limit employing

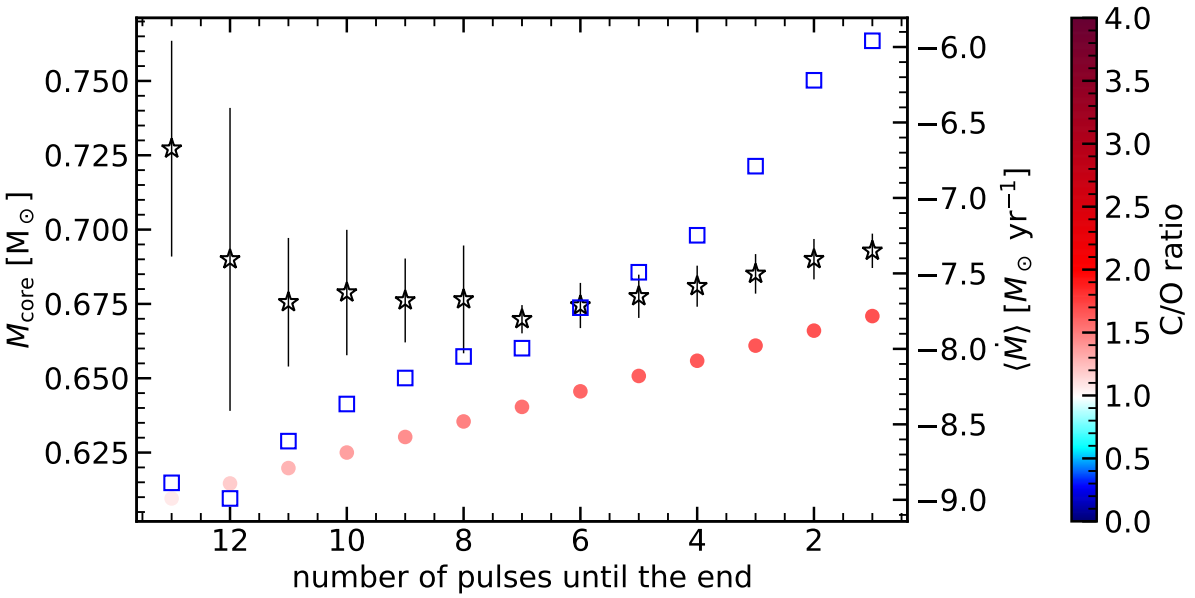

Fig. 3.16: Consistency test of the extrapolation scheme on the last 13 pulses of a 2 $M_\odot$ track. Each point on the x-axis corresponds to the n-th pulse until the end of PARSEC evolution. Colored circles (left y-axis) represent the PARSEC core mass with the colormap linked to the current surface C/O ratio, empty blue squares (right y-axis) the average mass-loss on the entire n-th pulse cycle, and the empty black stars (with errorbars, left y-axis) are the prediction of the final core mass given by the extrapolation scheme if applied at the same n-th thermal pulse.

Eq. 6 of Siess (2007) respectively using a fixed $\dot{M} = 10^{-4}$ $M_\odot$ yr^{-1} and 10^{-6} $M_\odot$ yr^{-1} and a fixed core mass rate taken from the last interpulse.

We can also check the extrapolation scheme consistency by using it on the same 2 $M_\odot$ track but starting from thermal pulses preceding the latter one calculated by PARSEC. I did so for the last 13 thermal pulses of our prototype 2 $M_\odot$ track, and results are shown in Figure 3.16. We can notice that the average mass loss increases steadily approaching the end of evolution, and a sudden increase is present in the last 3 thermal pulses. That is where the track activates the carbon dust-driven mass loss, which is considerably larger than the pulsation-driven one. Using later thermal pulses as a starting point clearly stabilizes the results of the extrapolation scheme, which goes accordingly with the mass loss increase, as it means there is little time remaining in the TP-AGB phase. We can also see how the error on the prediction gets smaller because there is little room for variation if only a few pulses are left before entering the post-AGB.

To wrap up this section, I want to remark that the extrapolation scheme offers a fast and reliable way to get a first-order prediction of the final mass of the white dwarf, which is useful to get a feeling of the results and can help to decide how and where to spend the computing time for producing more accurate estimates.

CHAPTER 4

The Initial-Final Mass Relation of White Dwarfs

Simulations give you numbers, no truth!
It is then your duty to say how close they really are..

Unknown Sardinian astrophysicist

This Chapter is the culmination of all my efforts spent in developing the PARSEC code, producing the models, assuring their quality, and analyzing the results. The results have been published in the paper *The Role of the Third Dredge-up and Mass Loss in Shaping the Initial–Final Mass Relation of White Dwarfs* (Addari et al., 2024), which is the main source for the Chapter.

In the following, I will discuss the crucial role of the IFMR in understanding the evolution and the physical processes happening in stars. I investigated the IFMR in the initial mass range of $0.8 \leq M_{\rm ini}/{\rm M}_{\odot} \leq 4$ using full PARSEC evolutionary tracks and terminated by COLIBRI computations to completely remove the envelope and reach the final core mass. Recent works have shown that the interaction between third dredge-up episodes and stellar winds in carbon stars in the TP-AGB phase might interrupt the supposed monotonicity of the IFMR with a kink, found in the range $M_{\rm ini} \approx 1.65 - 2.10$ M$_{\odot}$. To reproduce the kink in the IFMR we studied the role of convective overshooting at the bottom of the convective envelope and the borders of the pulse-driven convective zone, whose effects result in the magnitude of the mass loss. The comparison of our models with observations suggests that $f_{\rm env}$ cannot be kept constant with the initial mass, which would otherwise produce only monotonic IFMR. I also discuss possible degeneracy with $f_{\rm pdcz}$ and the information needed to overcome it, providing valuable insight on the internal mixing processes during the TP-AGB phase.

4.1 General overview on the IFMR

Low- and intermediate-mass stars all end their evolution through the thermally pulsing asymptotic giant branch phase, during which they eject the hydrogen-rich envelope in the interstellar medium, only leaving a carbon-oxygen white dwarf as a remnant (Herwig, 2005; Karakas & Lattanzio, 2014). By this point, I showed that the modeling of the TP-AGB phase is still plagued by uncertainties, due to the processes acting during the evolution that are hard to model from first principles, such as convective mixing, stellar wind, long-period variability, and recurrent dredge-up episodes. The tight interplay of these processes makes the picture greatly dependent on the current stage of the evolution and on the numerical treatment behind the models. In the previous Chapters, I just hinted that recurrent TDU events can lift the photospheric carbon-oxygen ratio above unity, which is confirmed by the presence of carbon stars in the coolest and most luminous regions (compared to the luminosity of low- and intermediate-mass stars) of color-magnitude diagrams. However, the TDU is highly dependent on the prescriptions and numerical treatment (Frost & Lattanzio, 1996; Herwig, 2000), which populate the literature with a variety of results and make it difficult to compare the models (Herwig, 2000; Stancliffe et al., 2005; Weiss & Ferguson, 2009; Cristallo et al., 2011; Marigo et al., 2013; Karakas, 2014; Ventura et al., 2018). One method for constraining the efficiency of the TDU is to reproduce the carbon star luminosity functions in various galaxies with different age-metallicity relations and known star formation histories (Groenewegen & de Jong, 1993; Marigo et al., 1999; Marigo & Girardi, 2007; Pastorelli et al., 2019, 2020). Another approach to calibrating the TDU in Milky Way carbon stars is provided by the semi-empirical initial-final mass relation of C-O white dwarfs, as demonstrated in several studies (Kalirai et al., 2014; Marigo et al., 2020; Marigo, 2022).

In this Ph.D. project and this Chapter, I choose the second approach, and I focus on the semi-empirical IFMR, aiming to replicate its behavior using recent data and extracting information on the TDU through fully self-consistent TP-AGB stellar models. To reconstruct the semi-empirical IFMR, I will specifically examine the influence of mass loss and convective overshooting applied to the base of the convective envelope and the borders of the pulse-driven convective zone. In general, the IFMR predicts that more massive stars will produce more massive remnants. Over the years, improvements in the semi-empirical IFMR have been achieved thanks to new observations and refined treatments in stellar evolution codes (Weidemann, 2000; Williams et al., 2004; Kalirai et al., 2008, 2009; Salaris et al., 2009; Williams et al., 2009; Kalirai et al., 2014; Cummings et al., 2018, 2019, and references therein). The recent addition of new WD data from open clusters aged 1.5-2.5 Gyr, Marigo et al. (2020) allowed to identify a kink in the IFMR at about $M_{\rm ini} \simeq 1.65 - 2.10 M_{\odot}$, which interrupts the monotonic trend. The white dwarfs at the peak, all members of the open cluster NGC 7789, have masses of $\simeq 0.70 - 0.74 M_{\odot}$, which were previously associated with stars having $M_{\rm ini} \simeq 3 M_{\odot}$. The IFMR kink is interpreted as indicative of the lowest-mass stars in the Milky Way that evolved into carbon stars during the TP-AGB phase. According to Marigo et al. (2020), these carbon stars likely underwent

shallow third dredge-up events, resulting in low photospheric C/O ratios and modest carbon excess relative to oxygen. Under these conditions, carbonaceous dust grains cannot condense in sufficient quantities to induce a strong wind, leading to an extended TP-AGB lifetime and greater core mass growth than typically predicted. Theoretically, this behavior is attributed to mass-loss prescriptions for carbon stars that depend on carbon excess, based on state-of-the-art dynamical models (Mattsson et al., 2010; Eriksson et al., 2014; Bladh et al., 2019). An independent study of AGB stars in Galactic open clusters using Gaia EDR3 recently confirmed these findings (Marigo et al., 2022c). In the initial mass range of the kink, they identified carbon stars with dust-free spectra and irregular small-amplitude pulsations (indicating very low mass loss, as estimated from spectral energy distribution fitting) with current core masses of $\simeq 0.67 - 0.7\,M_{\odot}$, consistent with WD masses (see Figure 8 of that paper).

The whole project has been mainly a theoretical work, giving as granted the estimates on the $M_{\rm ini}$ and $M_{\rm f}$ of the white dwarfs, which comes from the works by Cummings et al. (2018) and Marigo et al. (2020). However, it is important to know how these are determined, and that explains why we refer to the IFMR retrieved from fits of the $M_{\rm f} - M_{\rm ini}$ data as a *semi-empirical* relation. The final mass $M_{\rm f}$ of the white dwarf is retrieved from the cooling age, which is a byproduct of WD cooling models that are fitted to the surface gravity and effective temperature of the observed WD. The initial mass, or the progenitor mass, estimation is trickier. Theoretical isochrones are fitted to find the turn-off luminosity of the cluster, which gives an estimate of the age of the cluster. The difference between the cluster age and the WD cooling age gives the lifetime of the progenitor, which gives the initial mass $M_{\rm ini}$ if compared with stellar evolution models. Therefore, from cluster observations, one needs the color and magnitude of each cluster member, an estimate for the metallicity and the extinction, the latter needed for the distance determination. On top of these requirements, depending on the cluster, it may be needed to carefully assess the membership of the observed white dwarf, otherwise the progenitor age might not be as accurate. A deep discussion on the possible model inconsistencies (and a better explanation of the method to get the masses) is present in the work by Salaris et al. (2009), who also propagates the systematic errors in the estimates of those inconsistencies in the theoretical ingredients are indeed present.

Here I want to remark that the initial mass $M_{\rm ini}$ estimate is almost unaffected by the TP-AGB part of the evolution of the theoretical models. The TP-AGB duration is so short compared to the rest of the evolution that the progenitor lifetime, and therefore mass, is minimally impacted. Therefore, all the heterogeneity in the number of thermal pulses, dredge-up efficiency, and growth of the core can be safely neglected to evaluate the initial mass $M_{\rm ini}$. This feature allows us to explore the parameter space in the TP-AGB models without running the full procedure of getting the $M_{\rm ini}$ every time we change the input parameters in the TP-AGB phase. That is also the reason why I fix the parameters prior to the TP-AGB phase as the $M_{\rm ini}$ provided by Cummings et al. (2018) and Marigo et al. (2020) already use the `PARSEC` isochrones and tracks.

$f_{\rm pdcz}$	$f_{\rm env}$						
	0.047*	0.056	0.064	0.096	0.128	0.144	0.160
0.000	✓	×	✓	×	✓	×	×
0.001	✓	✓	✓	✓	✓	✓	✓
0.002	✓	×	✓	×	✓	×	×
0.004	✓	×	✓	×	✓	×	×
0.008	✓	×	✓	×	✓	×	×
0.016	✓	×	✓	×	✓	×	×
0.032	✓	×	×	×	×	×	×
0.064	✓	×	×	×	×	×	×

Tab. 4.1: Sampled values of ($f_{\rm env}$, $f_{\rm pdcz}$) in the TP-AGB phase. Checkmarks correspond to the calculated sets of tracks and crosses to combinations of overshooting parameters that have not been explored.

4.2 Details on the input physics

The common input physics has already been presented in Section 2.2.3, but we will now complete the picture of the models computed in Addari et al. (2024).

Our sets of TP-AGB tracks have a solar-like metallicity Z = 0.014 and solar-scaled composition from Caffau et al. (2011). The helium content is given by $Y = Z \cdot \Delta Y/\Delta Z + Y_{\rm p} = 0.273$ with $Y_{\rm p} = 0.2485$ (Komatsu et al., 2011) and $\Delta Y/\Delta Z = 1.78$ (Bressan et al., 2012). Almost everything has already been set in the previous Chapters, meaning that we use the new opacity tables with nodes in the C, N, and O abundances, our shell-shifting scheme, and a particular prescription for the overshooting. In Section 2.2.3 we discussed the overshooting in the envelope only prior to the TP-AGB phase, but this work aims to investigate its effect during the TP-AGB itself. For this reason, I will refer to $f_{\rm env}$ and $f_{\rm pdcz}$ as the value of envelope and pulse-driven convective zone (both top and bottom border) overshooting efficiency only in the TP-AGB phase (see also final paragraph of Section 4.1).

I calculated a total of 439 TP-AGB tracks divided into 24 sets, where the evolution before the TP-AGB has been computed with the fiducial value of envelope overshooting, as explained in Section 2.2.3. Therefore, each set is identified by a couple of values ($f_{\rm env}$, $f_{\rm pdcz}$) and the spanned range is summarized in Table 4.1. The track initial mass is comprised in the range $0.8 \leq M_{\rm ini}/{\rm M}_\odot \leq 4$ (with only a few sets extending to $5{\rm M}_\odot$) with a step of $0.05 \leq \Delta M_{\rm ini}/{\rm M}_\odot \leq 0.3$ and a finer grid around the IFMR kink. The evolution is calculated from the PMS to the furthest point in the TP-AGB (see Section 4.4), but for the track experiencing the He-flash the code interrupts at the tip of the RGB. The track is then restarted with a proper ZAHB model, starting from a mass equal to the mass left at the RGB tip assuming the star does not lose mass in the transition. Our ZAHB models are computed with fiducial envelope overshooting, and clearly, $f_{\rm pdcz}$ does not matter before TP-AGB. I find that the He-flash is encountered by tracks

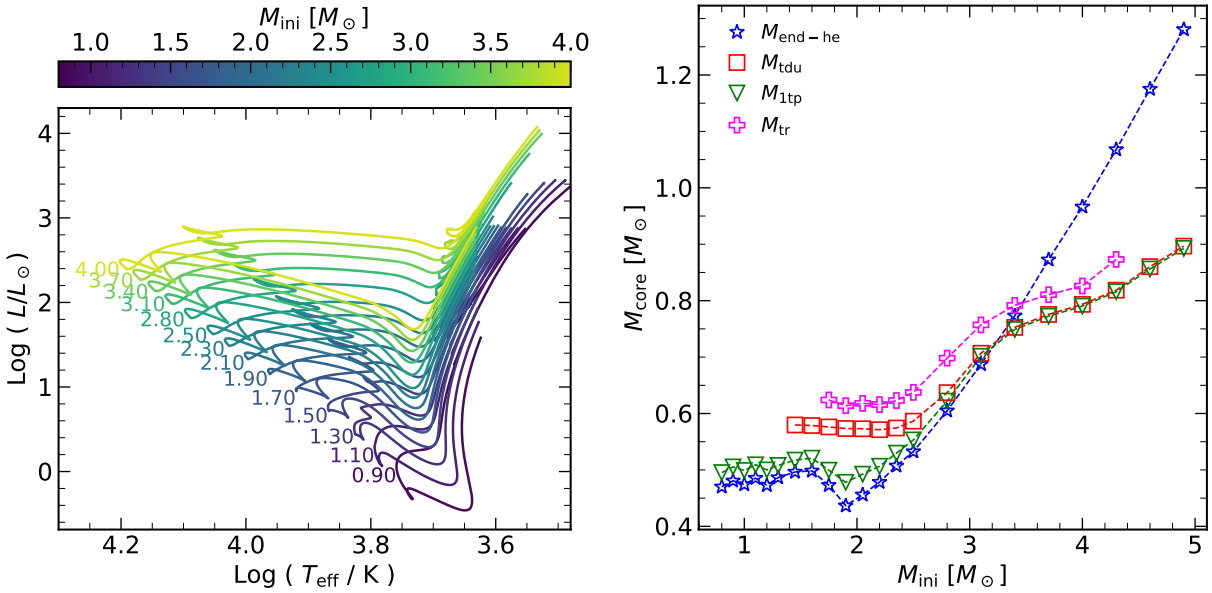

Fig. 4.1: In the left panel, H-R diagram for the fiducial value of envelope overshooting and no PDCZ overshooting, from the PMS up to the onset of the TP-AGB phase. A subset is shown for clarity. In the right panel, core mass at different stages of the evolution for fiducial envelope overshooting and $f_{\rm pdcz} = 0.001$. $M_{\rm end-he}$ (blue stars) refers to the end of central He-burning, $M_{\rm 1tp}$ (green triangles) to the first thermal pulse, $M_{\rm tdu}$ (red squares) the first occurrence of TDU and finally $M_{\rm tr}$ (pink plus) refers to the core mass at which the star moves from M- to C-type.

with $M_{\rm ini} \leq 1.85 M_\odot$ with an accuracy of $0.05 M_\odot$.

4.3 Evolutionary properties

In this section, I discuss the evolutionary characteristics of our models, emphasizing the evolution of the core mass. Its definition changes based on the evolutionary stage. The stages before the TP-AGB phase of the PARSEC tracks have been recently detailed by Nguyen et al. (2022). Before the TP-AGB phase, $M_{\rm core}$ is defined as the mass of the hydrogen-exhausted core. To consider the possibility that white dwarfs might retain a thin hydrogen layer atop the He-intershell and CO core (Saumon et al., 2022), I define the core mass during the TP-AGB phase as:

$$M_{\rm core} = m(X = 0.5 X_{\rm surf}) \tag{4.1}$$

where m represents a generic mass coordinate, and X and $X_{\rm surf}$ indicate the hydrogen abundance at any mesh point and at the surface, respectively. Furthermore, I define the onset of the TP-AGB phase as the point where the thickness of the He-intershell decreases below 0.1 $M_\odot$ (Dotter, 2016). The left panel of Figure 4.1 illustrates the evolution in the HR diagram of a sub-sample within the spanned mass range up to the beginning of the TP-AGB phase. With the assumptions for $f_{\rm env}$, this portion of the evolution is consistent across all sets of tracks. Before the TP-AGB phase, the core is built up by the ashes of both core and shell hydrogen and helium burning. This growth can be limited by the first and second dredge-up events (FDU and SDU, respectively),

$M_{\rm ini} = 3.70 M_\odot$				$M_{\rm ini} = 4.00 M_\odot$			
$f_{\rm env}$	0.047	0.096	0.144	$f_{\rm env}$	0.047	0.096	0.144
$M_{\rm core}$	0.791	0.778	0.782	$M_{\rm core}$	0.810	0.802	0.810
$X_{\rm surf}$	6.538E-01	6.522E-01	6.530E-01	$X_{\rm surf}$	6.398E-01	6.389E-01	6.388E-01
$Y_{\rm surf}$	3.321E-01	3.337E-01	3.330E-01	$Y_{\rm surf}$	3.462E-01	3.471E-01	3.471E-01
$X_{\rm C12,surf}$	1.456E-03	1.447E-03	1.445E-03	$X_{\rm C12,surf}$	1.423E-03	1.417E-03	1.413E-03
$X_{\rm O16,surf}$	5.137E-03	5.106E-03	5.098E-03	$X_{\rm O16,surf}$	5.011E-03	4.985E-03	4.974E-03
$\rm C/O_{surf}$	3.964E-01	3.965E-01	3.964E-01	$\rm C/O_{surf}$	3.975E-01	3.979E-01	3.977E-01

Tab. 4.2: Track properties at the onset of TP-AGB phase, after SDU. $M_{\rm core}$ is in solar units.

which are directly influenced by the efficiency of envelope overshooting. The goal is to examine the evolution of core mass and the final mass of the white dwarf formed at the end of the process. By setting a uniform $f_{\rm env}$ for all initial masses before the TP-AGB phase, we standardize the penetration of the envelope during the FDU and SDU. Observations of the RGB bump help constrain $f_{\rm env}$ during the FDU (Alongi et al., 1991; Fu et al., 2018), while during core helium burning, $f_{\rm env}$ affects the extension and position of blue loops (Tang et al., 2014). However, there are no direct constraints on the overshooting efficiency during the SDU. Therefore, I aim to ensure that the core mass and surface C/O ratio are minimally affected by the SDU in tracks with varying $f_{\rm env}$ values. The SDU significantly impacts stars with $M_{\rm ini} \gtrsim 3.5 M_\odot$ (Karakas & Lattanzio, 2014). Hence, I calculated a few intermediate-mass star tracks using different $f_{\rm env}$ values from the PMS phase, diverging from the standard $f_{\rm env} = 0.047^\star$. In the right panel of Figure 4.1, various mass thresholds are depicted, with definitions provided in the figure caption. The condition $M_{\rm end-he} > M_{\rm 1tp}$ indicates which tracks undergo the SDU, consistent with Karakas & Lattanzio (2014). Table 4.2 presents the main properties at the onset of the TP-AGB phase for two models with $M_{\rm ini} = 3.7 M_\odot$ and $M_{\rm ini} = 4 M_\odot$, computed with different $f_{\rm env}$ values from the PMS phase. Specifically, the core mass after the second dredge-up and the carbon-to-oxygen ratio are the primary properties influencing the subsequent evolution of the track. These quantities differ by less than 2% in models with varying $f_{\rm env}$ values (from the PMS), and no clear trend with increasing overshooting penetration is observed. Thus, I conclude that these differences are likely due to purely numerical features inherent in the mixing treatment. The tests confirmed that the SDU is not significantly affected by the choice of envelope overshooting, at least up to $M_{\rm ini} \simeq 4 M_\odot$. Consequently, I modify the $f_{\rm env}$ value only during the TP-AGB phase, ensuring consistency with previous calibrations. The PDCZ only appears during a thermal pulse, thus the prior evolution remains unaffected by $f_{\rm pdcz}$.

After setting the evolution until the onset of the first thermal pulse, I want now to discuss the properties of the TP-AGB evolution, focusing on the TDU efficiency λ and its consequences. It is important to acknowledge that λ is highly sensitive to both the numerical details and the physical inputs of the model (Frost & Lattanzio, 1996; Mowlavi, 1999). To ensure accurate

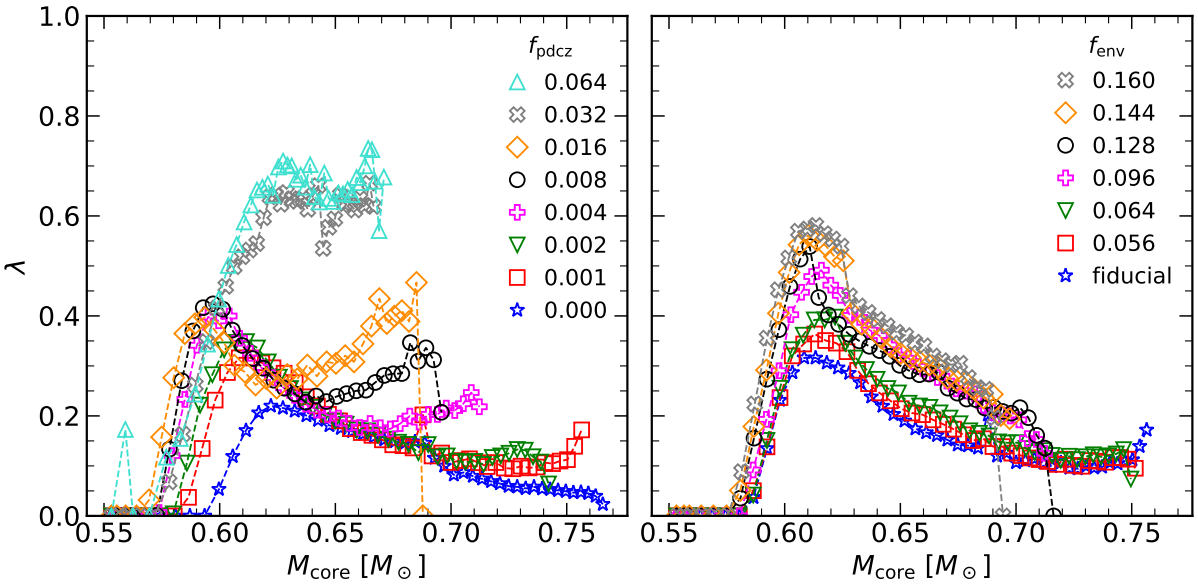

Fig. 4.2: Evolution of λ as a function of the core mass. Both panels show a $M_{\rm ini} = 2.50 M_\odot$ model. Left panel shows all $(0.047^\star, f_{\rm pdcz})$ models. Right panels shows $(f_{\rm env}, 0.001)$ models. Each symbol corresponds to a thermal pulse.

predictions, it is crucial to maintain consistent numerical prescriptions when calibrating the physical parameters to avoid potential systematic errors. Additionally, we note that λ primarily depends on the core mass and the envelope mass at a given metallicity (Straniero et al., 2003). These considerations serve as our reference point for the subsequent analysis of our TP-AGB tracks.

Figure 4.2 illustrates the evolution of λ relative to $M_{\rm core}$ for a star with $M_{\rm ini} = 2.5 M_\odot$ for each set. Generally, increasing envelope overshooting leads to more efficient dredge-up, a standard behavior commonly reported in the literature, as greater overshooting depth destabilizes deeper mass shells. However, the λ-curves exhibit a distinctive pattern with varying $f_{\rm pdcz}$. As expected, the TDU efficiency increases with the overshooting parameter (in this case, PDCZ), consistent with Herwig (2000). Nevertheless, the shape of the λ-curves at varying $f_{\rm pdcz}$ shows a prominent double maximum, rather than the usual bell-like profile observed in other studies (Straniero et al., 1997, 2003; Cristallo et al., 2011; Marigo, 2022). I noted that the second rise in λ with $M_{\rm core}$ begins approximately at $M_{\rm tr}$, where the mass-loss rate transitions from a Blöcker wind to a dust-free pulsation-driven regime. I propose that this transition moves the track back to a region of the ($M_{\rm core}$, $M_{\rm env}$) plane where TDU is more favorable (Straniero et al., 2003).

It is important to highlight that λ alone is not sufficient to fully determine a star's evolution. Instead, the interplay between the growth of the core mass and the composition of the dredge-up material is pivotal. Figure 4.3 presents an example of the mass-loss rate evolution over time for a $M = 2.50 M_\odot$ star from the set (0.128,0.001). Changing $f_{\rm env}$ or $f_{\rm pdcz}$ affects the evolution, as it alters the transition to a carbon star initially and modifies the duration of the dust-free phase with low mass-loss rates. Predicting the exact impact on the total TP-AGB lifetime and core mass is challenging due to the mild degeneracy between the two overshooting parameters. $f_{\rm env}$

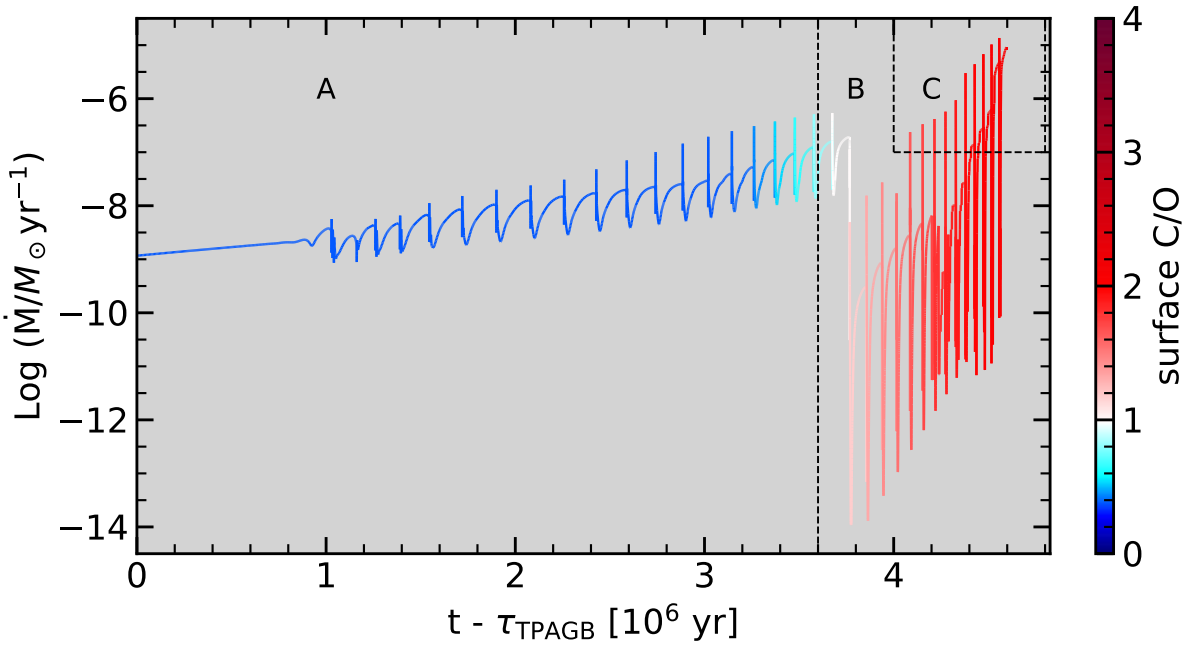

Fig. 4.3: Mass-loss evolution of $M_{\rm ini} = 2.5 M_\odot$ with $f_{\rm env} = 0.128$ and $f_{\rm pdcz} = 0.001$. $\tau_{\rm TPAGB} = 1.350$ Gyr is the time spent before the beginning of TP-AGB. A, B and C mark the main three regimes of the mass-loss. A: wind for O-rich stars (Bloecker, 1995); B: dust-free pulsation-driven wind (Marigo et al., 2020); C: carbon dust-driven wind (Mattsson et al., 2010; Bladh et al., 2019).

primarily influences the TDU efficiency (as shown in Figure 4.2), whereas $f_{\rm pdcz}$ also affects the intershell composition, as illustrated in Figure 4.4. Generally, deeper PDCZ overshooting increases the carbon abundance in the intershell but also raises the oxygen abundance, thereby reducing the overall $\rm C/O_{intershell}$ ratio of the material dredged up to the surface.

After analyzing the effect of $f_{\rm env}$ and $f_{\rm pdcz}$ on λ, we turn our attention to their impact on the mass thresholds previously presented in Figure 4.1. Notably, $M_{\rm end-he}$ and $M_{\rm 1tp}$ remain unaffected due to our assumptions. Figure 4.5 illustrates how the extent of the overshooting region (both in the envelope and PDCZ) influences $M_{\rm tdu}$ and $M_{\rm tr}$. The effect of $f_{\rm env}$ is limited, with changes in both $M_{\rm tdu}$ and $M_{\rm tr}$ being less than 0.05 $M_\odot$ in the low mass range. For $M_{\rm ini} \gtrsim 2.8 M_\odot$, $M_{\rm tdu}$ remains unchanged as it occurs at the first thermal pulse, independent of the overshooting parameters. In contrast, $f_{\rm pdcz}$ has a greater impact on $M_{\rm tdu}$ and $M_{\rm tr}$. The initial occurrence of TDU is significantly lowered in core mass with increasing $f_{\rm pdcz}$, particularly for oxygen-rich intershells. Additionally, TDU begins at even lower initial masses, dropping from $M_{\rm ini} \simeq 1.6 M_\odot$ with $f_{\rm pdcz} = 0.000$ to $M_{\rm ini} \simeq 1.3 M_\odot$ for $f_{\rm pdcz} \geq 0.004$. This effect is even more pronounced when observing the transition core mass $M_{\rm tr}$ from M-type to C-type. A small $f_{\rm pdcz}$ value can cause $M_{\rm tr}$ to decrease from approximately 0.7 $M_\odot$ to around 0.63 $M_\odot$. This significantly lowers the initial mass threshold for becoming a C-type star from $M_{\rm ini} \simeq 2.3 M_\odot$ with no PDCZ overshooting to $M_{\rm ini} \simeq 1.4 M_\odot$ at $f_{\rm pdcz} \simeq 0.008 - 0.016$. However, for $f_{\rm pdcz} > 0.016$, the trend reverses due to a combination of higher TDU efficiency and a C-deficient intershell, leading to delayed or non-existent transitions. For the extreme case of $f_{\rm pdcz} = 0.064$, only three tracks become C-type,

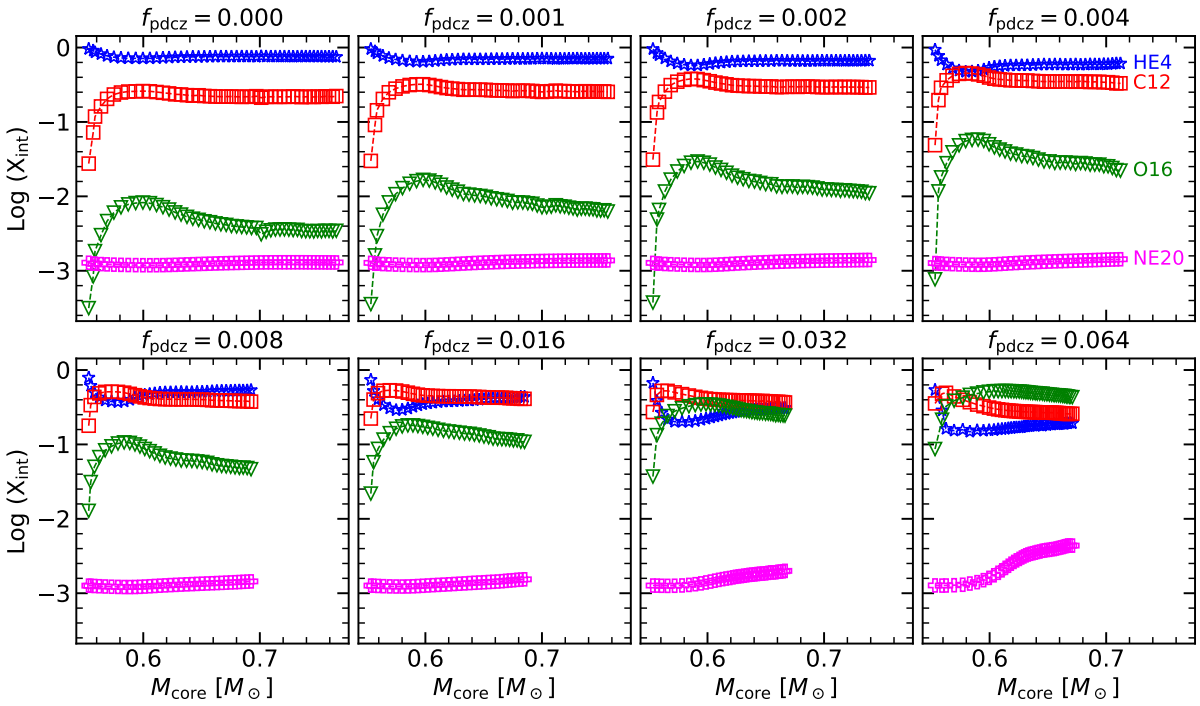

Fig. 4.4: Intershell abundances (in log scale) of ^{4}He, ^{12}C, ^{16}O, and ^{20}Ne after every calculated pulse for every ($0.047^\star$,f_{pdcz}) couple and $M_{ini} = 2.50 M_\odot$.

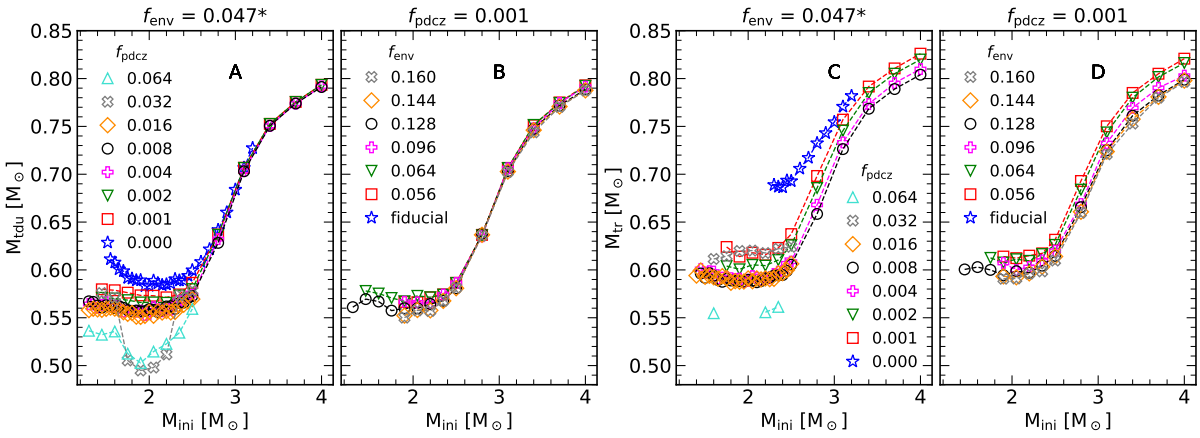

Fig. 4.5: Core mass at the first occurrence of TDU (A and B panels) and core mass when $C/O_{surf} > 1$ (C and D). $f_{pdcz} \geq 0.016$ models are limited to $M_{ini} \leq 2.5 M_\odot$. $f_{pdcz} = 0.000$ set is limited to $M_{ini} \leq 3.2 M_\odot$. A and C panels: ($0.047^\star$,f_{pdcz}) models. B and D panels: (f_{env},0.001) models. f_{env} = 0.056, 0.096, 0.144, 0.160 are limited to $M_{ini} \geq 1.9 M_\odot$.

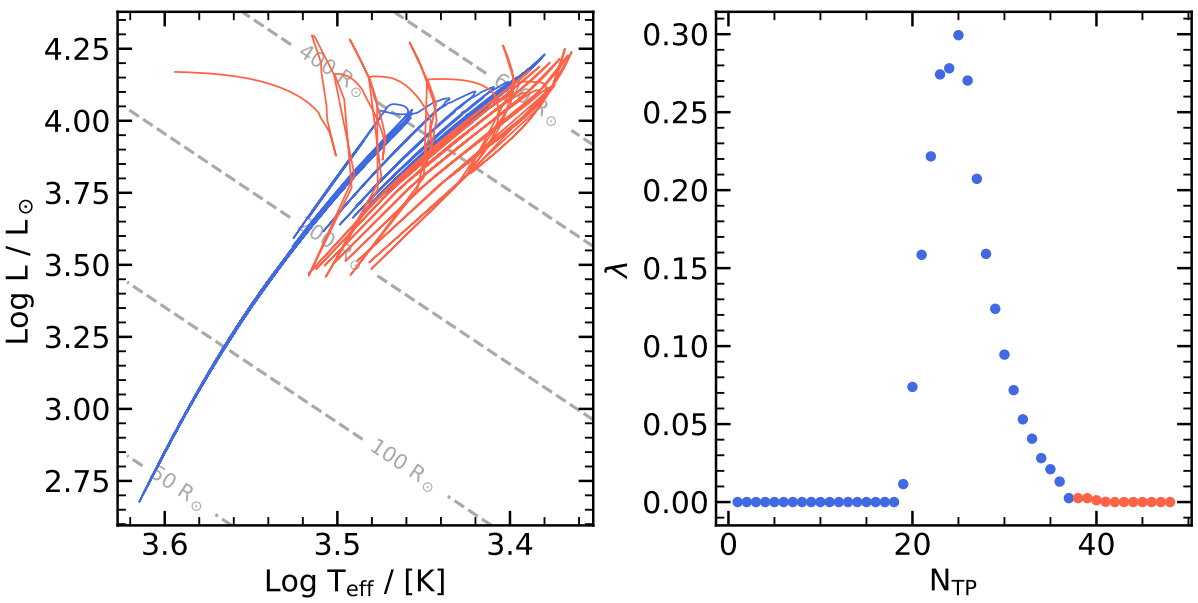

Fig. 4.6: Left panel: evolutionary track of a TP-AGB model with $M_{\rm ini}$ = 1.85 $M_\odot$. The PARSEC and COLIBRI sections of the track are colored in blue and red, respectively. Right panel: TDU efficiency as a function of the TP number.

but they quickly revert to M-type due to dredge-ups from an oxygen-rich intershell.

We have investigated the primary effects of the two overshooting parameters and their interplay with mass loss on the quantities that shape the IFMR. These considerations are fundamental in determining the final form of the initial-final mass relation, which will be discussed in the following section.

4.4 Estimating the final core mass

In Section 3.3 I already discussed the difficulties in ending TP-AGB tracks and the solution I came up with. The extrapolation scheme can give a first-order estimate with a (usually small) error bar, which is effective enough to apply to every track that cannot reach the proper end of evolution. This first estimate serves to give us the direction for further analysis, with a more appropriate tool, that is the COLIBRI code (Marigo et al., 2013) I briefly presented in 3.3.3. COLIBRI calculations start from the last TP computed by PARSEC, at the quiescent stage of the pre-flash luminosity maximum. The structural parameters are imported into COLIBRI from the final PARSEC model, including the intershell chemical composition, which remains constant until the end of the evolution. Figure 4.6 shows an example of the transition between PARSEC and COLIBRI computations. This TP-AGB $M_{\rm ini}$ = 1.85 $M_\odot$ model becomes a carbon star, has a final core mass of 0.726 $M_\odot$, and fits within the IFMR kink, consistent with observational data (Cummings et al., 2018; Marigo et al., 2020). We also observe that the TDU is already quenched when COLIBRI begins its computations. Consequently, the number of pulses computed with COLIBRI ($N_{\rm COLIBRI}$) is modest in most tracks, typically $N_{\rm COLIBRI} \simeq 1-2$, except for a few cases

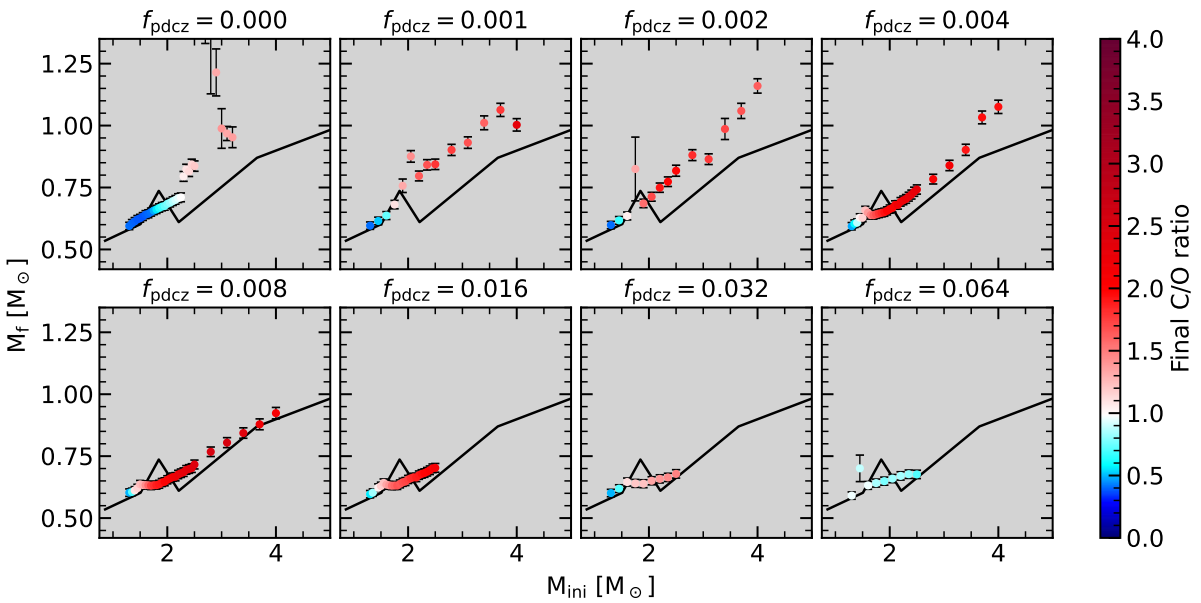

Fig. 4.7: Final core masses for fixed envelope overshooting $f_{env} = 0.047^\star$ and varying PDCZ overshooting. The solid line is the semi-empirical IFMR found by Marigo et al. (2020) and Cummings et al. (2018). Sets with large overshooting efficiency are limited to $1.3 \leq M_{ini}/M_\odot \leq 3.2$, sufficient to show they cannot reproduce the IFMR's kink. The final mass is estimated with the extrapolation technique (Section 3.3). A slight oscillation of the result is produced by the extrapolation technique, as well as the error bars.

where $N_{\texttt{COLIBRI}} \simeq 8 - 10$.

I now want to discuss how the choice of (f_{env}, f_{pdcz}) impacts the shape of the IFMR. Marigo et al. (2020) demonstrated that the IFMR is not monotonic and shows a prominent kink at around $1.65 - 2.1 M_\odot$ in the initial mass range. This feature is explained with the chemical enrichment caused by recurrent TDU events, coupled with the diverse regimes of mass loss with the carbon excess C−O. Stars with a carbon excess in the range $8.2 \lesssim (\mathrm{C-O})_{min} \lesssim 9.2$ experience extended lifetimes due to weaker winds (B-regime in Figure 4.3), allowing the core to grow beyond the usual monotonic trend. One advantage of employing purely synthetic or hybrid evolutionary codes is that the TDU efficiency λ can be directly calibrated from the IFMR, as it is treated as a free parameter, without the constraints imposed by more fundamental parameters like convective overshooting efficiency. Instead, our goal is to reproduce the shape of the IFMR by setting the values of (f_{env}, f_{pdcz}), which have a broader impact than simply adjusting λ. Figure 4.7 and Figure 4.8 illustrate the IFMR for varying f_{pdcz} and f_{env}, respectively. In most cases, a monotonic trend is evident, without any kink. We can observe that the low mass tracks ($M_{ini} \lesssim 1.5 M_\odot$) align closely with the expected IFMR regardless of the chosen parameters. This is because these tracks experience very shallow or no dredge-up, resulting in similar core mass evolution despite different (f_{pdcz}, f_{env}) values. In contrast, for intermediate-mass stars, most models overestimate the final mass predicted by the semi-empirical IFMR. The discrepancy diminishes progressively with increasing f_{env} or f_{pdcz}, indicating that a more efficient TDU is required at these initial masses. This finding aligns with previous IFMR calibrations (Marigo et al., 2020; Marigo,

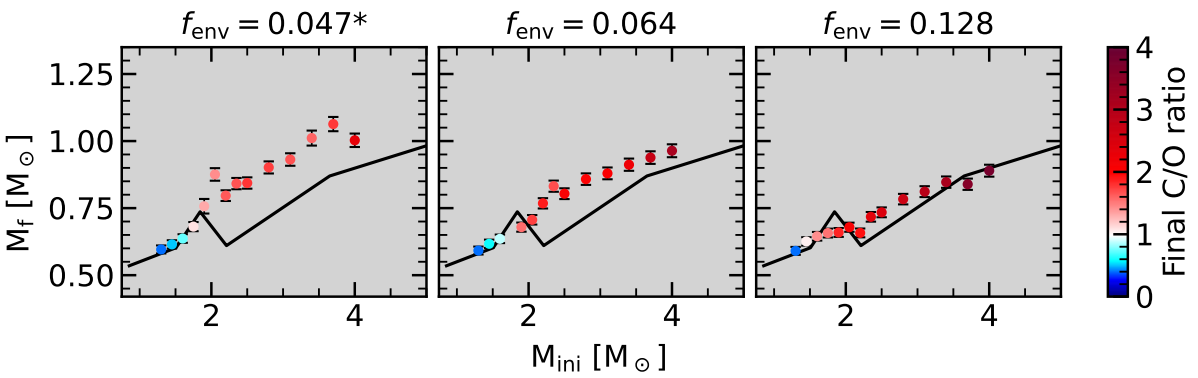

Fig. 4.8: Final core masses for fixed PDCZ overshooting $f_{pdcz} = 0.001$ and varying envelope overshooting. The solid line is the a fit to the semi-empirical IFMR of Marigo et al. (2020) and Cummings et al. (2018). The final mass is estimated with the extrapolation technique (Section 3.3).

2022), which suggest that λ_{max} increases with the initial mass. Our results indicate that a single set of overshooting parameters cannot reproduce the kink at $M_{ini} \simeq 1.65 - 2.10 M_\odot$.

At this point, we still have two parameters influencing the IFMR shape. For the rest of the discussion, I fix the value of f_{pdcz} and increase the TDU efficiency by adjusting f_{env} only, thereby maintaining a constant intershell composition (see Figure 4.4). We will address the robustness of this assumption later in this section. Under this assumption, I can immediately discard the extreme cases $f_{pdcz} = 0.000$ and 0.064. The latter fails to produce any carbon stars, while the former shows very weak dredge-ups across the entire mass range. Consequently, the first carbon stars emerge at $M_{ini} \simeq 2.30 - 2.40 M_\odot$, whereas lower initial masses are expected to form carbon stars (Marigo et al., 2022c). Figure 4.7 clearly demonstrates that even small values of PDCZ overshooting, compared to $f_{pdcz} = 0.000$, significantly impact the IFMR. Sets with $f_{pdcz} = 0.001 - 0.002$ sufficiently accommodate all initial masses up to the kink maximum at $M_{ini} \simeq 1.85 M_\odot$. To select our optimal final set, I choose $f_{pdcz} = 0.001$ since $f_{pdcz} > 0.002$ results in overly efficient TDU events (both in terms of envelope penetration and carbon abundance in the intershell) even with the fiducial value ($f_{env} = 0.047^\star$) of envelope overshooting. Having set f_{pdcz}, we can adjust f_{env} until a satisfactory fit is achieved, and then complete these tracks with `COLIBRI` to obtain more accurate estimates of the final mass. Figure 4.9 shows the final IFMR overlaid with observational data used in previous works (Cummings et al., 2018; Marigo et al., 2020; Canton et al., 2021), and Figure 4.10 illustrates the impact of each dredge-up on the same set of tracks. I collect the properties of the final set of tracks in Table 4.3.

As expected, the negative slope region ($M_{ini} \simeq 1.85 - 2.20 M_\odot$) indicates an increasing f_{env}, even up to four times greater than the envelope undershooting extent in the lower mass range. Another change of slope is evident at approximately $M_{ini} \sim 3.50 M_\odot$, where a reduction in f_{env} is necessary to accommodate larger core growth. In this high-mass range, core growth is severely hampered by the combination of high-efficiency TDU and hot bottom burning, significantly limiting core growth during the interpulse phase. However, the white dwarf data spread for $M_{ini} \simeq 3.00 M_\odot$ provides looser constraints on the f_{env}, and I selected an average value of f_{env}.

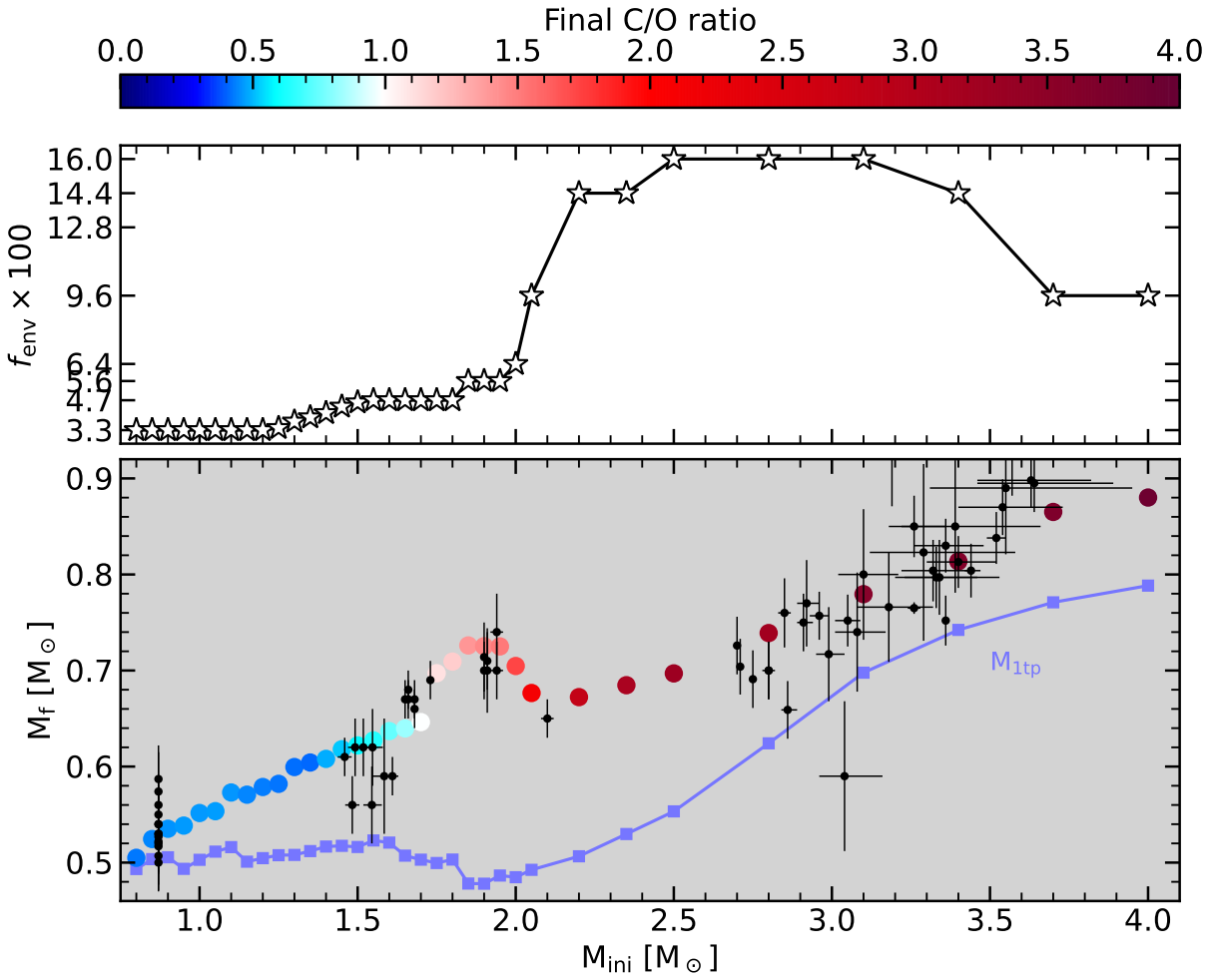

Fig. 4.9: Bottom panel: comparison between the semi-empirical IFMR (points with error bars; Cummings et al., 2018; Marigo et al., 2020), and theoretical predictions of this work (filled circles) color-coded as a function of the final surface C/O. The final mass is reached with `COLIBRI`. The core mass at the first thermal pulse M_{1tp} is plotted for reference. Top panel: the corresponding value of envelope overshooting, multiplied by 100 for clarity.

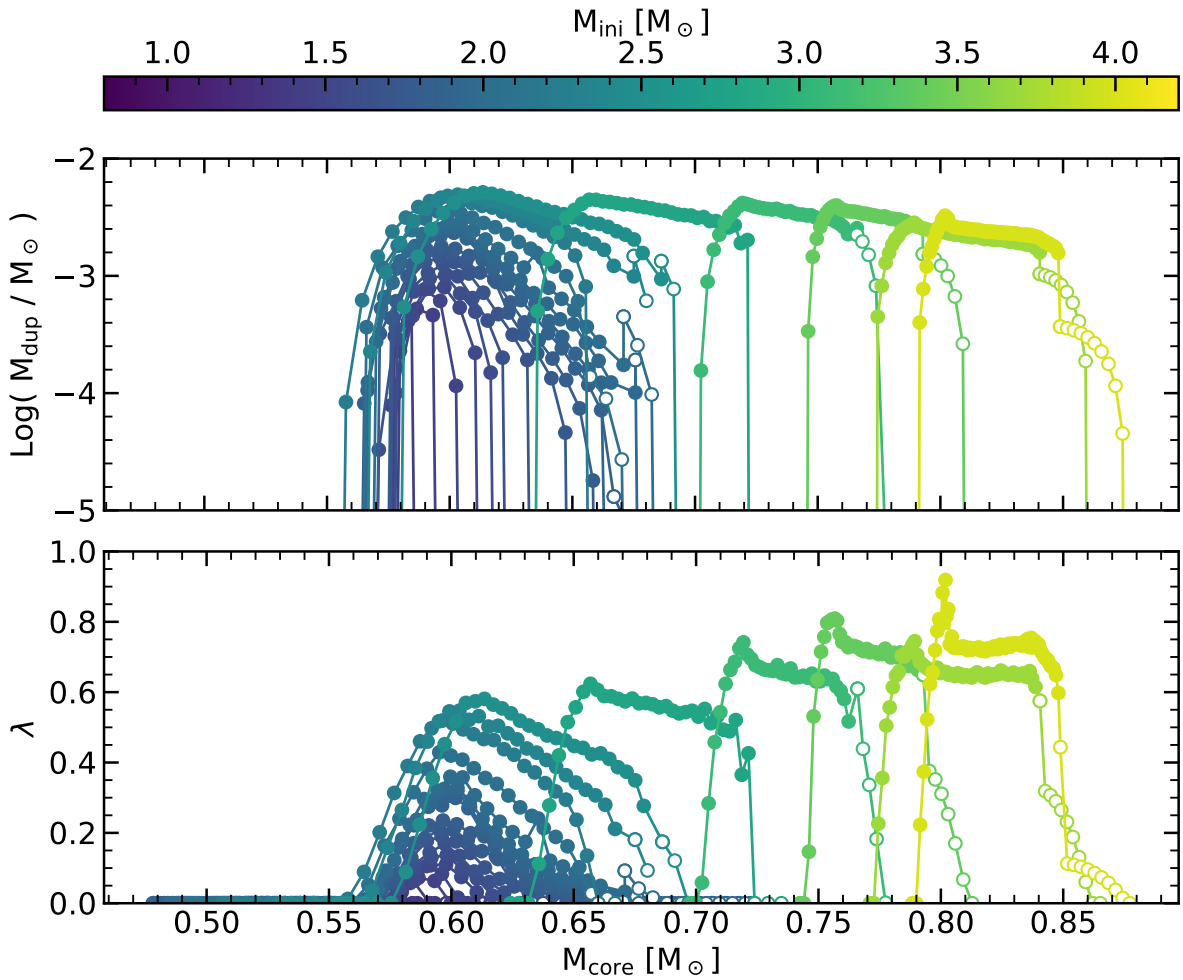

Fig. 4.10: Bottom panel: TDU efficiency versus current core mass for the tracks used in Figure 4.9. PARSEC TDUs are marked by filled circles, COLIBRI TDU are marked with empty circles. Top panel: Log10 of the dredge-up mass versus current core mass for the same tracks and symbols.

$M_{\rm ini}$	$f_{\rm env}$	$N_{\rm TP}$	$N_{\rm EXTRAP}$	$N_{\rm COLIBRI}$	$M_{\rm f,PARSEC}$	$M_{\rm EXTRAP}$	$M_{\rm f,COLIBRI}$	$({\rm C/O})_f$	$\tau_{\rm HB}$	$\tau_{\rm EAGB}$	$\tau_{\rm TPAGB}$	R_2	$\tau_{\rm C}$	$\lambda_{\rm max}$
0.80	0.033	6	0	0	0.503	...	...	0.424	102.510	16.129	1.455	0.172	0.000	0.000
0.85	0.033	6	0	0	0.523	...	...	0.441	111.940	11.547	1.791	0.119	0.000	0.000
0.90	0.033	7	0	0	0.534	...	...	0.455	109.881	11.492	1.963	0.122	0.000	0.000
0.95	0.033	11	0	0	0.538	...	...	0.464	113.405	14.591	2.498	0.151	0.000	0.000
1.00	0.033	10	0	0	0.551	...	...	0.462	108.428	12.715	2.545	0.141	0.000	0.000
1.05	0.033	9	0	0	0.554	...	...	0.468	118.934	9.192	2.070	0.095	0.000	0.000
1.10	0.033	10	0	0	0.573	...	...	0.458	112.987	9.563	2.394	0.106	0.000	0.000
1.15	0.033	14	0	0	0.571	...	...	0.438	109.913	14.758	2.908	0.161	0.000	0.000
1.20	0.033	14	0	0	0.579	...	...	0.428	111.067	13.911	2.952	0.152	0.000	0.000
1.25	0.034	14	0	0	0.582	...	...	0.418	108.358	13.055	2.841	0.147	0.000	0.000
1.30	0.037	17	0	1	0.598	0.598	0.599	0.413	107.687	12.026	3.018	0.140	0.000	0.000
1.35	0.039	16	1	1	0.600	0.605 ± 0.003	0.604	0.406	113.896	10.045	2.935	0.114	0.000	0.000
1.40	0.041	15	2 ± 1	2	0.598	0.610 ± 0.006	0.608	0.487	120.513	8.452	2.786	0.093	0.000	0.063
1.45	0.044	17	1 ± 1	1	0.614	0.619 ± 0.004	0.618	0.520	103.378	11.132	2.914	0.136	0.000	0.072
1.50	0.046	18	2 ± 1	1	0.616	0.623 ± 0.004	0.622	0.581	108.628	10.258	2.972	0.122	0.000	0.106
1.55	0.047	17	2 ± 1	2	0.617	0.630 ± 0.004	0.627	0.641	121.401	7.263	2.782	0.083	0.000	0.110
1.60	0.047	20	0	1	0.635	0.637 ± 0.000	0.637	0.741	113.248	9.355	3.055	0.110	0.000	0.137
1.65	0.047	23	2 ± 1	1	0.634	0.641 ± 0.004	0.640	0.830	129.538	10.010	3.510	0.104	0.000	0.169
1.70	0.047	25	5 ± 3	2	0.638	0.662 ± 0.015	0.646	0.982	117.913	13.553	3.812	0.147	0.000	0.190
1.75	0.047	34	2 ± 1	4	0.679	0.689 ± 0.006	0.697	1.103	129.467	14.204	4.311	0.143	0.657	0.210
1.80	0.047	34	3 ± 2	5	0.684	0.697 ± 0.007	0.709	1.182	159.252	8.776	4.283	0.082	0.789	0.235
1.85	0.056	38	12 ± 6	10	0.672	0.737 ± 0.034	0.726	1.401	267.388	17.313	5.252	0.084	1.014	0.299
1.90	0.056	38	17 ± 9	12	0.662	0.754 ± 0.050	0.725	1.454	234.687	17.506	5.149	0.097	0.890	0.321
1.95	0.056	38	13 ± 7	8	0.676	0.739 ± 0.034	0.725	1.518	240.711	14.036	5.029	0.079	0.975	0.329
2.00	0.064	37	5 ± 1	6	0.671	0.694 ± 0.007	0.705	1.727	195.418	18.703	4.962	0.121	0.925	0.360
2.05	0.096	34	3 ± 1	4	0.657	0.672 ± 0.003	0.677	2.127	193.298	15.462	4.690	0.104	0.939	0.429
2.20	0.144	34	2	2	0.660	0.669 ± 0.002	0.672	2.788	154.412	11.410	4.218	0.101	1.073	0.519
2.35	0.144	34	2	1	0.675	0.683 ± 0.002	0.685	3.130	126.222	8.305	3.476	0.093	1.115	0.547
2.50	0.160	34	3	2	0.686	0.695 ± 0.002	0.697	3.287	95.420	8.453	2.935	0.119	1.193	0.581
2.80	0.160	35	3 ± 1	3	0.724	0.734 ± 0.003	0.739	3.219	63.693	5.019	1.818	0.107	0.905	0.624
3.10	0.160	38	5 ± 2	4	0.766	0.782 ± 0.007	0.779	3.571	43.372	3.239	1.194	0.102	0.663	0.742
3.40	0.144	41	9 ± 3	7	0.793	0.818 ± 0.007	0.814	3.626	29.673	2.559	0.955	0.118	0.583	0.809
3.70	0.096	62	17 ± 3	10	0.841	0.867 ± 0.005	0.865	3.681	23.604	1.559	0.885	0.104	0.563	0.745
4.00	0.096	71	20 ± 4	11	0.849	0.873 ± 0.005	0.880	3.901	17.128	1.360	0.859	0.130	0.584	0.919

Tab. 4.3: Relevant data for the final track set. All tracks have $f_{\rm pdcz} = 0.001$. $N_{\rm TP}$ is the number of pulses calculated by PARSEC. $N_{\rm EXTRAP}$ is the number of pulses with the extrapolation method. $N_{\rm COLIBRI}$ is the number of TPs calculated by COLIBRI. $M_{\rm f,PARSEC}$ is the core mass reached by PARSEC, $M_{\rm f,COLIBRI}$ is the final core mass calculated by continuing the evolution with COLIBRI and $M_{\rm EXTRAP}$ is the core mass reached with the extrapolation. $\tau_{\rm HB}$ is the time spent in the core He-burning phase, $\tau_{\rm EAGB}$ is the time spent in Early AGB, from the central He exhaustion to the beginning of TP-AGB, set when the helium intershell thickness becomes smaller than $0.1 M_\odot$. $\tau_{\rm TPAGB}$ is the time spent in TP-AGB phase and $\tau_{\rm C}$ is the time spent as a C-type star. R_2 ratio is estimated as $(\tau_{\rm EAGB} + \tau_{\rm TPAGB})/\tau_{\rm HB}$. Masses are in solar units and ages in Myr.

Object	Mass fractions				References
	He	C	O	Ne	
PG1707+427	0.52	0.45	0.03	0.0	Werner et al. (2015)
PG1159-035	0.33	0.48	0.17	0.02	Jahn et al. (2007)
PG2131-066	0.73	0.22	0.03	0.0	Werner & Rauch (2014)
PG0122-200	0.73	0.22	0.03	0.0	Werner & Rauch (2014)
PG1424-535	0.52	0.45	0.03	0.01	Werner et al. (2015)
PG1144+005	0.38	0.57	0.016	0.02	Werner et al. (2016)
PG1520+525	0.43	0.38	0.17	0.02	Werner et al. (2016)
MCT0130+1937	0.73	0.22	0.03	0.0	Werner & Rauch (2014)
HS0704+6153	0.56	0.33	0.11	0.0	Dreizler et al. (1994)
HS1517+7403	0.85	0.13	0.02	0.0	Werner & Herwig (2006)
[WC] Abell-78	0.35	0.5	0.15	0.0	Koesterke & Werner (1998)
[WCE] NGC1501	0.5	0.35	0.15	0.0	Werner & Herwig (2006)
RXJ12117.1+3412	0.38	0.54	0.06	0.02	Werner et al. (2005)
NGC246	0.62	0.3	0.06	0.02	Werner et al. (2005)
K1-16	0.33	0.48	0.17	0.02	Werner et al. (2005)
HS2324+397	0.41	0.37	0.01	0.0	Werner et al. (2005)
Longmore4	0.45	0.42	0.11	0.02	Werner et al. (2005)
NGC7094	0.41	0.21	0.01	0.02	Werner et al. (2005)

Tab. 4.4: PG1159 stars and [WC]-type central stars of planetary nebulae surface abundances (in mass fraction units) with references. The typical errors in abundance determination is 0.3-0.5 dex.

Figure 4.10 shows again that PARSEC calculation stops close to the end of TP-AGB, where TDU is quenched. Then, it is clear that both the extrapolation method and COLIBRI have a limited impact on the results. Furthermore, the comparison of $N_{\rm EXTRAP}$ and $M_{\rm EXTRAP}$ with the COLIBRI analogs, retrospectively shows that the extrapolation method is successful in giving a good first-order estimate of the final part of the track. Given all the inherently carried out approximations, it is remarkably good in assigning the correct final core mass, although usually slightly underestimated. Instead, COLIBRI stands out as a very efficient and powerful tool to complete the TP-AGB evolution, where full stellar evolutionary codes usually give up.

Finally, I want to briefly discuss the robustness of the results when giving up the assumption of fixed $f_{\rm pdcz}$. If I let both parameters free, a simple χ^2-fit gives a random distribution of $(f_{\rm env}, f_{\rm pdcz})$, with no clear trend with the initial mass. Still leaving it as an open possibility, it would give little or no information on the internal mixing processes and on the efficiency of the third dredge-up. This is because the parameters not only change the envelope penetration but also the intershell composition, leading to a mild degeneracy of the parameters.

The works by Wagstaff et al. (2020) and Addari (2020) provide valuable insights on how to overcome this apparent degeneracy. The [WC]-type of central stars of planetary nebulae

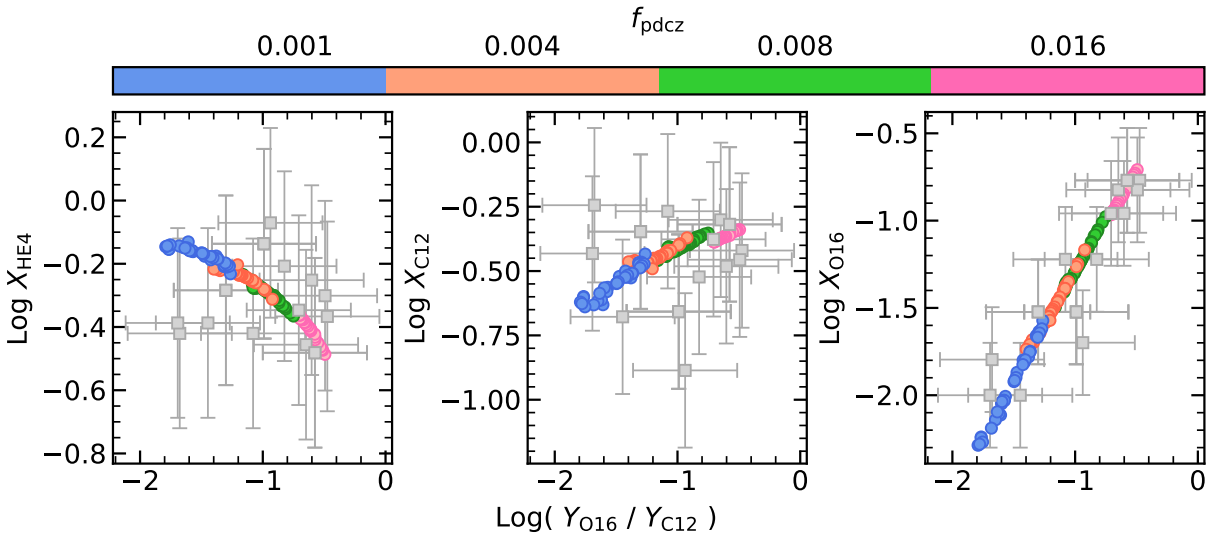

Fig. 4.11: Final intershell composition predicted by our PARSEC (only) models with different f_{pdcz} (colored circles) and abundance determination from Table 4.4 (grey squares with error bar). Neon has not been used as it is poorly determined.

abundances (Table 4.4) is thought to reflect the final intershell composition, giving tighter constraints on the f_{pdcz} only. These findings suggested selecting a single value for f_{pdcz}, and letting only f_{env} vary to adjust the efficiency of TDU. Herwig (2005) and Wagstaff et al. (2020) suggest a much higher PDCZ overshooting $0.004 < f_{pdcz} < 0.016$, compared to $f_{pdcz} = 0.001$ found in this work based on IFMR. Actually, if I naively compare the intershell abundances from our models with higher f_{pdcz} to the observed abundances of PG 1159 stars as in Figure 4.11, I find that f_{pdcz} can be anything between 0.001 and 0.016, consistent with values commonly reported in literature. However, the typical errors for PG 1159 stars abundances determination (about 0.3-0.5 dex, Werner & Herwig 2006; Werner & Rauch 2014; Werner et al. 2016) and the data spread make it difficult to disentangle scenarios with low or zero f_{pdcz}, by relying solely on intershell abundances. Given the difficulties in interpreting observations, primarily due to the potential influence of late thermal pulses, the study of [WC]-type of central stars of planetary nebulae is beyond the scope of this work, but we acknowledge that combining these data with the IFMR can potentially lift the degeneracy of (f_{env}, f_{pdcz}).

4.5 Comments on stellar yields

Our final set of tracks, which are all complete considering PARSEC + COLIBRI evolution, opens up the possibility for calculating stellar yields and ejecta. Even though they are limited to $M_{ini} \leq 4.00 M_{\odot}$ and the two evolutionary codes do not have a full nuclear network, is it at least an exercise worth being done. Stellar yields (or ejecta) are one of the main ingredients in modeling the chemical evolution of galaxies, which is basically due to stars only. Stars pollute their surrounding environment through stellar wind and, eventually, supernovae explosions. The second scenario is out of the scope of this work, as it treats massive stars, and needs careful

explosion models that are calculated with hydrodynamic codes, e.g. (Woosley et al., 2002, KEPLER), (Kifonidis et al., 2003, P-HOTB), (Limongi & Chieffi, 2020, HYPERION). The extreme case involving low- and intermediate-mass stars would be SN Ia, but that is another whole story for another Ph.D. thesis. Then, we limit ourselves in recalling the simple, yet elegant, formalism for calculating yields to which we mainly refer to Portinari et al. (1998). We define the ejecta due to stellar winds as:

$$EJ_{\rm i}(M_{\rm ini}) = \int_0^{\tau_{\rm end}} {\rm d}t \dot{M}(M_{\rm ini}, t) \cdot X_{\rm i}^{\rm surf}(M_{\rm ini}, t) \tag{4.2}$$

where i indicates each element. Eq. 4.2 is just the integral over the total lifetime of the star (from 0 to the end $\tau_{\rm end}$) of the ejected mass, assuming it has the surface composition. In our case, we integrate the wind from the PMS all up to the end of the TP-AGB, roughly when the envelope $M_{\rm env} < 0.01{\rm M}_\odot$, therefore neglecting any possible contribution of the subsequent late thermal pulses or the planetary nebula. The result of the integral then is in mass units, always positive if we consider no accretion, and it depends on the initial mass and metallicity of the star. For this reason, we usually bring up stellar yields $Yd_{\rm i}(M_{\rm ini})$, that quantify the mass fraction of a given element in a star with initial mass $M_{\rm ini}$ that has been newly synthesized and then ejected.

$$EJ_{\rm i}(M_{\rm ini}) = (M_{\rm ini} - M_{\rm f}) \cdot X_{\rm i}(M_{\rm ini}, 0) + M_{\rm ini} \cdot Yd_{\rm i}(M_{\rm ini}) \tag{4.3}$$

Or equivalently, explicating the integral term:

$$Yd_{\rm i}(M_{\rm ini}) = \frac{1}{M_{\rm ini}} \int_0^{\tau_{\rm end}} {\rm d}t \dot{M}(M_{\rm ini}, t) \cdot \left[X_{\rm i}^{\rm surf}(M_{\rm ini}, t) - X_{\rm i}(M_{\rm ini}, 0)\right] \tag{4.4}$$

The yields can be positive or negative, depending if they are produced or consumed from a net point of view. The result of integration is given in the Table 4.5, Table 4.6 for the yields and Table 4.7, Table 4.8 for ejecta.

Here I will briefly comment on the tables, starting from hydrogen, which we can see is always consumed, given its yield is always negative, as it is the first nuclear fuel used by every star, and it is continuously burnt down either in the core or in a shell. On the contrary, helium yield is positive as it is produced by consuming hydrogen, and, most of the time after the main sequence, there is always a source of helium production. About ^{12}C, we can see how for $M_{\rm ini} < 1.55$ M$_\odot$ the yield change from negative to positive sign, meaning that for larger masses ^{12}C is a net product. That is of course due to the contribution of TDU events that bring the product of He-burning on the surface in competition with the carbon burnt, mainly, via the CNO-cyles and converted into ^{14}N. Note that TDU events are also present at slightly lower masses, but they are not yet efficient enough to overcome carbon depletion. Speaking of ^{14}N we can see that it is always produced and its yield increases with $M_{\rm ini}$, which is caused by the increase in the CNO-cyles efficiency at larger initial masses.

A more detailed discussion on the yields and their effects would need to use them in galactic evolutionary models, which was well out of the scope of this thesis and it is a good exercise anyway and, most importantly, a good sanity check of the robustness of our models.

M_{ini}	H	He3	He4	C12	C13	N14	N15	O16	O17	O18
0.800	-8.2691E-03	6.1312E-04	7.6461E-03	-1.0929E-04	2.0179E-05	1.0640E-04	-1.4618E-07	3.7964E-07	2.9398E-08	-2.6802E-07
0.850	-9.1646E-03	5.7441E-04	8.5759E-03	-1.3909E-04	2.1753E-05	1.4014E-04	-1.7154E-07	-1.3982E-07	3.5357E-08	-3.5793E-07
0.900	-9.7935E-03	5.5740E-04	9.2185E-03	-1.6082E-04	2.2561E-05	1.6471E-04	-1.8852E-07	-1.3058E-07	4.2985E-08	-4.4064E-07
0.950	-1.0571E-02	5.6799E-04	9.9833E-03	-1.7607E-04	2.4042E-05	1.8118E-04	-2.0411E-07	-2.4324E-07	3.9905E-08	-4.9289E-07
1.000	-1.1027E-02	5.6925E-04	1.0436E-02	-1.9211E-04	2.4728E-05	1.9979E-04	-2.1730E-07	-8.6191E-07	5.3593E-08	-5.6440E-07
1.050	-8.0255E-03	4.0133E-04	7.6078E-03	-1.4198E-04	1.7793E-05	1.4730E-04	-1.5847E-07	3.3743E-07	4.5268E-08	-4.2523E-07
1.100	-1.2077E-02	5.5928E-04	1.1490E-02	-2.3128E-04	2.6292E-05	2.4387E-04	-2.4877E-07	-7.2162E-07	1.0326E-07	-7.3946E-07
1.150	-9.7182E-03	3.6921E-04	9.3219E-03	-2.1610E-04	2.0889E-05	2.3111E-04	-2.1905E-07	-2.1541E-07	1.7203E-07	-7.5696E-07
1.200	-9.9306E-03	3.4495E-04	9.5550E-03	-2.4028E-04	2.1346E-05	2.5926E-04	-2.3684E-07	-7.8531E-07	2.8889E-07	-8.7611E-07
1.250	-7.7383E-03	2.4984E-04	7.4615E-03	-2.0530E-04	1.6827E-05	2.2296E-04	-1.9757E-07	-6.1505E-07	3.7328E-07	-7.7433E-07
1.300	-1.2657E-02	3.9857E-04	1.2209E-02	-3.6588E-04	2.9348E-05	3.9930E-04	-3.5050E-07	-2.8660E-06	8.3286E-07	-1.3966E-06
1.350	-1.2720E-02	3.8932E-04	1.2271E-02	-3.9357E-04	3.0056E-05	4.3190E-04	-3.7141E-07	-4.2357E-06	1.1391E-06	-1.5272E-06
1.400	-1.3427E-02	3.8335E-04	1.2796E-02	-2.5938E-04	3.0966E-05	4.7298E-04	-3.9926E-07	1.7774E-06	1.5367E-06	-1.7007E-06
1.450	-1.3677E-02	3.6852E-04	1.2960E-02	-2.0151E-04	3.1434E-05	5.0744E-04	-4.2052E-07	2.5365E-06	2.8391E-06	-1.8452E-06
1.500	-1.4803E-02	3.5311E-04	1.3964E-02	-7.6871E-05	3.1683E-05	5.3899E-04	-4.3753E-07	-9.0339E-06	1.4451E-05	-1.9675E-06
1.550	-1.5468E-02	3.3766E-04	1.4438E-02	5.3591E-05	3.2201E-05	5.7964E-04	-4.5760E-07	-2.0538E-05	1.7201E-05	-2.1004E-06
1.600	-1.6394E-02	3.1474E-04	1.5152E-02	2.7681E-04	3.1927E-05	6.1612E-04	-4.6593E-07	-3.7327E-05	1.8138E-05	-2.1844E-06
1.650	-1.8566E-02	2.8576E-04	1.7100E-02	4.7461E-04	3.2554E-05	7.0132E-04	-4.8788E-07	-8.8228E-05	1.6816E-05	-2.3355E-06
1.700	-2.0324E-02	2.7278E-04	1.8459E-02	8.4060E-04	3.2923E-05	7.4558E-04	-5.0188E-07	-1.0062E-04	1.5729E-05	-2.4340E-06
1.750	-2.1124E-02	2.4697E-04	1.9005E-02	1.0971E-03	3.1690E-05	7.5412E-04	-4.8920E-07	-1.1731E-04	1.4227E-05	-2.4016E-06
1.800	-2.2782E-02	2.3623E-04	2.0445E-02	1.3456E-03	3.1982E-05	7.9622E-04	-5.0066E-07	-1.4138E-04	1.3369E-05	-2.4839E-06
1.850	-2.4906E-02	2.2625E-04	2.1879E-02	1.9616E-03	3.1223E-05	8.2321E-04	-5.0395E-07	-1.4472E-04	1.4323E-05	-2.5465E-06
1.900	-2.6303E-02	2.1719E-04	2.3085E-02	2.1386E-03	3.1664E-05	8.6147E-04	-5.1577E-07	-1.6450E-04	1.2306E-05	-2.6222E-06
1.950	-2.8114E-02	2.1007E-04	2.4568E-02	2.3742E-03	3.2460E-05	9.0676E-04	-5.3408E-07	-1.9167E-04	1.2036E-05	-2.7274E-06
2.000	-2.9755E-02	1.9642E-04	2.5667E-02	2.8908E-03	3.1904E-05	9.1577E-04	-5.3205E-07	-1.9933E-04	1.0148E-05	-2.7375E-06
2.050	-3.1644E-02	1.7426E-04	2.6604E-02	3.7902E-03	3.0148E-05	8.8272E-04	-5.1134E-07	-1.8175E-04	8.8618E-06	-2.6521E-06
2.200	-3.5250E-02	1.3681E-04	2.8817E-02	5.1021E-03	2.7911E-05	8.6249E-04	-4.9104E-07	-1.9451E-04	6.3674E-06	-2.5973E-06
2.350	-3.8656E-02	1.1995E-04	3.1434E-02	5.8015E-03	2.8146E-05	9.1215E-04	-5.0878E-07	-2.4370E-04	6.0302E-06	-2.7258E-06
2.500	-5.1516E-02	1.3122E-04	4.1940E-02	7.7345E-03	3.5192E-05	1.1782E-03	-6.4887E-07	-3.7821E-04	6.2052E-06	-3.5018E-06
2.800	-4.4872E-02	8.9426E-05	3.7001E-02	6.3381E-03	3.0663E-05	1.0678E-03	-5.7103E-07	-4.4184E-04	4.3012E-06	-3.0835E-06
3.100	-4.9973E-02	7.8841E-05	4.1150E-02	7.2033E-03	3.3875E-05	1.1999E-03	-6.3384E-07	-5.5829E-04	4.4871E-06	-3.4137E-06
3.400	-5.9143E-02	6.6868E-05	5.0029E-02	7.4366E-03	3.5531E-05	1.3547E-03	-6.7798E-07	-6.7532E-04	3.0452E-06	-3.6605E-06
3.700	-7.0205E-02	5.5473E-05	6.0991E-02	7.5623E-03	3.7427E-05	1.5094E-03	-7.2975E-07	-7.7995E-04	2.6176E-06	-3.9172E-06
4.000	-8.3988E-02	3.8589E-05	7.3726E-02	8.2063E-03	2.3975E-04	1.6987E-03	-1.1849E-06	-8.9229E-04	2.4320E-06	-4.7154E-06

Tab. 4.5: Yields for the elements from Hydrogen to Oxygen-18. The initial mass column is in solar masses. The yields are calculated from the beginning to the end of the track using Eq. 4.4 and remnant mass as in Table 4.3

M_{ini}	Ne20	Ne21	Ne22	Na23	Mg24	Mg25	Mg26	Al26	Al27	Si28
0.800	7.4439E-08	2.3606E-10	-4.5274E-09	1.3385E-08	3.2507E-08	3.7066E-09	4.7899E-09	1.1200E-11	3.4726E-09	3.3643E-08
0.850	9.5355E-08	2.1206E-10	-2.2420E-08	3.5144E-08	3.7460E-08	1.2251E-09	5.8469E-09	2.6800E-09	4.2389E-09	4.1426E-08
0.900	9.5716E-08	1.6213E-10	-2.2487E-08	3.5712E-08	3.8432E-08	1.3409E-09	5.9192E-09	2.6833E-09	4.4464E-09	4.1823E-08
0.950	1.0922E-07	3.3111E-11	-1.6401E-08	3.2180E-08	4.3847E-08	-3.8682E-11	6.3258E-09	4.2701E-09	5.6012E-09	4.5353E-08
1.000	1.0913E-07	-3.4288E-10	-2.9257E-08	5.0854E-08	4.5772E-08	-4.7416E-09	5.3341E-09	8.3310E-09	8.3939E-09	4.8283E-08
1.050	8.3701E-08	2.1962E-10	-3.4905E-09	1.3365E-08	3.3151E-08	3.5501E-09	4.8652E-09	2.4063E-10	3.5960E-09	3.5725E-08
1.100	1.3686E-07	-2.6435E-10	-4.0328E-08	6.5727E-08	4.9815E-08	-2.9314E-09	4.7800E-09	7.1291E-09	1.0278E-08	7.6601E-08
1.150	7.3747E-08	7.8626E-11	-4.3369E-08	5.7224E-08	2.6271E-08	1.0436E-09	4.7671E-09	1.8282E-09	3.9105E-09	4.5193E-08
1.200	5.1735E-08	-1.7444E-10	-9.1442E-08	1.0522E-07	3.0115E-08	-1.4866E-09	3.6341E-09	4.1617E-09	3.2929E-09	4.2154E-08
1.250	5.8766E-08	-1.3777E-10	-1.2408E-07	1.3919E-07	1.9822E-08	-4.9216E-10	3.1780E-09	3.1606E-09	3.5534E-09	2.9604E-08
1.300	7.0644E-08	-1.1242E-09	-3.1423E-07	3.5856E-07	2.6858E-08	-1.4491E-08	4.0157E-11	1.2267E-08	1.3080E-08	4.8050E-08
1.350	7.2912E-08	-1.6993E-09	-4.1284E-07	4.9098E-07	4.3026E-08	-2.4505E-08	-1.0399E-08	1.2562E-08	2.9003E-08	5.5197E-08
1.400	7.0784E-08	-2.7222E-09	6.8767E-06	7.7180E-07	5.4661E-08	-5.4463E-08	-4.7370E-08	1.2022E-08	9.5942E-08	6.3573E-08
1.450	1.6982E-08	-3.7226E-09	1.0646E-05	1.1075E-06	5.8906E-08	-6.9814E-08	-7.0829E-08	3.2665E-08	1.4179E-07	6.4850E-08
1.500	-2.5275E-07	-1.9533E-09	1.6246E-05	2.6158E-06	6.4358E-08	-9.0054E-08	-1.0694E-07	3.6573E-08	2.0775E-07	6.8700E-08
1.550	-3.1768E-07	1.3331E-09	2.4050E-05	3.0737E-06	6.6264E-08	-1.0139E-07	-1.3623E-07	2.9501E-08	2.7305E-07	7.0538E-08
1.600	-3.1661E-07	8.1128E-09	3.5651E-05	3.7362E-06	9.7885E-08	-1.2512E-07	-1.7725E-07	1.1734E-07	3.6436E-07	7.7063E-08
1.650	-4.0620E-07	3.4321E-08	4.7035E-05	4.8357E-06	1.0888E-07	-1.5420E-07	-1.9872E-07	8.4593E-08	4.5224E-07	7.4195E-08
1.700	-4.6270E-07	4.9182E-08	6.7994E-05	5.6988E-06	1.1860E-07	-1.6202E-07	-2.4619E-07	8.9612E-08	5.8864E-07	7.6901E-08
1.750	-4.5985E-07	6.2728E-08	8.3338E-05	6.2074E-06	1.5685E-07	-1.6154E-07	-2.7977E-07	7.0966E-08	6.9865E-07	7.5931E-08
1.800	-4.7781E-07	8.1911E-08	1.0135E-04	6.8670E-06	1.6678E-07	-1.8061E-07	-3.1131E-07	5.1315E-08	8.1206E-07	7.5021E-08
1.850	-9.9009E-07	1.0123E-07	1.4398E-04	8.1456E-06	2.2952E-07	-1.4825E-07	-3.7110E-07	2.5938E-08	1.0152E-06	1.2919E-07
1.900	-1.0274E-06	1.2390E-07	1.5807E-04	8.6063E-06	2.3722E-07	-1.2776E-07	-3.6335E-07	1.3372E-08	1.0837E-06	1.3354E-07
1.950	-1.0685E-06	1.4947E-07	1.7874E-04	9.4631E-06	2.4716E-07	-9.8477E-08	-3.7491E-07	1.6767E-08	1.2028E-06	1.3837E-07
2.000	-1.0419E-06	1.7323E-07	2.2452E-04	1.0023E-05	3.0788E-07	6.5611E-08	-4.0498E-07	4.1572E-08	1.3779E-06	1.3933E-07
2.050	-4.7224E-07	1.9542E-07	3.1527E-04	1.1405E-05	4.0639E-07	2.5106E-07	-4.6809E-07	5.4214E-08	1.6368E-06	1.3365E-07
2.200	8.2938E-08	2.6597E-07	5.0195E-04	1.4753E-05	5.9393E-07	9.6300E-07	-5.0232E-07	1.8490E-07	2.1096E-06	1.7766E-07
2.350	8.2029E-07	3.5249E-07	6.0808E-04	1.6902E-05	7.4586E-07	2.0403E-06	-4.1099E-07	3.0282E-07	2.4625E-06	1.8730E-07
2.500	2.2891E-06	5.5080E-07	8.6025E-04	2.2463E-05	1.0108E-06	4.3414E-06	-3.1888E-07	6.2492E-07	3.4745E-06	2.4384E-07
2.800	2.4265E-06	6.6903E-07	7.2374E-04	1.5869E-05	-4.6831E-07	1.1300E-05	5.9808E-07	5.5097E-07	3.7113E-06	2.5714E-07
3.100	2.5706E-06	1.0044E-06	8.1603E-04	1.5008E-05	-6.0508E-06	3.7587E-05	2.9001E-06	1.1473E-06	6.5518E-06	3.6807E-07
3.400	1.2438E-06	1.6237E-06	8.1336E-04	1.5199E-05	-1.1062E-05	6.3085E-05	5.6818E-06	8.9169E-07	9.6579E-06	5.9246E-07
3.700	-3.4878E-07	2.2366E-06	7.6212E-04	1.6500E-05	-1.3950E-05	8.5584E-05	8.5011E-06	1.0388E-06	1.2651E-05	9.6366E-07
4.000	-6.3322E-07	3.0083E-06	8.6727E-04	1.8703E-05	-1.6107E-05	1.1584E-04	1.1566E-05	1.3046E-06	1.5436E-05	1.3319E-06

Tab. 4.6: Yields for the elements from Neon-20 to Silicon-28. The initial mass column is in solar masses. The yields are calculated from the beginning to the end of the track using Eq. 4.4 and remnant mass as in Table 4.3

M_{ini}	H	He3	He4	C12	C13	N14	N15	O16	O17	O18
0.800	2.0373E-01	4.9779E-04	8.6651E-02	6.5527E-04	2.5143E-05	2.8549E-04	3.7580E-07	1.8175E-03	7.5703E-07	3.8841E-06
0.850	2.2427E-01	4.9629E-04	9.6136E-02	7.0113E-04	2.8419E-05	3.4017E-04	3.9779E-07	2.0047E-03	8.3928E-07	4.2173E-06
0.900	2.5125E-01	5.1067E-04	1.0787E-01	7.7352E-04	3.1433E-05	3.9597E-04	4.3955E-07	2.2467E-03	9.4559E-07	4.6707E-06
0.950	2.8333E-01	5.4976E-04	1.2181E-01	8.6859E-04	3.5392E-05	4.5158E-04	4.9335E-07	2.5343E-03	1.0610E-06	5.2481E-06
1.000	3.0866E-01	5.8033E-04	1.3283E-01	9.3665E-04	3.8407E-05	5.0431E-04	5.3158E-07	2.7610E-03	1.1684E-06	5.6645E-06
1.050	3.4554E-01	4.3366E-04	1.4351E-01	1.1007E-03	3.3828E-05	4.9184E-04	6.6279E-07	3.0583E-03	1.2819E-06	6.4504E-06
1.100	3.6246E-01	6.2823E-04	1.5650E-01	1.0723E-03	4.4998E-05	6.2618E-04	6.0656E-07	3.2454E-03	1.4239E-06	6.5078E-06
1.150	4.0184E-01	4.3891E-04	1.6885E-01	1.2098E-03	4.1694E-05	6.5920E-04	7.1561E-07	3.5679E-03	1.6381E-06	7.1769E-06
1.200	4.3105E-01	4.2929E-04	1.8106E-01	1.2757E-03	4.4568E-05	7.3307E-04	7.5345E-07	3.8259E-03	1.8914E-06	7.5796E-06
1.250	4.6660E-01	3.2881E-04	1.9167E-01	1.4250E-03	4.1412E-05	7.3238E-04	8.6873E-07	4.1138E-03	2.1275E-06	8.3120E-06
1.300	4.8299E-01	5.3544E-04	2.0709E-01	1.2878E-03	5.9522E-05	9.9485E-04	7.1433E-07	4.3111E-03	2.8244E-06	7.9159E-06
1.350	5.1455E-01	5.4400E-04	2.2014E-01	1.3461E-03	6.3326E-05	1.0896E-03	7.4418E-07	4.5879E-03	3.3920E-06	8.2986E-06
1.400	5.4587E-01	5.5626E-04	2.3411E-01	1.6306E-03	6.7512E-05	1.2000E-03	7.6379E-07	4.8808E-03	4.1205E-06	8.6213E-06
1.450	5.7336E-01	5.5491E-04	2.4591E-01	1.8023E-03	7.0960E-05	1.3008E-03	7.7982E-07	5.1284E-03	6.1852E-06	8.8825E-06
1.500	6.0381E-01	5.5136E-04	2.6063E-01	2.0951E-03	7.4310E-05	1.4048E-03	8.1018E-07	5.3947E-03	2.3860E-05	9.2465E-06
1.550	6.3399E-01	5.4617E-04	2.7429E-01	2.4062E-03	7.8063E-05	1.5252E-03	8.3205E-07	5.6525E-03	2.8956E-05	9.5646E-06
1.600	6.6044E-01	5.2738E-04	2.8715E-01	2.8674E-03	8.0464E-05	1.6399E-03	8.6308E-07	5.8726E-03	3.1415E-05	9.8845E-06
1.650	6.8971E-01	4.9646E-04	3.0401E-01	3.3265E-03	8.4534E-05	1.8433E-03	8.8245E-07	6.0776E-03	3.0258E-05	1.0182E-05
1.700	7.1674E-01	4.8976E-04	3.1902E-01	4.0817E-03	8.8115E-05	1.9831E-03	9.0673E-07	6.3195E-03	2.9358E-05	1.0501E-05
1.750	7.1369E-01	4.5822E-04	3.2066E-01	4.5704E-03	8.7574E-05	2.0348E-03	9.0234E-07	6.2798E-03	2.7514E-05	1.0423E-05
1.800	7.3664E-01	4.5216E-04	3.3454E-01	5.1678E-03	9.0840E-05	2.1740E-03	9.2050E-07	6.4638E-03	2.6777E-05	1.0681E-05
1.850	7.5525E-01	4.4633E-04	3.4728E-01	6.4584E-03	9.2049E-05	2.2863E-03	9.4484E-07	6.6551E-03	2.9293E-05	1.0902E-05
1.900	7.8758E-01	4.4169E-04	3.6453E-01	7.0207E-03	9.5998E-05	2.4346E-03	9.8207E-07	6.9233E-03	2.6302E-05	1.1337E-05
1.950	8.1847E-01	4.3989E-04	3.8226E-01	7.7132E-03	1.0066E-04	2.6001E-03	1.0043E-06	7.1708E-03	2.6515E-05	1.1697E-05
2.000	8.6398E-01	4.2484E-04	4.0491E-01	9.0423E-03	1.0332E-04	2.7112E-03	1.0992E-06	7.5796E-03	2.3516E-05	1.2519E-05
2.050	9.1434E-01	3.9115E-04	4.2944E-01	1.1227E-02	1.0370E-04	2.7423E-03	1.2456E-06	8.0870E-03	2.1581E-05	1.3643E-05
2.200	1.0117E+00	3.3873E-04	4.8042E-01	1.5070E-02	1.0801E-04	2.9350E-03	1.4713E-06	8.9821E-03	1.7807E-05	1.5509E-05
2.350	1.0965E+00	3.2302E-04	5.2846E-01	1.7826E-02	1.1694E-04	3.2746E-03	1.5858E-06	9.6849E-03	1.8311E-05	1.6729E-05
2.500	1.1567E+00	3.7260E-04	5.9704E-01	2.3875E-02	1.4298E-04	4.1701E-03	1.3893E-06	1.0160E-02	1.9996E-05	1.6294E-05
2.800	1.3438E+00	3.0131E-04	6.6621E-01	2.2935E-02	1.4873E-04	4.3895E-03	1.8434E-06	1.1458E-02	1.7168E-05	1.9998E-05
3.100	1.4996E+00	3.0173E-04	7.6100E-01	2.8172E-02	1.7580E-04	5.2956E-03	1.9108E-06	1.2563E-02	1.9680E-05	2.1654E-05
3.400	1.6429E+00	2.9125E-04	8.7609E-01	3.1795E-02	1.9970E-04	6.3624E-03	2.0145E-06	1.3634E-02	1.6784E-05	2.3484E-05
3.700	1.7614E+00	2.7528E-04	9.9951E-01	3.5117E-02	2.2496E-04	7.5101E-03	2.0347E-06	1.4576E-02	1.6733E-05	2.4889E-05
4.000	1.8884E+00	2.3143E-04	1.1465E+00	4.0679E-02	1.0542E-03	8.9138E-03	4.7125E-07	1.5648E-02	1.7485E-05	2.4480E-05

Tab. 4.7: Ejecta for the elements from Hydrogen to Oxygen-18. The initial mass column is in solar masses. The ejecta are calculated from the beginning to the end of the track using Eq. 4.2 and remnant mass as in Table 4.3

M_{ini}	Ne20	Ne21	Ne22	Na23	Mg24	Mg25	Mg26	Al26	Al27	Si28
0.800	3.8590E-04	9.7135E-07	3.1204E-05	9.7380E-06	1.4264E-04	1.8809E-05	2.1538E-05	8.9598E-12	1.5765E-05	1.9724E-04
0.850	4.2574E-04	1.0716E-06	3.4410E-05	1.0761E-05	1.5736E-04	2.0749E-05	2.3762E-05	2.2780E-09	1.7393E-05	2.1761E-04
0.900	4.7713E-04	1.2009E-06	3.8564E-05	1.2059E-05	1.7636E-04	2.3253E-05	2.6630E-05	2.4150E-09	1.9492E-05	2.4387E-04
0.950	5.3824E-04	1.3545E-06	4.3511E-05	1.3598E-05	1.9894E-04	2.6230E-05	3.0040E-05	4.0566E-09	2.1990E-05	2.7511E-04
1.000	5.8651E-04	1.4756E-06	4.7400E-05	1.4834E-05	2.1679E-04	2.8577E-05	3.2733E-05	8.3310E-09	2.3964E-05	2.9978E-04
1.050	6.4937E-04	1.6345E-06	5.2512E-05	1.6383E-05	2.4002E-04	3.1651E-05	3.6242E-05	2.5267E-10	2.6529E-05	3.3191E-04
1.100	6.8938E-04	1.7345E-06	5.5703E-05	1.7448E-05	2.5480E-04	3.3591E-05	3.8472E-05	7.8420E-09	2.8168E-05	3.5238E-04
1.150	7.5768E-04	1.9070E-06	6.1227E-05	1.9165E-05	2.8005E-04	3.6928E-05	4.2288E-05	2.1024E-09	3.0954E-05	3.8729E-04
1.200	8.1259E-04	2.0449E-06	6.5610E-05	2.0611E-05	3.0036E-04	3.9602E-05	4.5353E-05	4.9940E-09	3.3198E-05	4.1536E-04
1.250	8.7370E-04	2.1988E-06	7.0506E-05	2.2199E-05	3.2293E-04	4.2582E-05	4.8762E-05	3.9508E-09	3.5694E-05	4.4658E-04
1.300	9.1623E-04	2.3045E-06	7.3692E-05	2.3563E-05	3.3865E-04	4.4636E-05	5.1131E-05	1.5948E-08	3.7444E-05	4.6834E-04
1.350	9.7543E-04	2.4526E-06	7.8330E-05	2.5252E-05	3.6055E-04	4.7507E-05	5.4421E-05	1.6959E-08	3.9884E-05	4.9860E-04
1.400	1.0359E-03	2.6032E-06	9.3403E-05	2.7193E-05	3.8291E-04	5.0409E-05	5.7741E-05	1.6831E-08	4.2448E-05	5.2951E-04
1.450	1.0881E-03	2.7334E-06	1.0345E-04	2.9038E-05	4.0226E-04	5.2935E-05	6.0625E-05	4.7364E-08	4.4657E-05	5.5626E-04
1.500	1.1479E-03	2.8874E-06	1.1725E-04	3.2874E-05	4.2452E-04	5.5836E-05	6.3928E-05	5.4859E-08	4.7223E-05	5.8704E-04
1.550	1.2064E-03	3.0399E-06	1.3490E-04	3.5192E-05	4.4619E-04	5.8670E-05	6.7148E-05	4.5727E-08	4.9729E-05	6.1701E-04
1.600	1.2591E-03	3.1833E-06	1.5892E-04	3.7733E-05	4.6571E-04	6.1193E-05	7.0014E-05	1.8774E-07	5.2039E-05	6.4393E-04
1.650	1.3207E-03	3.3824E-06	1.8448E-04	4.1291E-05	4.8856E-04	6.4150E-05	7.3418E-05	1.3958E-07	5.4726E-05	6.7550E-04
1.700	1.3773E-03	3.5523E-06	2.2705E-04	4.4431E-05	5.0956E-04	6.6895E-05	7.6495E-05	1.5234E-07	5.7299E-05	7.0452E-04
1.750	1.3761E-03	3.5755E-06	2.5721E-04	4.5576E-05	5.0920E-04	6.6831E-05	7.6359E-05	1.2419E-07	5.7474E-05	7.0393E-04
1.800	1.4256E-03	3.7378E-06	2.9780E-04	4.8323E-05	5.2753E-04	6.9203E-05	7.9052E-05	9.2366E-08	5.9736E-05	7.2925E-04
1.850	1.4680E-03	3.8870E-06	3.8525E-04	5.2126E-05	5.4371E-04	7.1370E-05	8.1349E-05	4.7986E-08	6.1926E-05	7.5155E-04
1.900	1.5344E-03	4.1024E-06	4.2460E-04	5.5084E-05	5.6830E-04	7.4641E-05	8.5055E-05	2.5407E-08	6.4822E-05	7.8553E-04
1.950	1.5998E-03	4.3234E-06	4.7810E-04	5.8838E-05	5.9256E-04	7.7887E-05	8.8673E-05	3.2695E-08	6.7787E-05	8.1905E-04
2.000	1.6919E-03	4.6102E-06	5.8606E-04	6.2752E-05	6.2673E-04	8.2699E-05	9.3733E-05	8.3143E-08	7.1959E-05	8.6613E-04
2.050	1.7952E-03	4.9216E-06	7.9159E-04	6.8664E-05	6.6472E-04	8.8064E-05	9.9288E-05	1.1114E-07	7.6734E-05	9.1836E-04
2.200	1.9981E-03	5.6140E-06	1.2659E-03	8.2827E-05	7.3978E-04	9.9503E-05	1.1040E-04	4.0677E-07	8.6263E-05	1.0216E-03
2.350	2.1799E-03	6.3102E-06	1.6052E-03	9.4628E-05	8.0674E-04	1.1095E-04	1.2059E-04	7.1162E-07	9.4761E-05	1.1137E-03
2.500	2.3638E-03	7.3123E-06	2.3414E-03	1.1561E-04	8.7409E-04	1.2579E-04	1.3081E-04	1.5623E-06	1.0502E-04	1.2059E-03
2.800	2.7022E-03	8.6578E-06	2.2445E-03	1.1239E-04	9.9496E-04	1.6302E-04	1.5211E-04	1.5427E-06	1.2051E-04	1.3785E-03
3.100	3.0428E-03	1.0752E-05	2.7752E-03	1.2303E-04	1.1029E-03	2.6444E-04	1.7837E-04	3.5565E-06	1.4429E-04	1.5523E-03
3.400	3.3866E-03	1.4034E-05	3.0390E-03	1.3695E-04	1.2126E-03	3.7936E-04	2.0810E-04	3.0317E-06	1.7102E-04	1.7309E-03
3.700	3.7062E-03	1.7607E-05	3.1197E-03	1.5452E-04	1.3187E-03	4.9737E-04	2.3837E-04	3.8436E-06	1.9827E-04	1.8986E-03
4.000	4.0777E-03	2.2303E-05	3.7991E-03	1.7768E-04	1.4437E-03	6.6225E-04	2.7399E-04	5.2186E-06	2.2843E-04	2.0909E-03

Tab. 4.8: Ejecta for the elements from Neon-20 to Silicon-28. The initial mass column is in solar masses. The ejecta are calculated from the beginning to the end of the track using Eq. 4.2 and remnant mass as in Table 4.3

Concluding remarks

In few words, this Ph.D. thesis presented a theorist's journey and point of view on the Initial-Final Mass Relation, from models to the interpretation of the observations. In practice, this is a very crude summary and it would not give it justice.

After a much-needed introduction in Chapter 1 on the very basics of stellar structure and evolution, which sets the vocabulary and a common ground knowledge, I have spent much effort into analyzing our stellar evolution code PARSEC in the context of producing good quality TP-AGB models. This objective does indeed need a deep understanding of the backstage of any stellar evolution code, built in Chapter 1, which goes from deriving and analyzing the meaning of the equations and prescriptions to the choice of updated and accurate input physics. This discussion gave me the possibility of presenting a detailed and updated description of PARSEC. Having settled these solid foundations, In Chapter 3 I presented the most important and recent implementations of the PARSEC code for computing the TP-AGB evolution. In particular, I introduced new sets of opacity tables to include the tracking of abundance variation of Carbon, Nitrogen, and Oxygen. I showed that this is crucial to retrieve more accurate estimates of the opacity, especially in the stellar outer envelope which conditions directly affect the magnitude and the driving mechanism of the stellar wind. Then I developed and implemented a new shell-shifting method that simultaneously ensures energy is conserved in time and allows to considerably decrease the computation time of TP-AGB tracks by about 4 times. The time and resource optimization was fundamental to allow an exhaustive exploration of the parameter space of interest, namely the efficiency of overshooting at the bottom of the convective envelope and at the borders of the pulse-driven convective zone. The effects of overshooting coupled with mass-loss on the shape of the IFMR were studied in detail in the recently published paper Addari et al. (2024), which is the base of Chapter 4 where, along with the analysis of the evolutionary features of our sets of models at $0.8 \leq M_{\rm ini}/{\rm M}_{\odot} \leq 4$, we concluded that the efficiency of the extra mixing at the bottom of the convective envelope cannot be kept constant with the initial mass without failing in reproducing the IFMR kink at $M_{\rm ini} \sim 1.65 - 2.10$ M$_{\odot}$. The overshooting has to increase with $M_{\rm ini}$ by a factor of $\sim 4 - 5$, reaching values comparable with

those needed for the extended blue loops in massive stars (Tang et al., 2014). Still, we noticed a mild degeneracy between the two overshooting parameters, which we overcame by keeping the one at the pulse-driven convective zone constant, meaning that more information is needed to couple with the IFMR and arrive at a conclusive result. The possibility of including abundances of PG 1159 stars and [WC]-type of central stars of planetary nebulae has been briefly discussed, but the possibility of (very) late thermal pulse events complicate the picture enough not to allow a definitive interpretation and constraint on the overshooting parameter in the pulse-driven convective zone. Finally, we confirmed the interpretation of the kink in the IFMR (Marigo et al., 2020), as originated by the carbon enrichment of recurrent dredge-up event, affecting the power of stellar wind and therefore prolonging the duration of the TP-AGB phase for those stars that do not form enough carbon dust in their atmospheres.

This work wants to stand as evidence of the information on the basic parameters of stellar models we can gather from the IFMR, and as a practical guideline on how to calibrate those structural parameters on this fundamental relation. Future works building on our findings will investigate the IFMR at larger masses, where hot bottom burning is present and where Marigo (2022) hinted at the presence of a second kink. Then, we plan to extend our set of complete TP-AGB models at lower metallicity, and something I have not discussed here, but we keep it in mind, is to explore also the uncertainty in the $^{12}C(\alpha,\gamma)^{16}O$ reaction as it might influence the composition of the intershell. Even more to the future, we would like to include a larger network of elements and nuclear reactions, studying also the nucleosynthetic possibilities offered by AGB stars, such as s-process nucleosynthesis.

APPENDIX A

PyPARSEC: A Python package for PARSEC utilities

In this Chapter, I present the main tool I started developing at the beginning of this Ph.D. project. The Python module `PyPARSEC` contains routines for efficient reading and storage of the stellar evolution tracks, automated analysis of the TP-AGB phase and its extrapolation (see Section 3.3), yields calculation, detailed Kippenhahn diagrams and a wrapper to start `PARSEC` tracks and sets in a Python framework.

Packages required: `NumPy` (Harris et al., 2020), `matplotlib` (Hunter, 2007), `SciPy` (Virtanen et al., 2020).

A.1 PARSEC output files

Before going into the technical details of `PyPARSEC`, a primer on what and how `PARSEC` output provides during the runs is needed. We can divide the files into two types: history and structure files. The main history files are:

`F7` : contains all the star's most important properties for each model, such as age, mass, luminosity, effective temperature, etc... There are two types of this file, one in text form and another in binary format. In the first there is also information about the input parameters of the track, and a limited sub-sample of properties (= columns) is present. In the binary (or unformatted) version there are all the columns for each stellar model.

`F4` : similar to `F7` but has three records for each stellar model. For the chemical composition, the three records respectively refer to the surface, the bottom of the hydrogen-burning shell (if present), and the center. In addition, more properties of interest of the TP-AGB are saved here, such as the temperature at the bottom of the convective envelope, and at the top, middle, and bottom of the He-intershell.

History files are printed after completing each stellar model, which is not the case for structure files and the user has to choose the saving frequency, to avoid filling up the memory. The structure files are:

F11 : A binary file containing fundamental structural profiles, is mainly used to restart a track from a specific model. Only the mass shells below the fitting point are present, therefore the atmosphere is not saved. The four structure variables (see Section 2.2) are saved with all the chemical composition and additional profiles such as energy produced, reaction rates, residuals of the structure equations, etc... All the structures are printed into the same file.

J0 : A text file containing a single structure at a specific model, therefore there are as many J0 files as given by the user-defined frequency. The structures are complete from the center to the atmosphere. The saved quantities are similar to the F11 file but with the intention to be used as output (i.e. in proper units) and in general with much more information.

The four files presented above are those to look at when we want to extract the information out of the PARSEC calculations, but there are more. Briefly, we have the F3 file dedicated to solar calibration, F6 and F9 files that can help with understanding divergences and bugs, FAGB file saves important properties to check when using the shell-shifting module (Section 3.2) and finally F81 file collects the structure profiles at every stellar model resampled down to about 100 meshpoints.

A.2 Current status of PyPARSEC

At the time of writing, the package is structured as in Figure A.1. Not all the modules, classes, and functions are mentioned here in this work, I prefer to keep it concise and report only the most used tools, for simplicity. In Figure A.1 the modules are shown in alphabetic order, however, `readfiles.py` is the one that is really independent of all the others. That is, all the most important modules have to import, at least, the `Track` class with the `Read` method so I start to describe how PyPARSEC reads the files.

`readfiles.py`: There are two fundamental classes: `Track` and `Structure`. The first one stores, as attributes, all the previously cited PARSEC files after reading. The two structure files, F11 and J0, are saved into lists of objects of the `Structure` class. The `Structure` class clearly stores the structure as one of its attributes but also keeps track of some global properties, such as the model number, age, luminosity, mass, etc... The text files are read as structured NumPy arrays so that every column is identified with the same column name as in the PARSEC output files. Something to point out here is the reading speed: I could have used some NumPy function (e.g. `numpy.genfromtxt`). That is very efficient when dealing with relatively small files, however, TP-AGB history files have typically an order of 10^5 lines, which leads us to write custom read functions. The unformatted FORTRAN files are trickier to deal with. I made use of the SciPy package, with the function `scipy.io.FortranFile` which can read our binary files.

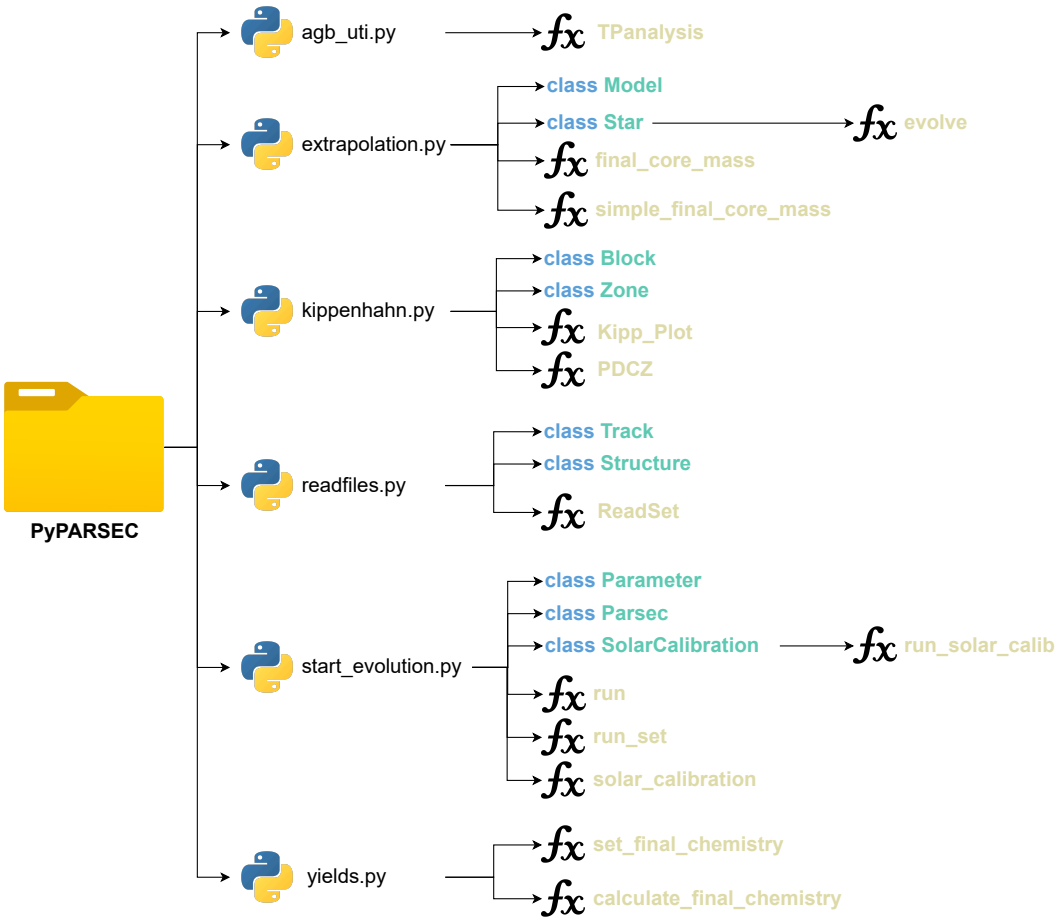

Fig. A.1: PyPARSEC package structure. Here I report the most used modules, classes, and functions. There are a few more utility modules, but I prefer to skip them for the sake of simplicity. The same approach is intended for the mentioned class, methods and functions.

Here one has to know precisely the type of variables in each record, otherwise `TypeErrors` or `ValueErrors` can easily occur. For both kinds of files, while reading them, it is important to save the temporary rows, before converting them to `NumPy` arrays, as `tuple` and not `list`, because the latter takes so much more memory as they have no limited size. I noted that this simple precaution made our reading method improve speed by a factor of 100.

Once every file has been read, the `Track` object is saved to a `pickle` file, which is in binary form, as it is much faster to read it again if needed. This is especially useful when dealing with long calculations, such as the ones for the TP-AGB phase. As the typical time of the PARSEC execution, for TP-AGBs, is $\sim$ 100 hr we might want to read the files in the middle of the calculation. To improve efficiency, our module checks if the evolution has progressed from the last model, and only reads from that point onwards, exploiting the already read part saved into the previous `pickle` file. With the same logic, the reading module handles eventual track restarts, grouping correctly the restarted and original PARSEC files.

From the user point of view, all that has been described above is done in the background:

when a new object of the class Track is defined, just by giving it the filename of the unformatted F7, all the files corresponding to that run are read. Instead, by giving a list of filenames or a regular expression to the function ReadSet, the set identified by that will be read all at once.

As a benchmark, a total of ∼ 4.5 GB of data of a single TP-AGB track is read in 35 seconds on the same Intel Xeon Gold 6238R CPU @ 2.20GHz cited before, and it is compacted into a ∼ 1.5 GB binary file. In particular, the unformatted F7 (accounting for 265MB and about 300k models) is read in 7 seconds, the F4 file is read in 21 seconds (good sanity check, since it has three records per model) and, interestingly, the binary structure file F11 is read in 4 seconds, even though it is the heavier file with 3.5 GB. However, this can be explained as a smaller number of cycles are needed to read the F11 compared to the F7.

start_evolution.py: The evolution module offers a Python based interface to run PARSEC tracks and sets. It has two base classes, Parameter and Parsec: the first one saves every input parameter name with its value and contains methods to check if two parameters are equal or not. It is the basis for the Parsec class, which saves a list of Parameter objects (the code inputs) and methods to generate automatically the name of the various output files, modify the value of parameters, write the correct command line to start the evolution.

The Parsec object is then fed to the run or run_set functions: the first one simply runs the given track, as dictated by the input, the second instead allows to input a dictionary containing the parameters and values to explore in the set of tracks. This latter function has also the option to send different tracks to run in parallel, with a user-defined number of CPUs. This module allows great flexibility and possibilities to implement new methods to deal with particular cases, such as the automatic restart or diagnosis of stopped calculations, the generation of Zero Age Horizontal Branch files (needed to evolve stars after the He-flash).

Recently, I have added a first implementation of automated solar calibration, by exploiting the scipy.interpolate.leastsq method, which tried to minimize the sum of squared errors. The class SolarCalibration is a wrapper to construct the initial stage of calibration and function solar_calibration offers a user interface for effectively running the calibration. Ideally, the user can give an undefined number of parameters to calibrate (with the same PARSEC format) on top of the initial metallicity and helium content and an undefined number of target values (to be chosen from the F3 output file). The leastsq method does not randomly search for the best parameters, nor does it span the parameter space blindly. Instead, it tries to estimate the Jacobian function to predict the direction in which the sum of squares decreases. However, this prevents parallelization of the single tracks needed to run the calibration. For this reason, I am planning to add different methods for solar calibration, in a fully pythonic framework. This shows how important is to modernize the approach and our codes to exploit well-known and fully working methods, allowing us to focus on the results.

kippenhahn.py: As the name suggests, this module deals with the generation of Kippenhahn diagrams. The user interface is provided by Kipp_Plot function, which has many parameters to optimize the visualization. The definition of convective and burning zones is completely automatic and it is optimize to minimize the eventual numerical artifacts that may

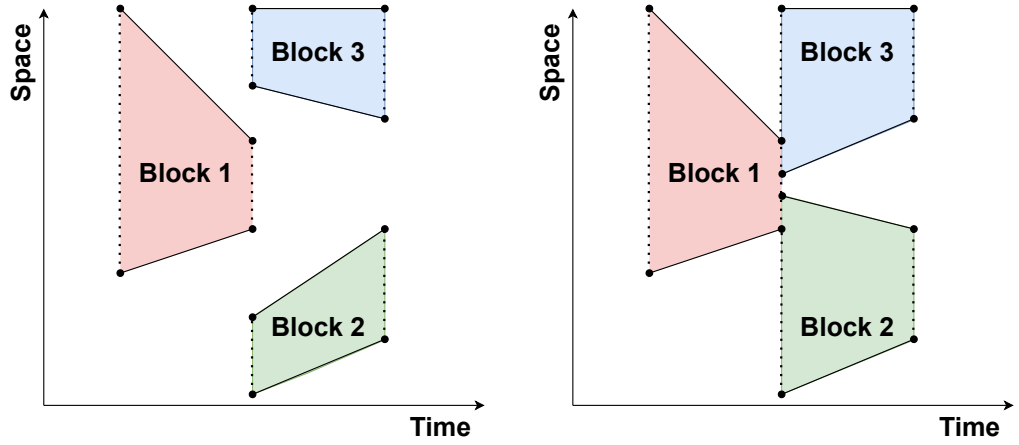

Fig. A.2: The four cases for considering merging between `Blocks` when they are adjacent (if not, they cannot be merged). By definition, two adjacent blocks can only intersect in the time coordinate. The left panel visually shows the two cases in which the block cannot be merged, and the right panel shows the two in which the block will be merged in a `Zone`. The time axis can be the model number or age, in any unit. The space axis can be the mass or radial coordinate.

happen simply utilizing the borders of convective regions from the `PARSEC` output. Instead, it deals with the problem of identifying the various convective regions as a whole, both in time (age or model number) and in space (mass or radius). To do so, I introduce two base classes: `Block` and `Zone`. The first is simply defined by four numbers, which are the minimum and maximum in the time ($x_{\rm min}$ and $x_{\rm max}$) and space axis ($y_{\rm min}$ $y_{\rm max}$), identifying the four vertices ($x_{\rm min}$, $y_{\rm min}$), ($x_{\rm max}$, $y_{\rm min}$), ($x_{\rm max}$, $y_{\rm max}$) and ($x_{\rm min}$, $y_{\rm max}$). The `Block` object has a method to check the intersection with another time-adjacent `Block` object, within a user-defined tolerance, as shown in Figure A.2. The `Zone` class instead collects all the blocks and merges them into a `matplotlib` Polygon if they are intersecting and generates new Polygons as needed if the zones are not contiguous. This method has been motivated by the need to identify the pulse-driven convective zones and by how `PARSEC` saves the convective borders. The instability regions are identified by their top and bottom border, and they are printed in the `F7` ordered by their width. Therefore, if the track has more than one convective region simultaneously and their relative width change, the order in the output might be swapped during the evolution. Instead, burning regions are defined by their fuel, hydrogen, helium, and carbon, therefore they are uniquely identified and a simple `fill_between` method (again from `matplotlib`) can be used to draw them in the Kippenhahn diagram.

The other important method implemented in this module is the `PDCZ` function. It utilizes the same function to generate the convective regions as `Kipp_Plot`, without plotting them, but storing the Polygons to analyze them. First, it has a series of filters to assess whether or not they are real PDCZs or small spurious regions that might happen during the calculation. Once all the PDCZ are identified, this is also compared with the number of pulses found by another function, described later in the `agb_uti.py` module, and this serves as a sanity check

that both functions are identifying the same number of thermal pulses. Moreover, Polygons are extremely convenient for extracting information such as the maximum extension, time duration, time of growth, and decay of the PDCZ, which can help in characterizing the model. Finally, this method allows to know when the PDCZ vanishes to identify the structure from which I can safely extract the intershell composition, just after the pulse and before any pollution from the TDU.

agb_uti.py: This module has many methods that are of interest in characterizing the TP-AGB phase, which is all called with the function `TPanalysis` that takes a `Track` object and tries to extract information about every thermal pulse.

The first task is to find the thermal pulses, which seems easy but the real complication is filtering out the "relaxation pulses" that might occur after the main flash event. The same issue might be present with the PDCZs corresponding to the pulses. These spurious pulses and PDCZs occur mainly during the first thermal pulses, which are often referred to as not in "full-power". To do so, I use the function `scipy.signal.find_peaks` on the Helium luminosity column, with thresholds on the prominence and the minimum height, which must be larger than the Hydrogen luminosity. This method already finds almost only the main thermal pulses, but to avoid including some secondary ones, I also filter with the average interpulse time $\langle \tau_{\text{int}} \rangle$. I calculate it and if two pulses are closer than 10% of $\langle \tau_{\text{int}} \rangle$ I drop the less luminous ones. Finally, in very few cases this is not enough, and we compare the number of pulses to the number of found PDCZ (with the `PDCZ` function described previously) and I drop the last secondary pulses that might have sneaked through the first two filters. Figure A.3 shows an example of a TP-AGB track after passing through all the filters.

After this three-step filter procedure, I can reliably calculate all the necessary information about the TP-AGB: the module prints a summary table with many quantities per thermal pulse, such as dredge-up efficiency, core growth, relevant mass coordinates, temperature at the bottom of the convective envelope, intershell composition after PDCZ extinction and, conservation of energy and much more.

extrapolation.py: The extrapolation scheme has been extensively described in Section 3.3. Here I can translate the workflow by citing the most important classes and functions implemented in `PyPARSEC`. The extrapolation model, equal for all the simulations, is initialized by creating an object of the `Model` class, which immediately analyzed the previous `PARSEC` track by finding fitting and shaping functions and preparing the λ model with uniform or gaussian probability, depending of the user input. Then, a simulation is initialized by an instance of the `Star` class, which takes the `PARSEC` track and the `Model` object, adjusting it at the last thermal pulse. The extrapolation is carried out by calling the method `Star.evolve`, which also prints the output to a text file with all the timesteps and pulse cycles. This pipeline is contained inside the function `final_core_mass`, which at the end of all simulations, does a quick statistical analysis offering mean, and standard deviation and removes eventual outliers. If the pipeline cannot find a satisfying result, e.g. when too many extrapolation instances fail, the function calls `simple_final_core_mass` which estimates the final mass as Eq. 6 of (Siess, 2007).

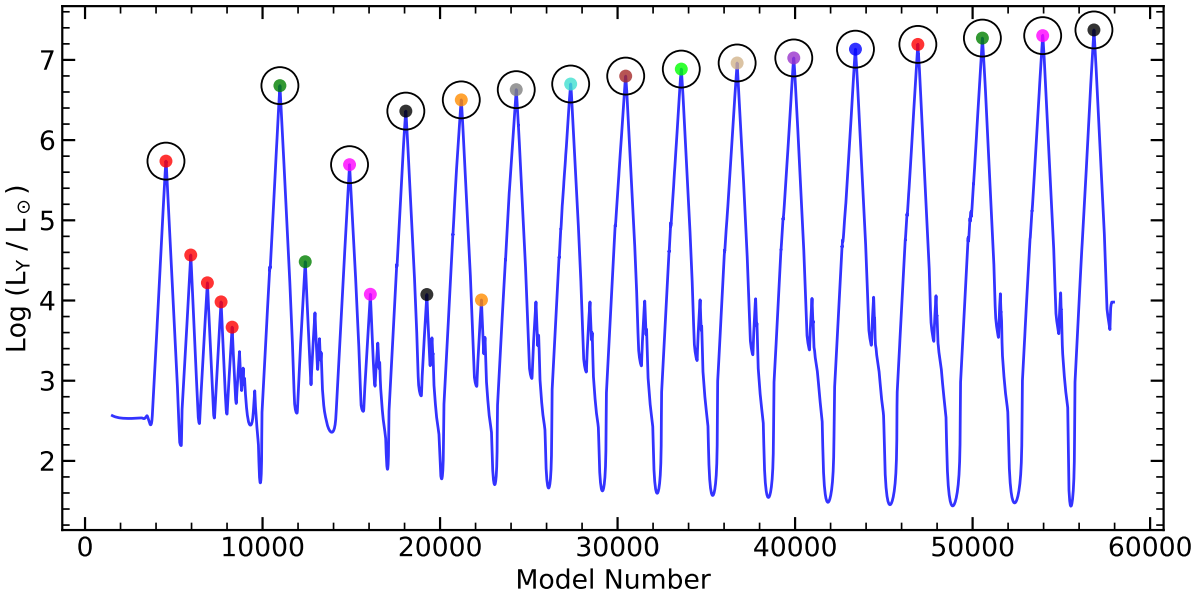

Fig. A.3: Example of application of the thermal pulse finder routine. I plot the Helium luminosity with the Model number as they are more concentrated in the thermal pulse stages. The colored circles are the detected thermal pulses only applying the `scipy.signal.find_peaks` functions, while the circles one have been selected at the end of the filter procedure.

`yields.py`: This module has been recently opened to calculate yields as described in Section 4.5, by including all phases and merges the evolution of PARSEC and COLIBRI if needed. The current state only includes the material expelled by winds, which covers the AGB scenarios completely. It can calculate the yields of a set of tracks (calling `set_final_chemistry`) or a single track (with `calculate_final_chemistry`).

APPENDIX B

Other contributions

In this Chapter, I want to briefly describe my contribution to other projects and works, that were somehow linked to the main strand of the main Ph.D. project and are cited at the beginning of each Section.

B.1 Preliminary works

Based on Addari (2020) and Marigo et al. (2022c)

Before even starting the Ph.D. project, I have been involved in studying the final phases of low- and intermediate-mass stars for the Master's Thesis (Addari, 2020). That turned out as a preliminary study for this thesis, as I gained a deep knowledge on the matter and confidence in using proficiently the tools to study stellar structure and evolution. In Addari (2020), I studied the evolution of TP-AGB stars with the `MESA` code (Paxton et al., 2011; Jermyn et al., 2023), with focus on the effects of different exponential overshooting parameters at the bottom of the convective evenlope $f_{\rm env}$ and at both borders of the PDCZ $f_{\rm pdcz}$. That study, even though was much more limited in the exploration of the parameter space, allowed us to somehow identify a similar range for $f_{\rm pdcz} \simeq 0.004 - 0.016$ as commonly stated in the literature (Herwig, 2000; Wagstaff et al., 2020). The input physics of those models was very similar to the one used in the present work, of course accounting for a different numerical framework which can have important effects on the efficiency of the TDU, as I made clear in Chapter 2 and 4. Interestingly, already at the time I encountered the same difficulties in bringing the tracks to the very end of the TP-AGB phase, similar to what I described in Section 3.3.

Although the tracks were not reaching the post-AGB phase, we used them in the work by Marigo et al. (2022c) for estimating the current core mass of the TP-AGB stars in the studied sample from the observed bolometric luminosity, as shown in Figure B.1. The core mass-luminosity relation (CMLR) of TP-AGB stars is a known characteristic of such objects, as it

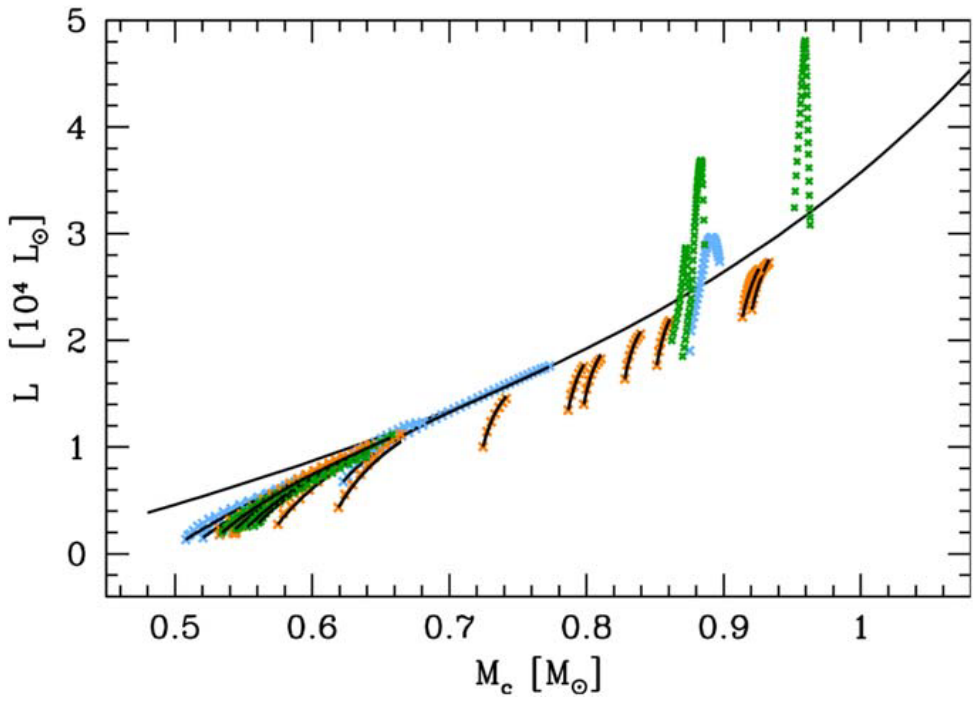

Fig. B.1: Core mass-luminosity relation (CMLR) of TP-AGB stars, Figure 6 by (Marigo et al., 2022c). Each data point is taken at the pre-flesh luminosity maximum, before the on-set of the Helium burning thermonuclear runaway. The models are from Karakas et al. (2002, green crosses) , Cristallo et al. (2011, orange crosses) and Addari (2020, blue crosses). The solid black line covering the whole core mass range is a fit to the asymptotic CMLR for Z = 0.014 (i.e. not considering the first pre-pulses). The black lines overplotted to the models is obtained from synthetic CMLR calculations. See Section 4.5 by (Marigo et al., 2022c) for details.

has been explained and deeply studied in several works published in the past (Eggleton, 1967; Paczyński, 1970; Tuchman et al., 1983; Boothroyd & Sackmann, 1988). It offers a reliable tool, almost independent of the stellar mass, to convert the observed luminosity to the current mass of the core, if no HBB is present. In Figure B.1 the models departing from the fit are indeed those where hydrogen burning is activated at the bottom and inside the convective envelope. In the work by (Marigo et al., 2022c) we went much deeper in analyzing a sample of candidates TP-AGB stars from Gaia DR2 and early DR3 data, characterizing each of them in terms of initial mass, luminosity, mass loss, core mass, period, and pulsation mode.

B.2 Massive stars and beyond

Based on Bressan et al. (2023), Volpato et al. (2024) and Costa et al. (2024)

As it may be clear by now, much of my effort has been focused on studying low- and intermediate-mass stars, both from a physical and numerical point of view. In the years, the PARSEC group has been proficient in covering the whole range of masses, and I found a touch-point through which I could contribute towards more massive stars and the studies about their final fates. At higher masses, and therefore larger temperatures, new nuclear reaction paths

open up as more massive species are involved, and consequently screening effects and neutrino losses become more important. In preparation for simulating the progenitors of electron-capture supernovae and studying the mass threshold between super-AGB and massive stars ($M_{\rm up}$), I revised the calculation of derivatives in the Henyey module and reorganized the energy module in `PARSEC`, generalizing the procedures and including numeric derivatives without resorting to exact derivatives of the screening factors for each reaction. This allows for an easier extension to the most advanced phases of such stars, and after checking the proper working, those contributions have been used for calculating massive star evolution by Bressan et al. (2023); Volpato et al. (2024); Costa et al. (2024).

On top of that, in Appendix A I have described the `kippenhahn.py` module, which has been adopted for the various Kippenhahn diagrams by Volpato et al. (2024) and Costa et al. (2024) for its flexibility and ease of use.

B.3 Thermohaline mixing

Based on Nguyen et al. (2024)

In Chapter 2 I cited thermohaline mixing as one of the non-canonical mixing processes that may occur inside stars. Charbonnel & Zahn (2007) showed that surface abundances of lithium, carbon, and nitrogen in low-mass RGB stars can be explained by including this process in stellar models. In literature, the coefficient is not well-constrained, varying from order unity to hundreds (Charbonnel & Zahn, 2007; Siess, 2009; Cantiello & Langer, 2010; Choi et al., 2016), also because its effect *blends* with other mixing mechanisms such as overshooting and rotation. In the work by Nguyen et al. (2024) we included thermohaline mixing in `PARSEC`, that also required the calculation of the revised equation of state tables, shifting the temperature limit above which matter is considered fully ionized from 10^7 K to 10^8 K. These EOS tables have been used in all stellar models presented in this thesis. More interestingly, we faced the problem of calibrating the thermohaline mixing parameter on observed RGB stars in conjunction with the envelope overshooting, which is also relevant during the first dredge-up.

The inclusion of a new process requires careful debugging and testing to make sure it is properly working, which I carried out along the way, and I had the chance to test it on the TP-AGB phase. Even though a much deeper study is needed to address the issue, the first tests show that there are no sensible effects on the core mass, TDU efficiency, or C/O ratio evolution during this phase. In Figure B.2 I show the first tests on the TP-AGB phase of a 1.9 $M_\odot$ model at solar metallicity. Here I briefly focus on the quantities relevant for shaping the final core mass, consistent with the Ph.D. thesis work, and even for extreme thermohaline coefficient $\alpha_{\rm th}$ values there are no sensible discrepancies. The preliminary result is consistent with what was found in previous works (Cantiello & Langer, 2010), but a dedicated study is needed to answer this question.

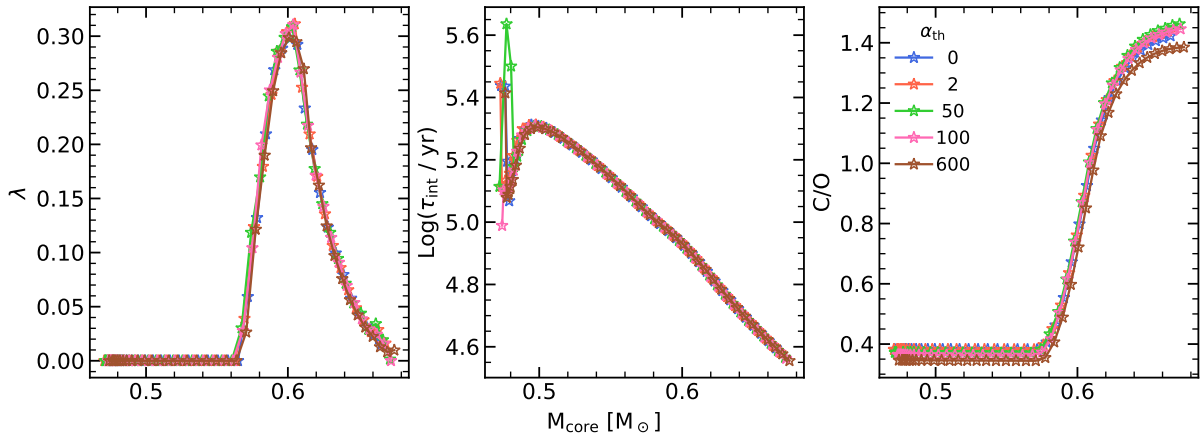

Fig. B.2: Thermohaline mixing tests in the TP-AGB phase of a 1.9 $M_\odot$ and solar metallicity. From left to right: evolution of λ, interpulse duration, and C/O ratio against the core mass for five values of the thermohaline coefficient.

B.4 More on the opacity tables

Based on Marigo et al. (2024)

Recently in the study work by Marigo et al. (2024), we have extended the limits of the low-temperature opacity provided by ÆSOPUS (Marigo & Aringer, 2009; Marigo et al., 2022b) (now version `2.1`) to high pressure and density conditions ($-8 \leq \log R \leq 6$) and spanning temperatures from 100 K to 32000 K. The extended limits cover the range needed for modeling very low-mass stars, brown dwarfs, and planets. In the high-pressure regime, pressure broadening on molecular transitions, electron degeneracy, and, non-ideal effects such as ionization potential depression have to be considered.

In this context, I have used PARSEC to test the extended opacity tables in very low-mass stars and compare them with the same code using ÆSOPUS `2.0` tables, where the maximum value of $\mathrm{Log}\, R = 1$. When the limit is reached, in the outer layers of the convective envelope, PARSEC takes the opacity value at the border of the table. If the temperature gradient in these layers is adiabatic, then it should be rather insensitive to variations in the opacity. The models were computed at metallicity $Z = 0.01779$ and solar composition from Caffau et al. (2011), also with $T - \tau$ relations adopted from PHOENIX atmosphere models (Allard et al., 2012), thoroughly discussed by Chen et al. (2014) and we also included models with a shift (labeled with S) in the relation again explained by Chen et al. (2014). I covered the mass range $0.1 \leq M_{\rm ini}/\mathrm{M}_\odot \leq 0.85$ spaced with 0.05 $\mathrm{M}_\odot$, and results are shown in Figure B.3. The ÆSOPUS `2.1` models at 5 Gyr differ significantly with the new opacity, as they are consistently fainter and cooler than the ÆSOPUS `2.0` models. The discrepancy reduces at initial mass about $M_{\rm ini} = 0.6$ $\mathrm{M}_\odot$, because the structure does not extend above $\mathrm{Log}\, R = 1$, therefore they are effectively using the same table as the previous version. The same tracks are also shown in the mass-radius diagram with data from double-lined eclipsing binary catalogs (see caption for references). Already the ÆSOPUS `2.0` show a good general agreement, but slightly underestimating the radius between

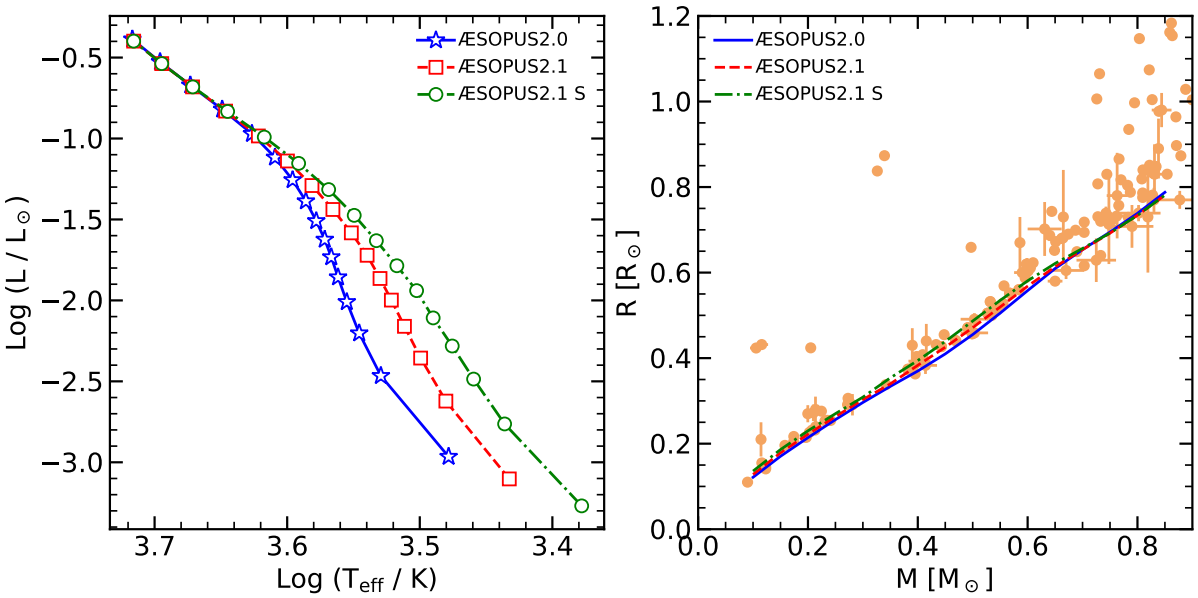

Fig. B.3: The impact of the new ÆSOPUS 2.1 Rosseland mean opacities on low-mass stellar models. The left panel shows the position in the HR diagram at 5 Gyr for models in the mass range from 0.1 to 0.85 $M_\odot$ and computed at intervals of 0.05 $M_\odot$ (from bottom-right to top-left). The blue symbols indicate models computed with the previous version of the opacity tables from Marigo et al. (2022b), while the red and green symbols are for models computed with the new ÆSOPUS 2.1 opacity tables. The green symbols correspond to models with a shift in their $T - \tau$ relation (see text for details). The right panel shows the same models in the mass-radius plane, superimposed with the empirical data of low-mass stars in double-lined eclipsing binary catalogs from Ségransan et al. (2003); Demory et al. (2009); Torres et al. (2010); Carter et al. (2011); Doyle et al. (2011); Kraus et al. (2011); Parsons et al. (2012a,b); Southworth (2014).

$0.1 \leq M_{\rm ini}/M_\odot \leq 0.6$. The new opacity tables inflate the models, and even more with a temperature shift of $\Delta\,{\rm Log}(T/T_{\rm eff}) = 0.03$ dex for ${\rm Log}(T_{\rm eff}/{\rm K}) < 3.5$ (gradually reduced to 0 for ${\rm Log}(T_{\rm eff}/{\rm K})$ between 3.5 and 3.765). The mass-radius discrepancy will be studied more in the future, and more details about ÆSOPUS 2.1 are given by Marigo et al. (2024).

References

Addari, F. 2020, Master's thesis, University of Padua. https://thesis.unipd.it/handle/20.500.12608/22550

Addari, F., Marigo, P., Bressan, A., et al. 2024, The Astrophysical Journal, 964, 51, doi: 10.3847/1538-4357/ad2067

Allard, F., Homeier, D., & Freytag, B. 2012, Philosophical Transactions of the Royal Society A: Mathematical, Physical and Engineering Sciences, 370, 2765, doi: 10.1098/rsta.2011.0269

Alongi, M., Bertelli, G., Bressan, A., & Chiosi, C. 1991, Astronomy & Astrophysics, 244, 95. https://articles.adsabs.harvard.edu/pdf/1991A%26A...244...95A

Angulo, C., Arnould, M., Rayet, M., et al. 1999, Nuclear Physics A, 656, 3, doi: 10.1016/S0375-9474(99)00030-5

Bedijn, P. J. 1988, Astronomy and Astrophysics, 205, 105. https://ui.adsabs.harvard.edu/abs/1988A&A...205..105B

Bladh, S., Eriksson, K., Marigo, P., Liljegren, S., & Aringer, B. 2019, Astronomy & Astrophysics, 623, A119, doi: 10.1051/0004-6361/201834778

Bloecker, T. 1995, Astronomy and Astrophysics, 297, 727. https://ui.adsabs.harvard.edu/abs/1995A&A...297..727B

Boothroyd, A. I., & Sackmann, I. J. 1988, The Astrophysical Journal, 328, 641, doi: 10.1086/166322

Bowen, G. H. 1988, The Astrophysical Journal, 329, 299, doi: 10.1086/166378

Bressan, A., Bertelli, G., & Chiosi, C. 1986, Memorie della Societa Astronomica Italiana, 57, 411. https://ui.adsabs.harvard.edu/abs/1986MmSAI..57..411B

Bressan, A., Costa, G., Goswami, S., et al. 2023, 94, 91, doi: 10.36116/MEMSAIT_94N2.2023.91

Bressan, A., Girardi, L., Marigo, P., Rosenfield, P., & Tang, J. 2015, 39, 25. https://ui.adsabs.harvard.edu/abs/2015ASSP...39...25B

Bressan, A., Marigo, P., Girardi, L., et al. 2012, MNRAS, 427, 127, doi: 10.1111/j.1365-2966.2012.21948.x

Bressan, A. G., Chiosi, C., & Bertelli, G. 1981, Astronomy and Astrophysics, 102, 25. https://ui.adsabs.harvard.edu/abs/1981A&A...102...25B

Böhm-Vitense, E. 1958, Zeitschrift fur Astrophysik, 46, 108. https://ui.adsabs.harvard.edu/abs/1958ZA.....46..108B

Caffau, E., Ludwig, H.-G., Steffen, M., Freytag, B., & Bonifacio, P. 2011, Solar Physics, 268, 255, doi: 10.1007/s11207-010-9541-4

Cantiello, M., & Langer, N. 2010, Astronomy and Astrophysics, 521, A9, doi: 10.1051/0004-6361/201014305

Canton, P. A., Williams, K. A., Kilic, M., & Bolte, M. 2021, The Astronomical Journal, 161, 169, doi: 10.3847/1538-3881/abe1ad

Carter, J. A., Fabrycky, D. C., Ragozzine, D., et al. 2011, Science, 331, 562, doi: 10.1126/science.1201274

Caughlan, G. R., & Fowler, W. A. 1988, Atomic Data and Nuclear Data Tables, 40, 283, doi: 10.1016/0092-640X(88)90009-5

Chandrasekhar, S. 1931, The Astrophysical Journal, 74, 81, doi: 10.1086/143324

Charbonnel, C., & Zahn, J.-P. 2007, Astronomy & Astrophysics, 467, L15, doi: 10.1051/0004-6361:20077274

Charbonnel, C., Lagarde, N., Jasniewicz, G., et al. 2020, Astronomy & Astrophysics, 633, A34, doi: 10.1051/0004-6361/201936360

Chen, Y., Girardi, L., Bressan, A., et al. 2014, Monthly Notices of the Royal Astronomical Society, 444, 2525, doi: 10.1093/mnras/stu1605

Chieffi, A., Limongi, M., & Straniero, O. 1998, The Astrophysical Journal, 502, 737, doi: 10.1086/305921

Choi, J., Dotter, A., Conroy, C., et al. 2016, The Astrophysical Journal, 823, 102, doi: 10.3847/0004-637X/823/2/102

Christensen-Dalsgaard, J., Monteiro, M. J. P. F. G., Rempel, M., & Thompson, M. J. 2011, Monthly Notices of the Royal Astronomical Society, 414, 1158, doi: 10.1111/j.1365-2966.2011.18460.x

Claret, A., & Torres, G. 2017, The Astrophysical Journal, 849, 18, doi: 10.3847/1538-4357/aa8770

Constantino, T., Campbell, S. W., Lattanzio, J. C., & van Duijneveldt, A. 2016, Monthly Notices of the Royal Astronomical Society, 456, 3866, doi: 10.1093/mnras/stv2939

Costa, G. 2019, PhD thesis, Scuola Internazionale Superiore di Studi Avanzati. https://www.sissa.it/ap/phdsection/AlumniThesis/Guglielmo%20Costa.pdf

Costa, G., Girardi, L., Bressan, A., et al. 2019, Monthly Notices of the Royal Astronomical Society, 485, 4641, doi: 10.1093/mnras/stz728

Costa, G., Shepherd, K. G., Bressan, A., et al. 2024, to be submitted

Costantini, H., deBoer, R. J., Azuma, R. E., et al. 2010, Physical Review C, 82, 035802, doi: 10.1103/PhysRevC.82.035802

Cranmer, S. R., & Saar, S. H. 2011, The Astrophysical Journal, 741, 54, doi: 10.1088/0004-637X/741/1/54

Cristallo, S., Piersanti, L., Straniero, O., et al. 2011, The Astrophysical Journal Supplement Series, 197, 17, doi: 10.1088/0067-0049/197/2/17

Cummings, J. D., Kalirai, J. S., Choi, J., et al. 2019, The Astrophysical Journal, 871, L18, doi: 10.3847/2041-8213/aafc2d

Cummings, J. D., Kalirai, J. S., Tremblay, P.-E., Ramirez-Ruiz, E., & Choi, J. 2018, The Astrophysical Journal, 866, 21, doi: 10.3847/1538-4357/aadfd6

Cyburt, R. H., & Davids, B. 2008, Physical Review C, 78, 064614, doi: 10.1103/PhysRevC.78.064614

Cyburt, R. H., Hoffman, R. D., & Woosley, S. 2012, REACLIB. https://reaclib.jinaweb.org/labels.php?action=viewLabel&label=chw0

Cyburt, R. H., Amthor, A. M., Ferguson, R., et al. 2010, The Astrophysical Journal Supplement Series, 189, 240, doi: 10.1088/0067-0049/189/1/240

Demory, B.-O., Ségransan, D., Forveille, T., et al. 2009, Astronomy & Astrophysics, 505, 205, doi: 10.1051/0004-6361/200911976

Descouvemont, P., Adahchour, A., Angulo, C., Coc, A., & Vangioni-Flam, E. 2004, Atomic Data and Nuclear Data Tables, 88, 203, doi: 10.1016/j.adt.2004.08.001

Doherty, C. L., Gil-Pons, P., Siess, L., & Lattanzio, J. C. 2017, Publications of the Astronomical Society of Australia, 34, e056, doi: 10.1017/pasa.2017.52

Dotter, A. 2016, The Astrophysical Journal Supplement Series, 222, 8, doi: 10.3847/0067-0049/222/1/8

Doyle, L. R., Carter, J. A., Fabrycky, D. C., et al. 2011, Science, 333, 1602, doi: 10.1126/science.1210923

Dreizler, S., Werner, K., Jordan, S., & Hagen, H. 1994, Astronomy and Astrophysics, 286, 463. https://ui.adsabs.harvard.edu/abs/1994A&A...286..463D

Eggenberger, P., Meynet, G., Maeder, A., et al. 2008, Astrophysics and Space Science, 316, 43, doi: 10.1007/s10509-007-9511-y

Eggleton, P. P. 1967, Monthly Notices of the Royal Astronomical Society, 135, 243, doi: 10.1093/mnras/135.3.243

Eriksson, K., Nowotny, W., Höfner, S., Aringer, B., & Wachter, A. 2014, Astronomy & Astrophysics, 566, A95, doi: 10.1051/0004-6361/201323241

Ferguson, J. W., Alexander, D. R., Allard, F., et al. 2005, The Astrophysical Journal, 623, 585, doi: 10.1086/428642

Ferrario, L., Wickramasinghe, D., Liebert, J., & Williams, K. A. 2005, Monthly Notices of the Royal Astronomical Society, 361, 1131, doi: 10.1111/j.1365-2966.2005.09244.x

Freytag, B., Ludwig, H. G., & Steffen, M. 1996, Astronomy and Astrophysics, 313, 497. https://ui.adsabs.harvard.edu/abs/1996A&A...313..497F

Frost, C. A., & Lattanzio, J. C. 1996, The Astrophysical Journal, 473, 383, doi: 10.1086/178152

Fu, X., Bressan, A., Marigo, P., et al. 2018, Monthly Notices of the Royal Astronomical Society, 476, 496, doi: 10.1093/mnras/sty235

Fynbo, H. O. U., Diget, C. A., Bergmann, U. C., et al. 2005, Nature, 433, 136. https://ui.adsabs.harvard.edu/abs/2005Natur.433..136F

Gabriel, M., Noels, A., Montalbán, J., & Miglio, A. 2014, Astronomy and Astrophysics, 569, A63, doi: 10.1051/0004-6361/201423442

Groenewegen, M. A. T., & de Jong, T. 1993, Astronomy and Astrophysics, 267, 410. https://ui.adsabs.harvard.edu/abs/1993A&A...267..410G

Hansen, C. 2004, Stellar Interiors - Physical Principles, Struct. and Evolution (Springer-Verlag)

Harris, C. R., Millman, K. J., van der Walt, S. J., et al. 2020, Nature, 585, 357, doi: 10.1038/s41586-020-2649-2

Heil, M., Detwiler, R., Azuma, R. E., et al. 2008, Physical Review C, 78, 025803, doi: 10.1103/PhysRevC.78.025803

Henyey, L. G., Forbes, J. E., & Gould, N. L. 1964, The Astrophysical Journal, 139, 306, doi: 10.1086/147754

Henyey, L. G., Wilets, L., Böhm, K. H., Lelevier, R., & Levee, R. D. 1959, The Astrophysical Journal, 129, 628, doi: 10.1086/146661

Herwig, F. 1999, Internal mixing and surface abundance of [WC]-CSPN, arXiv. http://arxiv.org/abs/astro-ph/9912353

—. 2000, arXiv:astro-ph/0007139. http://arxiv.org/abs/astro-ph/0007139

—. 2005, Annual Review of Astronomy and Astrophysics, 43, 435, doi: 10.1146/annurev.astro.43.072103.150600

Hopf, E. 1934, Mathematical Problems of Radiative Equilibrium, 1 No. 31 (Cambridge University Press)

Hunter, J. D. 2007, Computing in Science & Engineering, 9, 90, doi: 10.1109/MCSE.2007.55

Iglesias, C. A., & Rogers, F. J. 1996, The Astrophysical Journal, 464, 943, doi: 10.1086/177381

Iliadis, C., Angulo, C., Descouvemont, P., Lugaro, M., & Mohr, P. 2008, Physical Review C, 77, 045802, doi: 10.1103/PhysRevC.77.045802

Iliadis, C., Longland, R., Champagne, A. E., Coc, A., & Fitzgerald, R. 2010, Nuclear Physics A, 841, 31, doi: 10.1016/j.nuclphysa.2010.04.009

Imbriani, G., Costantini, H., Formicola, A., et al. 2005, European Physical Journal A, 25, 455, doi: 10.1140/epja/i2005-10138-7

Irwin, A. W. 2012, Astrophysics Source Code Library, ascl:1211.002. https://ui.adsabs.harvard.edu/abs/2012ascl.soft11002I

Itoh, N., Uchida, S., Sakamoto, Y., Kohyama, Y., & Nozawa, S. 2008, The Astrophysical Journal, 677, 495, doi: 10.1086/529367

Izzard, R. G., Tout, C. A., Karakas, A. I., & Pols, O. R. 2004, Monthly Notices of the Royal Astronomical Society, 350, 407, doi: 10.1111/j.1365-2966.2004.07446.x

Jahn, D., Rauch, T., Reiff, E., et al. 2007, Astronomy and Astrophysics, 462, 281, doi: 10.1051/0004-6361:20065901

Jermyn, A. S., Bauer, E. B., Schwab, J., et al. 2023, The Astrophysical Journal Supplement Series, 265, 15, doi: 10.3847/1538-4365/acae8d

Kalirai, J. S., Davis, D. S., Richer, H. B., et al. 2009, The Astrophysical Journal, 705, 408, doi: 10.1088/0004-637X/705/1/408

Kalirai, J. S., Hansen, B. M. S., Kelson, D. D., et al. 2008, The Astrophysical Journal, 676, 594, doi: 10.1086/527028

Kalirai, J. S., Marigo, P., & Tremblay, P.-E. 2014, The Astrophysical Journal, 782, 17, doi: 10.1088/0004-637X/782/1/17

Karakas, A., & Lattanzio, J. C. 2007, Publications of the Astronomical Society of Australia, 24, 103, doi: 10.1071/AS07021

Karakas, A. I. 2003, PhD thesis, Monash University

—. 2014, Monthly Notices of the Royal Astronomical Society, 445, 347, doi: 10.1093/mnras/stu1727

Karakas, A. I., & Lattanzio, J. C. 2014, Publications of the Astronomical Society of Australia, 31, e030, doi: 10.1017/pasa.2014.21

Karakas, A. I., Lattanzio, J. C., & Pols, O. R. 2002, Publications of the Astronomical Society of Australia, 19, 515, doi: 10.1071/AS02013

Kifonidis, K., Plewa, T., Janka, H. T., & Müller, E. 2003, Astronomy and Astrophysics, 408, 621, doi: 10.1051/0004-6361:20030863

Kippenhahn, R. 1990, Stellar structure and evolution (Springer-Verlag)

Kippenhahn, R., Weigert, A., & Hofemeister, E. 1967, in Methods in Computational Physics, Vol. 7 (Academic Press), 129–189

Koesterke, L., & Werner, K. 1998, The Astrophysical Journal, 500, L55, doi: 10.1086/311383

Komatsu, E., Smith, K. M., Dunkley, J., et al. 2011, The Astrophysical Journal Supplement Series, 192, 18, doi: 10.1088/0067-0049/192/2/18

Kraus, A. L., Tucker, R. A., Thompson, M. I., Craine, E. R., & Hillenbrand, L. A. 2011, The Astrophysical Journal, 728, 48, doi: 10.1088/0004-637X/728/1/48

Lattanzio, J. C., Tout, C. A., Neumerzhitckii, E. V., Karakas, A. I., & Lesa, P. 2017, Memorie della Società Astronomica Italiana, 4

Lau, H. H. B., Gil-Pons, P., Doherty, C., & Lattanzio, J. 2012, Astronomy & Astrophysics, 542, A1, doi: 10.1051/0004-6361/201218826

Leblanc, P. J., Imbriani, G., Görres, J., et al. 2010, Physical Review C, 82, 055804, doi: 10.1103/PhysRevC.82.055804

Lee, M. G., Freedman, W. L., & Madore, B. F. 1993, The Astrophysical Journal, 417, 553, doi: 10.1086/173334

Li, Z., Su, J., Guo, B., et al. 2010, Science China Physics, Mechanics, and Astronomy, 53, 658, doi: 10.1007/s11433-010-0128-8

Limongi, M., & Chieffi, A. 2020, The Astrophysical Journal, 902, 95, doi: 10.3847/1538-4357/abb4e8

Limongi, M., Roberti, L., Chieffi, A., & Nomoto, K. 2024, The Astrophysical Journal Supplement Series, 270, 29, doi: 10.3847/1538-4365/ad12c1

Maeder, A. 2009, Physics, Formation and Evolution of Rotating Stars (Springer), doi: 10.1007/978-3-540-76949-1

Marigo, P. 2022, Universe, 8, 243, doi: 10.3390/universe8040243

Marigo, P., Addari, F., Bossini, D., et al. 2024, AESOPUS 2.1: Low-Temperature Opacities Extended to High Pressure, doi: 10.48550/arXiv.2409.10905

Marigo, P., & Aringer, B. 2009, Astronomy & Astrophysics, 31

Marigo, P., Aringer, B., Girardi, L., & Bressan, A. 2022a, The Astrophysical Journal, 940, 129, doi: 10.3847/1538-4357/ac9b40

—. 2022b, Low-Temperature Gas Opacities with AESOPUS 2.0, arXiv. http://arxiv.org/abs/2210.08587

Marigo, P., Bressan, A., Nanni, A., Girardi, L., & Pumo, M. L. 2013, Monthly Notices of the Royal Astronomical Society, 434, 488, doi: 10.1093/mnras/stt1034

Marigo, P., & Girardi, L. 2007, Astronomy & Astrophysics, 469, 239, doi: 10.1051/0004-6361:20066772

Marigo, P., Girardi, L., & Bressan, A. 1999, Astronomy and Astrophysics, 344, 123, doi: 10.48550/arXiv.astro-ph/9901235

Marigo, P., Cummings, J. D., Curtis, J. L., et al. 2020, Nature Astronomy, 4, 1102, doi: 10.1038/s41550-020-1132-1

Marigo, P., Bossini, D., Trabucchi, M., et al. 2022c, The Astrophysical Journal Supplement Series, 258, 43, doi: 10.3847/1538-4365/ac374a

Mattsson, L., Wahlin, R., & Höfner, S. 2010, Astronomy and Astrophysics, 509, A14, doi: 10.1051/0004-6361/200912084

Meynet, G., & Maeder, A. 1997, Astronomy and Astrophysics, 321, 465. https://ui.adsabs.harvard.edu/abs/1997A&A...321..465M

Miller Bertolami, M. M. 2016, Astronomy & Astrophysics, 588, A25, doi: 10.1051/0004-6361/201526577

Miller Bertolami, M. M., & Althaus, L. G. 2006, Astronomy and Astrophysics, 454, 845, doi: 10.1051/0004-6361:20054723

Mowlavi, N. 1999, Astronomy & Astrophysics

Nguyen, C. T., Costa, G., Girardi, L., et al. 2022, Astronomy and Astrophysics. http://arxiv.org/abs/2207.08642

Nguyen, C. T., Bressan, A., Korn, A. J., et al. 2024, submitted to A\&A

Paczyński, B. 1970, Acta Astronomica, 20, 47. https://ui.adsabs.harvard.edu/abs/1970AcA....20...47P

Parsons, S. G., Marsh, T. R., Gänsicke, B. T., et al. 2012a, Monthly Notices of the Royal Astronomical Society, 420, 3281, doi: 10.1111/j.1365-2966.2011.20251.x

—. 2012b, Monthly Notices of the Royal Astronomical Society, 419, 304, doi: 10.1111/j.1365-2966.2011.19691.x

Pastorelli, G., Marigo, P., Girardi, L., et al. 2019, Monthly Notices of the Royal Astronomical Society, 485, 5666, doi: 10.1093/mnras/stz725

—. 2020, Monthly Notices of the Royal Astronomical Society, 498, 3283, doi: 10.1093/mnras/staa2565

Paxton, B., Bildsten, L., Dotter, A., et al. 2011, The Astrophysical Journal Supplement Series, 192, 3, doi: 10.1088/0067-0049/192/1/3

Portinari, L., Chiosi, C., & Bressan, A. 1998, Astronomy and Astrophysics, 334, 505, doi: 10.48550/arXiv.astro-ph/9711337

Reimers, D. 1975, Memoires of the Societe Royale des Sciences de Liege, 8, 369. https://ui.adsabs.harvard.edu/abs/1975MSRSL...8..369R

Sackmann, I. J., Smith, R. L., & Despain, K. H. 1974, The Astrophysical Journal, 187, 555, doi: 10.1086/152666

Salaris, M., Serenelli, A., Weiss, A., & Miller Bertolami, M. 2009, The Astrophysical Journal, 692, 1013, doi: 10.1088/0004-637X/692/2/1013

Salpeter, E. E. 1955, The Astrophysical Journal, 121, 161, doi: 10.1086/145971

Saumon, D., Blouin, S., & Tremblay, P.-E. 2022, Physics Reports, 988, 1, doi: 10.1016/j.physrep.2022.09.001

Siess, L. 2006, Astronomy and Astrophysics, 448, 717, doi: 10.1051/0004-6361:20053043

—. 2007, Astronomy and Astrophysics, 476, 893, doi: 10.1051/0004-6361:20078132

—. 2009, Astronomy & Astrophysics, 497, 463, doi: 10.1051/0004-6361/200811362

Siess, L., Dufour, E., & Forestini, M. 2000, Astronomy and Astrophysics, 358, 593, doi: 10.48550/arXiv.astro-ph/0003477

Southworth, J. 2014, The DEBCat detached eclipsing binary catalogue, arXiv, doi: 10.48550/arXiv.1411.1219

Stancliffe, R. J. 2006, Monthly Notices of the Royal Astronomical Society, 370, 1817, doi: 10.1111/j.1365-2966.2006.10595.x

Stancliffe, R. J., Izzard, R. G., & Tout, C. A. 2005, Monthly Notices of the Royal Astronomical Society, 356, L1, doi: 10.1111/j.1745-3933.2005.08491.x

Strandberg, E., Beard, M., Couder, M., et al. 2008, Physical Review C, 77, 055801, doi: 10.1103/PhysRevC.77.055801

Straniero, O., Chieffi, A., Limongi, M., et al. 1997, The Astrophysical Journal, 478, 332, doi: 10.1086/303794

Straniero, O., Domínguez, I., Cristallo, S., & Gallino, R. 2003, Publications of the Astronomical Society of Australia, 20, 389, doi: 10.1071/AS03041

Ségransan, D., Kervella, P., Forveille, T., & Queloz, D. 2003, Astronomy & Astrophysics, 397, L5, doi: 10.1051/0004-6361:20021714

Tang, J., Bressan, A., Rosenfield, P., et al. 2014, Monthly Notices of the Royal Astronomical Society, 445, 4287, doi: 10.1093/mnras/stu2029

Thoul, A. A., Bahcall, J. N., & Loeb, A. 1994, The Astrophysical Journal, 421, 828, doi: 10.1086/173695

Torres, G., Andersen, J., & Giménez, A. 2010, The Astronomy and Astrophysics Review, 18, 67, doi: 10.1007/s00159-009-0025-1

Tuchman, Y., Glasner, A., & Barkat, Z. 1983, The Astrophysical Journal, 268, 356, doi: 10.1086/160958

Tuli, J. 2012, National Nuclear Data Center. https://reaclib.jinaweb.org/labels.php?action=viewLabel&label=chw0

Ventura, P., Karakas, A., Dell'Agli, F., García-Hernández, D. A., & Guzman-Ramirez, L. 2018, Monthly Notices of the Royal Astronomical Society, doi: 10.1093/mnras/stx3338

Virtanen, P., Gommers, R., Oliphant, T. E., et al. 2020, Nature Methods, 17, 261, doi: 10.1038/s41592-019-0686-2

Volpato, G., Marigo, P., Costa, G., et al. 2024, The Astrophysical Journal, 961, 89, doi: 10.3847/1538-4357/ad1185

Wagenhuber, J., & Groenewegen, M. A. T. 1998, Astronomy and Astrophysics, 340, 183, doi: 10.48550/arXiv.astro-ph/9809338

Wagenhuber, J., & Weiss, A. 1994, Astronomy and Astrophysics, 290, 807. https://ui.adsabs.harvard.edu/abs/1994A&A...290..807W

Wagstaff, G., Bertolami, M. M. M., & Weiß, A. 2020, Monthly Notices of the Royal Astronomical Society, 493, 4748, doi: 10.1093/mnras/staa362

Weidemann, V. 1977, Astronomy and Astrophysics, 59, 411. https://ui.adsabs.harvard.edu/abs/1977A&A....59..411W

—. 1987, Astronomy and Astrophysics, 188, 74. https://ui.adsabs.harvard.edu/abs/1987A&A...188...74W

—. 2000, Astronomy and Astrophysics, 363, 647. https://ui.adsabs.harvard.edu/abs/2000A&A...363..647W

Weidemann, V., & Koester, D. 1983, Astronomy and Astrophysics, 121, 77. https://ui.adsabs.harvard.edu/abs/1983A&A...121...77W

Weigert, A. 1966, Zeitschrift fur Astrophysik, 64, 395. https://ui.adsabs.harvard.edu/abs/1966ZA.....64..395W

Weiss, A., & Ferguson, J. W. 2009, Astronomy and Astrophysics, 508, 1343, doi: 10.1051/0004-6361/200912043

Weiss, A., Hillebrandt, W., Thomas, H. C., & Ritter, H. 2004, Cox and Giuli's Principles of Stellar Structure (Cambridge Scientific Publishers). https://ui.adsabs.harvard.edu/abs/2004cgps.book.....W

Werner, K., & Herwig, F. 2006, Publications of the Astronomical Society of the Pacific, 118, 183, doi: 10.1086/500443

Werner, K., & Rauch, T. 2014, Astronomy & Astrophysics, 569, A99, doi: 10.1051/0004-6361/201424051

Werner, K., Rauch, T., & Kruk, J. W. 2005, Astronomy and Astrophysics, 433, 641, doi: 10.1051/0004-6361:20042258

—. 2015, Astronomy and Astrophysics, 582, A94, doi: 10.1051/0004-6361/201526842

—. 2016, Astronomy & Astrophysics, 593, A104, doi: 10.1051/0004-6361/201628892

Williams, K. A., Bolte, M., & Koester, D. 2004, The Astrophysical Journal, 615, L49, doi: 10.1086/425995

—. 2009, The Astrophysical Journal, 693, 355, doi: 10.1088/0004-637X/693/1/355

Winters, J. M., Bertre, T. L., Jeong, K. S., Helling, C., & Sedlmayr, E. 2000, Astronomy & Astrophysics

Wood, P. R., & Faulkner, D. J. 1986, The Astrophysical Journal, 307, 659, doi: 10.1086/164451

Woosley, S. E., Heger, A., & Weaver, T. A. 2002, Reviews of Modern Physics, 74, 1015, doi: 10.1103/RevModPhys.74.1015